Rijksuniversiteit Groningen

Master Research Project

---

# Semi-automatic calibration procedure for a goniometric setup to measure the optical and geometrical properties of compound eyes

---

*Author:*
Jasper van Vliet
*Daily Supervisor:*
Doekele Stavenga

*First Supervisor:*
Mauricio Muñoz Arias
*Second Supervisor:*
Jacquelien Scherpen

2022

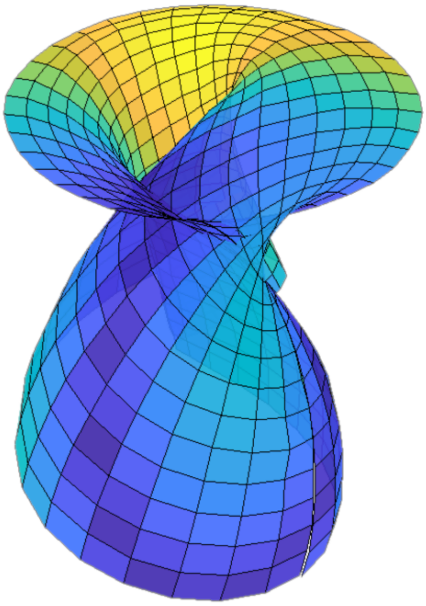

## Abstract

A motorised system capable of mapping optical properties of compound eyes cannot determine the morphology of the compound eye from the available goniometric data. As a proof of concept, the required methods are developed to semi-automatically calibrate the position of a reference object such that the morphology is directly related to the goniometric data. Secondly, a post-processing method is designed to correct the obtained goniometric data, because, in practice, it is expected that the position of the scanned object won't always be ideal. It has been shown that the developed methods can accurately reconstruct the morphology of the reference object from the data obtained by the apparatus. Morphology scanning of a reference object is proven successful.

# Acknowledgements

First and foremost, I would like to thank my supervisor Mauricio Muñoz Arias for offering me this project. I clearly remember the mini tour we did for the available projects. This project stood out the most, because of the potential problems that had to be solved, mainly using Matlab, with I love to work with, and some other code languages which were, at the time, unfamiliar to me. Our weekly meetings and numerous Friday co-operation days kept me on my toes and I very appreciated the provided literature and ideas you brought into the project. Thanks for all the guidance during the project.

Secondly, I'm extremely grateful to prof. dr. Doekele Stavenga for the Intangible support he provided during the project. The possibility for (bi)daily support has been very helpful during the project and I really appreciate the open minded communication we could have. I have learned a lot form working in the lab, and helping to move the GRACE setup to the new location was actually a wonderful experience. Even though biology is not my background, I really learned to appreciate the different types of compound eyes, which I will always remember. Somehow, I most often remember the story about starfish and their primal use of their limited vision, but the house fly, or rather Musca Domestica are also a fruitful memory.

A special thanks to prof. dr. ir. Jacquelien Scherpen, for being present *offline*, during my presentation. It was really nice to have someone to talk to and I also appreciated the feedback received.

Lastly, I would be remiss in not mentioning my girlfriend for the moral support, and not being too displeased with me for staying up many nights, coding and writing. Your help and little guidance at the time of need has been lovely.

# Contents

# List of Figures

# List of Tables

# Chapter 1

# Introduction

## 1.1 Introduction

The visual system is one of the key senses that is extensively used for almost all essential behaviour of living beings. Arthropods receive visual information through compound eyes consisting of typically thousands of individual photoreceptor units called ommatidia [3]. The differences between compound eyes are extensive, while little is known about how subtle differences affect vision [4].

Biologists interested in behaviour and visual ecology greatly benefit from quantitative studies providing opportunities for a better understanding of the evolution of vision. Knowledge about optical and geometrical properties such as the optical organisation and visual acuity of compound eyes is crucial for quantitative studies about the neural processing of visual information [3–6].

The pseudopupil technique is used to obtain optical properties of compound eyes such as facet diameter, inter ommatidia angles and the visual axes of insect compound eyes [7].

The optical organisation of compound eyes is also used to create models for the development and production of artificial eyes. This is motivated by the intrinsic advantages of compound eyes: they are compact, have a large field of view and are highly sensitive to moving objects [8]. Some of the applications for artificial eyes are medical imaging, vision and navigation systems such as drones, industrial engineering and space engineering. However, the current geometrical models of compound eyes used to develop and fabricate these artificial eyes are far from perfect [8].

An accurate geometrical description of compound eyes may have substantial potential for medical and industrial vision applications [7]. Additionally, it may provide additional insight for optical properties such as the inter-ommatidial angles and secondary information for the mapping of the facet sizes. In particular compound eyes of which the shape differs from a spherical approximation benefit from a morphological description.

Historically the procedures for mapping the visual axes of compound eyes were done manually, which was very time consuming and is described as ”extremely tedious” [7, 9, 10].

Present-day robotised goniometric setups automate and speed up the mapping process significantly. State of the art is a highly automated goniometer instrument called FACETS. The FACETS instrument is developed to facilitate rapid mapping of compound eye parameters for investigating regional visual field specialisations [7, 10].

The goniometric research apparatus for compound eyes (GRACE) is developed at the University of Groningen for the automated charting of the visual space of insect compound eyes. Over the years, the system has been modified and methods were developed to improve the automated scanning capabilities of the system [11–23].

Currently the system is unable to resolve the geometry of the compound eyes. Additionally there are no calibration procedures to verify the accuracy and calibration of the goniometer. Also, the control of the goniometric setup is in an inadequate state for complex methods to be developed. And lastly, the measurement process can be further streamlined by improving current methods causing problems and implementing additional methods that reduce the amount of manual preparation needed.

The outline of the thesis is as follows. First, in section 1.2 and 1.3, the research goal and research question are presented. This is followed by the materials and methods in chapter 2 and 3, which provide information regarding the GRACE setup and describe the developed methods. Thereafter, in chapter 4, the results of the methods are described and analysed. Next are the discussion and recommendations, in chapter 5, and finally, the results of the project are concluded in chapter 6.

## 1.2 Research Objective

The current objective for the GRACE system is to accurately measure the geometry of a compound eye. This enables accurate geometrical models of compound eyes to be made for the fabrication of artificial eyes. Furthermore, this geometrical model can be used to improve the accuracy of the optical properties determined of the compound eye, because these methods do relay on geometrical assumptions [7].

To be able to accurately measure the geometry of an object with the GRACE system, the position of the object should be tracked precisely. The position of a compound eye can't be measured directly with micrometer precision, therefore the position of the object must be determined indirectly using the goniometer of the GRACE system. This lead to the following research objective:

Develop, implement and validate the methods required to enable the geometry mapping of an object that is scanned using the GRACE system.

## 1.3 Research Question

The objective of this research project is to accurately represent an object scanned with the GRACE system. While the object is scanned, it is rotated under an epi-illumination microscope used to image the surface. These movements potentially change the position of the object with respect to the origin of the goniometer, posing a problem for the accurate tracking of the objects shape. This leads to the following research question and sub-questions:

- What methods are required to accurately map the geometry of an object scanned with the GRACE system?
    - How to validate the developed methods for geometry scanning?
    - What is the impact of a positional error of the scanning object on the acquired geometrical data and how can this impact be minimised?

The answer to the first sub-question is described in section 2.2 which enables the development and verification of the developed methods. The second sub-question is answered in section 2.3, which also provides essential knowledge to answer the main research question.

# Chapter 2

# Materials

The information presented in the following three sections, provides the reader with the necessary information to understand the developed methods required for geometry scanning. The first section described the hardware of the GRACE system. The next section is about the calibration object, which is used to validate the developed methods. In the thirth section, a mathematical description of the object position is presented, which is a vital element in all the developed methods.

## 2.1 Hardware Description

The GRACE system can be divided into three subsystems which are essential for the automated scanning capabilities of the system. The three subsystems are: a motorised multi-axes goniometer system, an epi-illumination microscope imaging system and a computer control system running MATLAB®. A schematic overview of the complete system is given in Figure 2.1. Hardware specifics such as part numbers can be found in subsection A.1.1.

### 2.1.1 System Control

The GRACE system can be controlled in two ways: with physical accessible controls, i.e. manually, and with software commands using MATLAB, i.e. digitally. The two methods are dependent on each other because they cannot be used at the same time. However, the manual controls are always accessible and are able to overrule the digital controls.

**Manual**

The joysticks are used to control the linear and rotary axes of the goniometer. Each joystick controls two axes, with the exception of the one which controls the $z$-axis solely. The linear stages are used to position the object in view of the microscope, while the rotary stages rotate the object or specimen to view it from different directions. Components of the optical stage that can be controlled physically are the light intensity and the height of the microscope. Using the oculars, it can be verified if the object or specimen is in the right position.

**Digital**

All electronically driven equipment of the GRACE setup can be controlled using software commands. A (virtual) serial interface must be present between a desktop PC and the respective

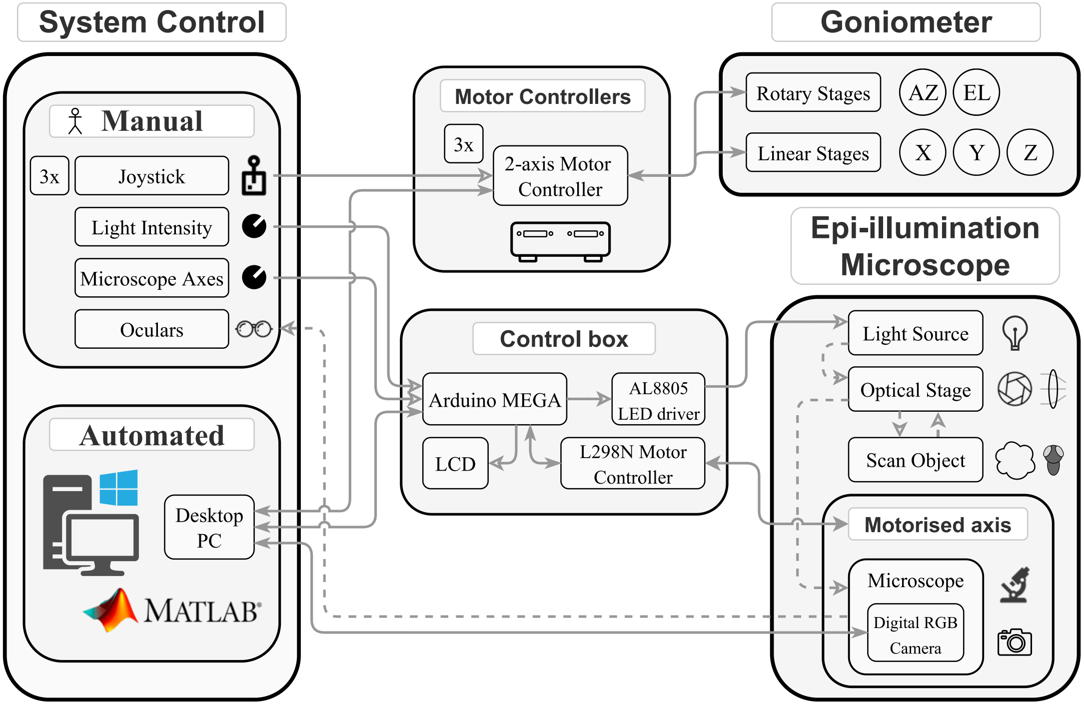

Figure 2.1: Schematic overview of the GRACE divided into subsystems, including control boxes to process electrical signals. The arrows indicate bidirectional or unidirectional paths. Solid lines and dashed indicate electrical and optical signals, respectively.

hardware or hardware controller. Using the digital interface, programmed commands can be sent to the hardware to automate the scanning procedure of an object or specimen.

### 2.1.2 Goniometer

The five-axes goniometer is build-up from a selection of linear and rotary stages, which can be controlled manually or digitally, as explained in subsection 2.1.1. These goniometer stages are presented shortly after which the irregular coordinate system (CS) of the GRACE setup is illustrated. Finally a selection of object holders is displayed.

There are three linear stages that serve to adjust the position of the object in three-dimensional space. Each linear axis corresponds to an axis of a (left-handed) Cartesian CS. Two rotary stages are used to view the object from different directions by rotating the object around the azimuth and elevation axis. The elevation axis is parallel to the $x$-axis and perpendicular to the azimuth axis. The goniometer axes are depicted in Figure 2.2.

The coordinate system of the GRACE setup is a left-handed system, which is different from the conventional right-handed CS. The left-handed CS follows from the positive directions of the rotation axes and a reversed vertical axis: the $z$-axis of the GRACE system is pointing down with respect to the optical table. A reminder about left-handed coordinate systems is given in Figure 2.3b. The Cartesian coordinate system and the rotary axes of the GRACE system are shown in Figure 2.3a.

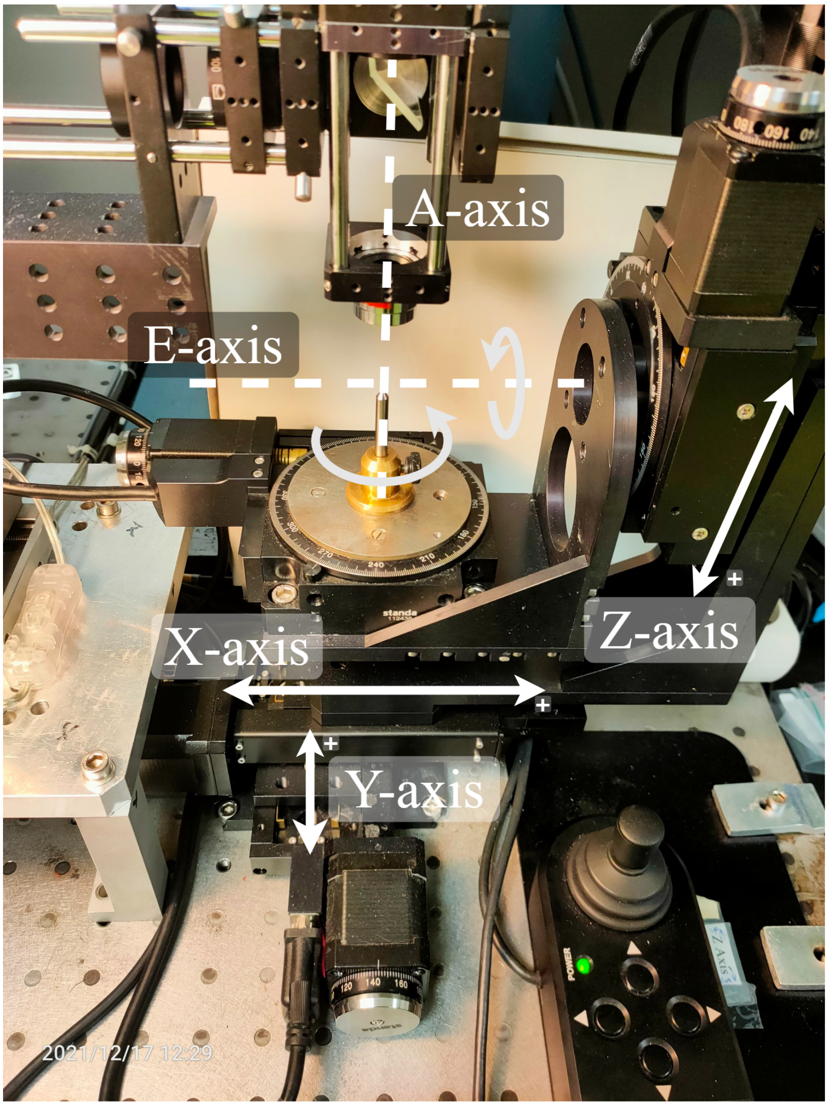

Figure 2.2: Goniometer stage with five axes. Three linear stages for a left-handed Cartesian coordinate system consisting of an $x$-, $y$- and $z$-axis. '+' indicates the positive direction for the linear axes. The azimuth (A) axis and the elevation (E) axis are the two rotational axes of the goniometer. The curved arrow indicates the positive rotational direction. All axis are motorised.

### Object Holders

A number of holds are used to orient an object in the desired position on the metal plate of the azimuth rotation stage. For specimens such as *Musca domestica* (house flies), a plastic tube is used and placed in a holder with two (or three) degrees of freedom [24]. For semi-automatic calibration purposes, an $xyz$-stage with a calibration sphere is available, see Figure 2.4b. For quick manual adjustments, to roughly align the azimuth axis with the optical axis, a centre point is available. The centre point has a bulge at the bottom, which corresponds to a hole at the centre of the metal plate. The different holders can be seen in Figure 2.4.

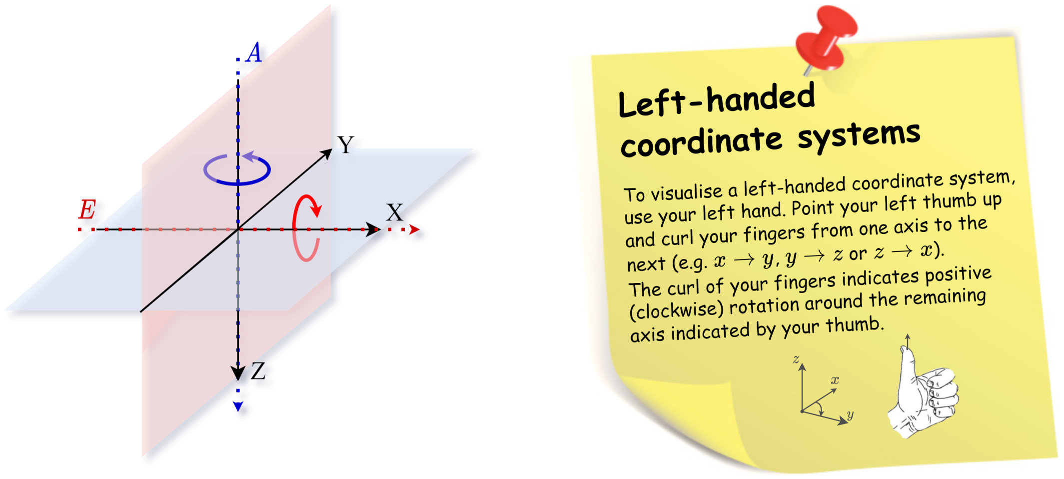

Left-handed coordinate systems

To visualise a left-handed coordinate system, use your left hand. Point your left thumb up and curl your fingers from one axis to the next (e.g. $x \to y$, $y \to z$ or $z \to x$). The curl of your fingers indicates positive (clockwise) rotation around the remaining axis indicated by your thumb.

(a) (b)

Figure 2.3: **(a)** Left-handed coordinate system of the goniometer. The plane orthogonal to the azimuth ($A$) and elevation ($E$) axis are coloured in blue and red respectively. The elevation axis is parallel to the $x$-axis, and perpendicular to the azimuth axis. Note that the azimuth plane and axis, are fixed to the elevation axis, as seen in Figure 2.2. So consequently, when the elevation changes, the azimuth plane and axis are rotated around the elevation axis. **(b)** A reminder about the definition of left-handed coordinate systems and the positive rotation directions.

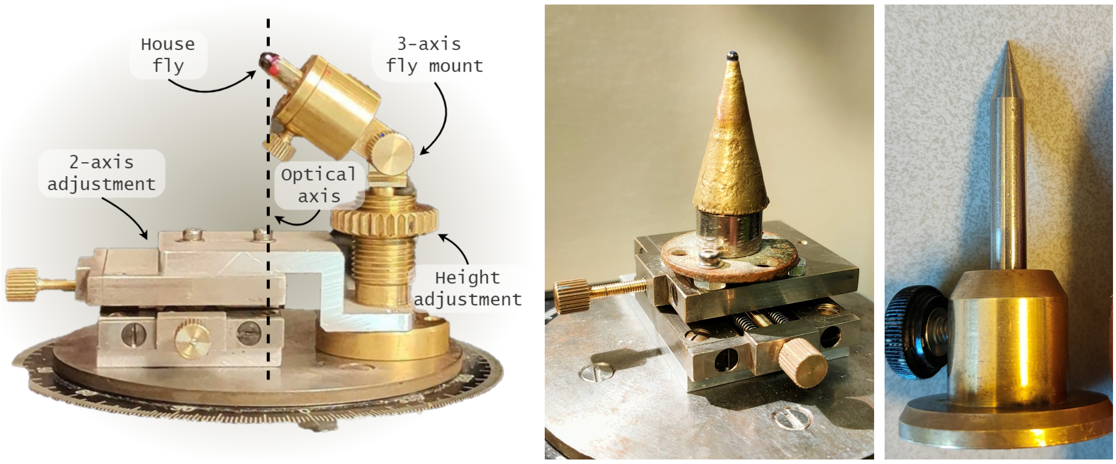

(a) (b) (c)

Figure 2.4: **(a)** 3-axis holder for a small specimen like a housefly. Optionally the specimen holder can be connected to a 2-axis adjustment stage. A similar 2-axis fly holder with slimmer, non-rotatable top part, is also available. **(b)** $xyz$-stage mounted on the azimuth table of the goniometer. A black sphere is glued at the top of the indented cone. The $x$-axis and $y$-axis alignment is adjusted by the golden thumb screws. The $z$-axis is adjusted by rotating the cone using pliers. The cone is connected to the base via a small threaded section on the inside of the cone. **(c)** Centre point for manual calibration.

### 2.1.3 Epi-Illumination Microscope

An epi-illumination microscope is used to image the object or specimen. This optical system consists of two main parts, namely an optical stage with a half-mirror and light source, and the microscope with objective lenses, oculars and a camera.

The optical stage is used to illuminate the object or specimen from the camera point of view. The light source is a white LED, of which the light is brought onto the optical axes of the microscope, by using a half-mirror [25]. The light path from the LED to the microscope, via the object under observation, is depicted in Figure 2.5.

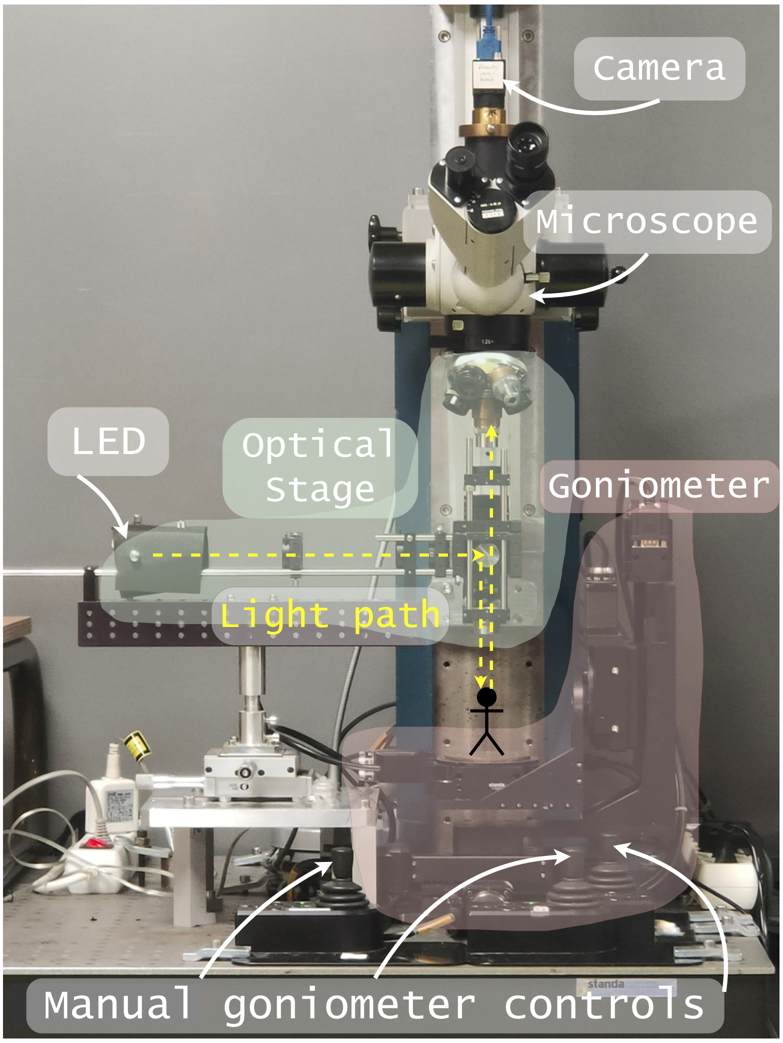

Figure 2.5: Overview of the GRACE system, consisting of a microscope with adjacent an optical stage, highlighted in green, and the goniometer, highlighted in red. The optical stage allows for the epi-illumination of the specimen using a half-mirror oriented at 45° with respect to the incident light beams. The light beams are more or less collimated when hitting the half-mirror. The general path of the relevant light beams is denoted by the dashed yellow line. The axes of the goniometer can be manually controlled by the three joysticks indicated by the arrows.

The microscope allows the user to view and capture images of the imaged object. The image capture is done by the digital camera mounted at the top of the microscope. The different objective lenses on the nose piece allow for a selection of different magnifications to be applied. The magnification of the microscope system enables relatively small objects (sub-centimetre) to be imaged across the whole image sensor. For an extensive description of the optical setup, refer to [25].

As explained above, the image size on the sensor is related to the magnification of the optical system. Besides the image size, the depth of field (DoF) is also related to the magnification by the following formula [26]:

$$DoF = \frac{\lambda \cdot n}{NA^2} + \frac{n}{M \cdot NA} \cdot e \tag{2.1}$$

Here $NA$ is the numerical aperture, $M$ is the magnification, $\gamma$ is the wavelength, $n$ is the refractive index and $e$ is the diffraction-limited resolution in the image plane.

For all measurements in this research project, a x5 objective lens chosen, unless otherwise specified. Based on (2.1) and the fact that $NA \sim M$ [26], a higher the magnification results in a smaller DoF, i.e. narrower focus range, which is beneficial for the accuracy and repeatability of the object position. However the magnification should not be to large, as it will enlarge the visual region of interest beyond the image sensor area.

## 2.2 Calibration Object

In previous projects, the Musca domestica, also known as the house fly, has been the main object of study for the development of the GRACE system [11–15, 17, 18]. However, for the verification of the methods developed in this project, a calibration object with a known geometry is required. A spherical calibration object is chosen, because of its rotational symmetry. One of the most accurate spheres that can be bought, are the ceramic ball bearings.

In the following sections is described, which ceramic ball bearing is chosen as the calibration object. In addition, the surface contamination of the ceramic balls is briefly described, in order to emphasise a point of attention when using these balls as a calibration object.

### 2.2.1 Sphere Type Selection

For the spherical calibration object, three different ball sizes of a black and a white ceramic materials are considered. A white and a black material is chosen because it is hypothesised that one of them can potentially resolve in a better image quality. A few different ball diameters are chosen, to vary the size of the observed region of interest. The size of the ball bearings is chosen to be of the same order of magnitude as the eyes of the species investigated in previous projects.

The black and white ball bearings are made from common ceramic materials, to be specific, silicon nitride ($Si_3N_4$) and zirconium dioxide ($ZrO_2$) respectively. The different ball types and their dimensional accuracy indication (ball grade) can be found in Table 2.1. The ball grade is a specification of a combination of dimensional parameters, defined by the American Bearing Manufacturers Association (ABMA) [2]. A selection of dimensional parameters, defining the roundness of the ceramic balls considered, is listed in Table 2.2.

The black silicon nitride ball with a diameter of two millimetres is selected as the calibration object. The black silicon nitride material shows less reflection outside the main circular reflection

---

[1] The accuracy of the sphere diameter and other dimensional parameters are denoted by the 'Grade' column. See also Table 2.2.

Table 2.1: Ball bearings ordered from Boca Bearing Company

| Quantity | Colour | Material | Diameter [mm][1] | Grade |
|---|---|---|---|---|
| 2 | black | $Si_3N_4$ | 1.0 | 3 |
| 2 | black | $Si_3N_4$ | 2.0 | 5 |
| 2 | black | $Si_3N_4$ | 3.0 | 5 |
| 2 | white | $ZrO_2$ | 1.0 | 10 |
| 2 | white | $ZrO_2$ | 2.0 | 10 |
| 2 | white | $ZrO_2$ | 3.0 | 10 |

Table 2.2: American Bearing Manufacturers Association (ABMA) ball grades [2]

| Grade | Sphericity [µm] | Lot diameter variation [µm] | Nominal ball diameter tolerance [µm] | Maximum surface roughness (Ra) [µm] |
|---|---|---|---|---|
| 3 | 0.08 | 0.08 | ±0.8 | 0.012 |
| 5 | 0.13 | 0.13 | ±1.3 | 0.02 |
| 10 | 0.25 | 0.25 | ±1.3 | 0.025 |

zone, compared to the white zirconium dioxide material, as seen in Figure 2.7. The choice for the black silicon nitride material is beneficial for the image analysis, since the region of interest can be better defined. A more detailed image analysis can be found in the appendix, subsection A.3.3. The diameter selection is mainly based on two criteria. The first criteria is the area of the image sensor which is covered by the reflection of the sphere. The second criteria is how much influence potential surface contamination could have on the image analysis. A diameter of two millimetres is chosen, because it showed the best compromise between the influence of potential surface contamination and the amount of available movement, before part of the illuminated circle crosses the image boundary[2].

The silicon nitride and the zirconium dioxide ball bearings are shown in Figure 2.7 and the different diameters of ball bearings are visualised in Figure 2.6. The different surface appearances of Figure 2.6 and 2.7 are explained in the next subsection. More images of all the six different ball bearings, used for the selection of the calibration object, can be found in the Appendix, subsection A.3.2.

### 2.2.2 Surface Contamination

The image processing results can be negatively impacted, if the surface of the object is mapped inaccurately. In practice, this can be caused by e.g. obstructions and contamination in the optical stage. However, another reason could be the contamination on the surface of the object of study, which is discussed in this subsection.

Contamination such as fibres and moisture can introduce image artefacts at a microscopic level, since the light is absorbed or reflected differently from contaminated areas. In turn, these artefacts affect the image analysis results, because the object of study isn't represented properly anymore. The best object mapping results are achieved if the surface of the sphere is clean,

---

[2] One could argue that a smaller magnification for the objective lens would allow for the larger ball bearing to be the best choice, because it would allow for more movement of the object on the sensor. However a smaller magnification would increase the focus depth significantly (as explained in subsection 2.1.3), which negatively impacts the focus accuracy and thereby the resolution of the obtained geometry data.

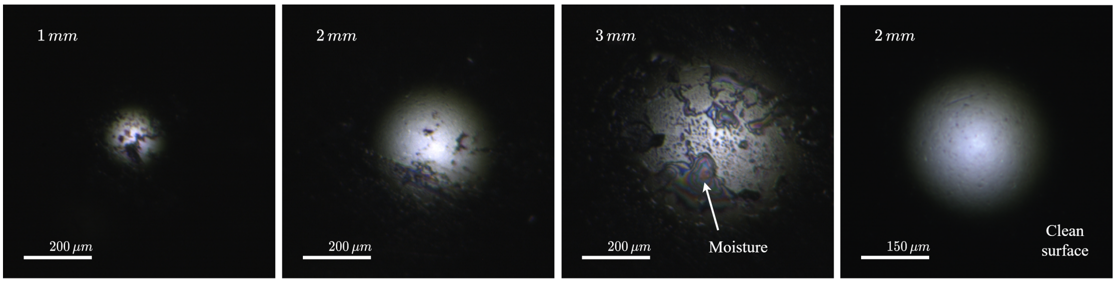

Figure 2.6: Silicon nitride ball bearings of different sizes imaged. The diameter of the ball bearings is denoted in the top left corner of each image. Their apparent size increases for the first three images, because a larger part of the collimated light beam is reflected towards the microscope.

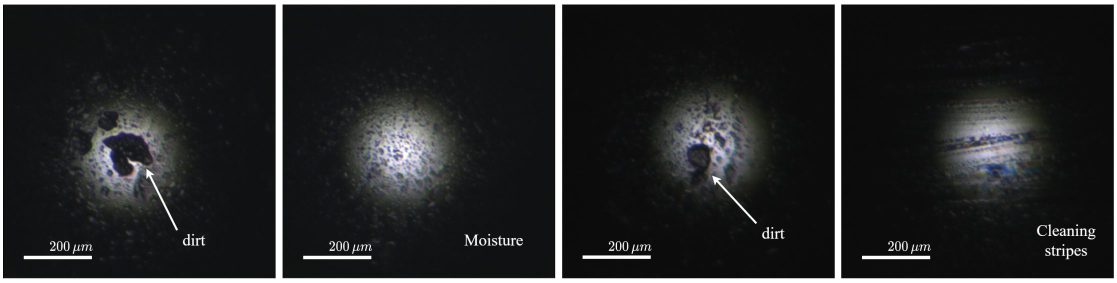

Figure 2.7: The two leftmost images display a 2 mm silicon nitride ($Si_3N_4$) ball bearing. The two images on the right are 2 mm zirconium dioxide ($ZrO_2$) ball bearings.

which results in a predictable edge of the reference object. Examples of surface contamination are shown in Figure 2.6 and 2.7. In Figure 2.6 it can be seen that, the smaller the ball bearing, the larger portion of the surface that is affected by the contamination. Figure 2.7 shows how a moisture and other sub-millimetre debris affect the image at microscopic level. The ceramic ball bearings can be cleaned with, for example, a regular white tissue. This could result in a clean surface, as displayed in Figure 2.6. However, when not performed properly, it might also result in a redistribution of dirt, or even an application of additional moisture and fibres[3].

## 2.3 Geometry Scanning

For the GRACE system, the geometry of a scanned object is represented by a point cloud. In the following sections, the distribution of the scanning positions will be described. After which, it is explained how the raw sensory data is translated into a point cloud, which accurately represents the dimensions of the observed object. Finally a small section is dedicated to describing some differences between the theoretical and practical framework.

### 2.3.1 Scanning Path

The spatial distribution of the geometry data is determined by the distribution of the sample points. The location of these sample points, depend on the orientation and geometry of the ob-

---

[3] The moisture could come from the tissue when handled with bare hands.

ject. The order in which all the sample points are scanned, is defined as the scanning path. For the scanning path, only the orientation of the object is considered. The effect of the geometry on the spatial distribution, is described in the next section.

The scanning of an object or specimen, is not only referred to as the scanning process, but also as mapping, because each combination of the two rotational angles can be mapped on a spherical surface. The standard mapping area of the GRACE system is a hemisphere, however the mapping range can be increased, such that it covers about 67 percent of a sphere[4]. The mapping range of the GRACE system is limited by the elevation range:

$$|\varphi_{lim}| \leq 110° \tag{2.2}$$

The scan path consists of a number of sample points which are defined in a spherical coordinate system. The azimuthal angle ($\theta$) and polar or elevation angle ($\varphi$), are used to represent any point in space, at a certain distance $d$, from the origin.

The default scanning path of the GRACE system, is constructed by a list of equally spaced azimuthal and elevation angles [11, 14]. This results in a non-uniform distribution of the scanning points over the surface of a sphere. In most scans, the scanning range covers a hemisphere, which is defined by:

$$\theta \in [0 : \theta_s : 360°] \tag{2.3}$$

$$\varphi \in [0 : \varphi_s : 90°] \tag{2.4}$$

Here $\theta_s$ and $\varphi_s$ are the azimuth and elevation step size. An example of a scan path with $\theta_s = 30°$ and $\varphi_s = 15°$ is displayed in Figure 2.8. The neighbouring sample points are connected by lines. The sample points are scanned in chronological order: For each azimuth position in the set (2.3), all elevation positions (2.4) are scanned. In other words, after the last elevation position, the first elevation position for the next azimuth value is scanned. The resulting number of sample points or scan locations, can be determined by multiplying the number of elements of the two sets.

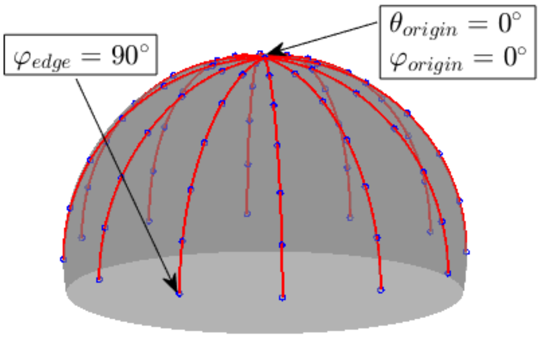

Figure 2.8: A hemispherical scan path visualised on a spherical surface. The blue markers indicate the sample points given by the sets (2.3) and (2.4) for $\theta_s = 30°$ and $\varphi_s = 15°$, resulting in 91 sample points. The origin for the rotation axes is defined at the top of the hemisphere.

---

[4] The derivation of the scannable area of a sphere is given in subsection A.2.3

At this point, only two of the five motorised axes of the goniometer are accounted for, namely the azimuth and elevation axis, which orient the object in a certain position. The function of the three linear axes is explained in the next section.

### 2.3.2 Object Position Part I

For the creation of a 3D geometry model of the object, an accurate determination of the object position is required. The object is represented by a three-dimensional point cloud, which consists of a set of sample points as explained in the previous section. The data of the three linear axes of the goniometer, in combination with the rotational information and the initial position of the object, provides us with all the information required to derive the geometry of the object. The word *derive* is important in this case, because the raw sensory data itself has to be transformed such that it represents the position of the sample points.

In this section, part one of three, the function of the three linear axes is described. In part II, (subsection 2.3.3), the required data conversion between the goniometer data and the geometrical data is described. Finally, in part III, a mathematical relation is derived to describe the object position, required for the development of the semi-automatic calibration methods, which are described in chapter 3. The mathematical object position model is not only used to adjust the position of the object before scanning, it can also be used to correct the geometry data after scanning, of which the results are shown in chapter 4.

The function of the three linear axis of the goniometer, is to align the object under the microscope. The motorised $z$-axis can adjusts the height of the object along the optical axis, to bring the surface of the object in focus. The $x$- and $y$-axis can adjust the object position in the horizontal plane, such that it is centred in the image frame. The intersection between the object's surface and the optical axis, is defined as the sample position or scanning point.

For an ideal goniometer setup, there are two main reasons why realignment of the object is required during the object mapping process:

1. The centre of the object is not aligned with the rotation centre of the goniometer
2. The object's surface shape is non-spherical

In the scenario where the scan object is a sphere and its centre is positioned on the rotation centre (RC), the apparent shape won't chance for any rotation. Thus, the sample position, positioned above the rotation centre, also will not chance.

In the scenario that only one of these cases is true, the $xyz$-data of the goniometer can be used to reconstruct an accurate shape of the scanned object. For the first case, the scan object is a sphere, were the radius from the centre to the surface is constant. In this case, the $xyz$-data describes the movement of the sphere, depicted in Figure 2.9a. In the second situation, the object is centred. The $xyz$ sensory data describes the sample positions on the object, compared to the same sample positions for a sphere. In other words, the azimuth and elevation angles describe the orientation of the surface, while the $xyz$-data describes the offset with respect to a spherical shape, as depicted in Figure 2.9b.

However, if both cases are true, the goniometer data does not accurately represent the shape of the object. In this scenario, the exact shape of the object can't be recovered from the geometrical data, without assumptions or additional data. The object position data is mixed with the object geometry data, resulting in an error of the surface mapping. This error is non-linearly related to the misalignment between the object centre (OC) and the rotation centre.

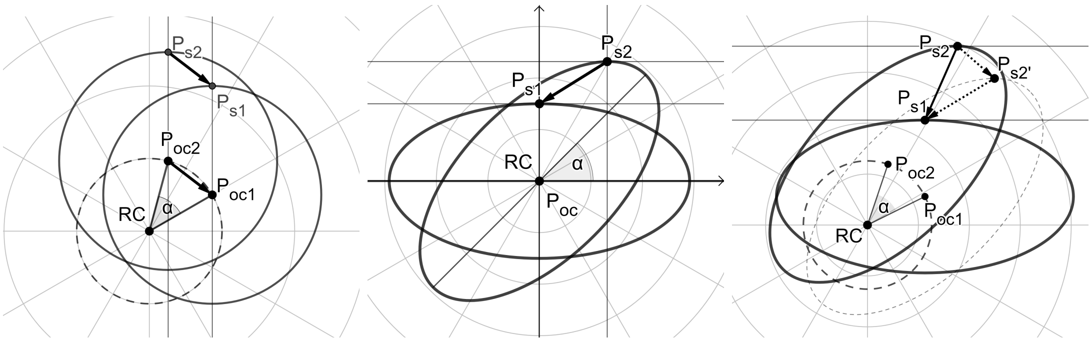

(a) (b) (c)

Figure 2.9: 2D projection of objects which need to be realigned after a rotational displacement, indicated by the shift in the sample position $P_s$. For all figures, the rotation $\alpha$ is 45°. **(a)** spherical object, OC and RC misaligned. **(b)** non-spherical convex object, OC and RC aligned. **(c)** non-spherical convex object, OC and RC misaligned. Realignment from $P_{s2}$ to $P_{s1}$ is equal to the sum of the two displacement vectors in (a) and (b), as indicated by the dotted vectors.

There is however, an elegant solution to the mixed position and geometry data problem. By describing the path of the object and subtracting this information from the geometrical data, we can effectively recover the geometry of the object. In the next two sections is described how this is accomplished.

### 2.3.3 Object Position Part II

In this section, the data conversion between the sensory data of the left-handed goniometer coordinate system, initially presented in Figure 2.3a, and a right-handed Cartesian coordinate system, used for examining the geometry point cloud data, is described.

The coordinate system of the GRACE goniometer (subsection 2.1.2) is based on the sensory data of the five axes. The axes are defined such that when the object is rotated or shifted, the resulting sensory data of the axes corresponds with the position in the coordinate system, as seen in Figure 2.10a. However, we would like to define the geometry data in a more regular right-handed spherical or Cartesian CS. By inverting the direction of the $z$-axis, a right-handed Cartesian CS is created, as seen in Figure 2.10b. Note that the elevation and azimuth definition are slightly different compared to a regular spherical coordinate system. This is required however, based on the rotation axes of the goniometer. To establish a relation between the sensory data of the goniometer CS and the position of the object, it should be considered that the goniometer axes describe the movement of the object.
In Table 2.3 the conversion between the raw sensory data from the goniometer and the position data for the geometry is given. Here $\mathrm{C_{rot}}$ and $\mathrm{C_{lin}}$ are conversion factors from motor steps $[M]$, to degrees and micrometer respectively[5]:

$$\begin{aligned} \mathrm{C_{rot}} &= \text{Rotational Resolution} = 0.6\,\text{arcmin/M} = 0.01\,°/\text{M} \\ \mathrm{C_{lin}} &= \text{Linear Resolution} = 2.5\,\mu\text{m/M} \end{aligned} \tag{2.5}$$

---

[5] Hardware details can be found in Table A.1.

Table 2.3: Relations between the raw sensory data and the position data for the degrees-of-freedom (DOF) of the goniometer coordinate system (GCS) and the right-handed coordinate system (RCS) respectively.

| **DOF** | **GCS** $[M]$ | **Conversion** | **RCS** [° **and** $\mu$m] |
|---|---|---|---|
| **Azimuth** | $\theta$ | $\theta' = \quad \theta \cdot \mathrm{C}_{\mathrm{rot}}$ | $\theta'$ |
| **Elevation** | $\varphi$ | $\varphi' = -\varphi \cdot \mathrm{C}_{\mathrm{rot}}$ | $\varphi'$ |
| **X-axis** | $x$ | $x' = -x \cdot \mathrm{C}_{\mathrm{lin}}$ | $x'$ |
| **Y-axis** | $y$ | $y' = -y \cdot \mathrm{C}_{\mathrm{lin}}$ | $y'$ |
| **Z-axis** | $z$ | $z' = \quad z \cdot \mathrm{C}_{\mathrm{lin}}$ | $z'$ |

All the data of the linear axes has to be inverted, because all the axes describe position correction movement. For example, if the object is at the position $[x, y, z]$, the required movement to align the object position with the origin is $-[x, y, z]$. However, since the $z$-axis is also flipped between the two coordinate system conventions, the sign is positive again[6]. The elevation direction is reversed, with respect to the old situation and the azimuth direction is unchanged. There are many other options for the definitions of the two rotation angles, but this option is chosen because it reassembles the measurement data the most, which keeps the process more transparent.

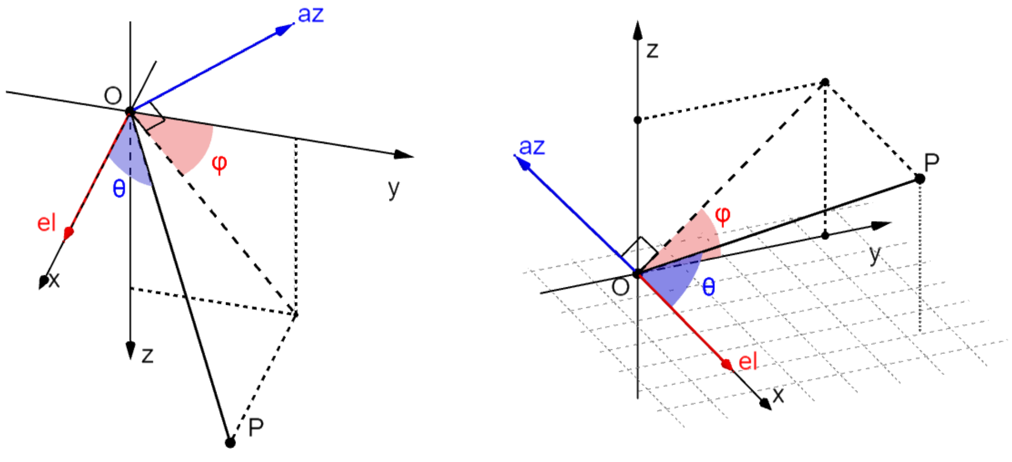

(a) (b)

Figure 2.10: **(a)** the five axes of the goniometer, similar to Figure 2.2 and 2.3a. The azimuth ($\theta$) and elevation ($\varphi$) are defined such that they represent the rotation axes of the goniometer. **(b)** A spherical coordinate system for describing the position of the object. Note that for both coordinate systems, the angles are defined in the positive direction.

### 2.3.4 Object Position Part III

When an object with an unknown shape is scanned, its centre should be at, or very close to the rotation centre of the goniometer, because only and only then, can the shape of the object

---

[6] One could argue that the z-axis of the goniometer system is already describing the height of the object, and yet it is. To refocus on a bulge on the object, the object has to move down to bring the surface of the bulge at the focal point. The explanation given in the text is equivalent, but just form another point of view.

be accurately derived from the goniometer data. In this project, methods are developed to semi-automatically centre a spherical object (the calibration object). For the development and verification of these methods, it is necessary to be able to describe the position of the object, because it influences the geometry results, as explained in subsection 2.3.2.

In this section, a complete mathematical description of the object position is presented. First the offset position is introduced, after which the object position is expressed in Cartesian coordinates, using rotation matrices. Finally, some special cases of the object position are highlighted, which are used in the semi-automatic calibration methods.

### Offset position

The initial position of all five goniometer axes is generally set to zero, to clearly mark the starting point. In reality, however, there may be an intentional or unintended difference between the initial sample point and the centre of rotation. The *intentional difference* is the distance between the object centre $P_{oc}$ and the object surface $P_{os}$, which for a sphere with radius $r_{sp}$ is:

$$D_{id}(x,y,z) = P_{os} - P_{oc} = \begin{pmatrix} 0 \\ 0 \\ r_{sp} \end{pmatrix} \tag{2.6}$$

For a non-spherical object, the (initial) sample point, may not lay precisely above the object centre. As illustrated in Figure 2.9b, the sample position relays on the orientation and geometry of the object. When the *geometry* of an object is described by the distance between the OC and the surface, the initial sample point, given the initial object orientation $(\theta_o, \varphi_o)$, is given by:

$$D_{id}(x,y,z) = P_{os} - P_{oc} = \begin{pmatrix} x_g(\theta_o,\varphi_o) \\ y_g(\theta_o,\varphi_o) \\ z_g(\theta_o,\varphi_o) \end{pmatrix} \tag{2.7}$$

When the position of the object of interest has not yet been calibrated, i.e. the OC does not match the RC, it is proposed that the orientation of the object is chosen in a way, that minimises the horizontal offset ($x_g$, $y_g$) of the initial sample point. In other words, the initial orientation of the object should be chosen such that, a line parallel to the optical axis, passes through the OC and is orthogonal to the surface.

The unintentional difference for the initial position, is defined as the distance between the object centre, $P_{oc}$, and the rotation centre of the goniometer, $P_{rc}$:

$$D_{ud}(x,y,z) = P_{oc} - P_{rc} = P_{oc} - O = P_{oc} \tag{2.8}$$

Generally, the initial sample point, also referenced as offset position, is expressed as:

$$P_0(x,y,z) = D_{id} + D_{ud} = \begin{pmatrix} x_0 \\ y_0 \\ z_0 \end{pmatrix} \tag{2.9}$$

### Position Equation Derivation

The rotation of a point around the azimuth and elevation axis, as depicted in Figure 2.10b, can be expressed by a combination of rotations around the $x$- and $z$-axis. The rotation around an axis can be expressed by a rotation matrix. The following rotation matrices can be derived from Figure 2.11:

$$R_x(\alpha) = \begin{pmatrix} 1 & 0 & 0 \\ 0 & \cos\alpha & -\sin\alpha \\ 0 & \sin\alpha & \cos\alpha \end{pmatrix} \tag{2.10}$$

$$R_z(\beta) = \begin{pmatrix} \cos\beta & -\sin\beta & 0 \\ \sin\beta & \cos\beta & 0 \\ 0 & 0 & 1 \end{pmatrix} \tag{2.11}$$

Note that these rotation matrices are only valid for right-handed systems.

The elevation axis, as seen in Figure 2.10b, is always parallel to the $x$-axis. Using (2.10), the rotation matrix for the elevation axis is given by:

$$R_e(\varphi) = R_x(\varphi) = \begin{pmatrix} 1 & 0 & 0 \\ 0 & \cos\varphi & -\sin\varphi \\ 0 & \sin\varphi & \cos\varphi \end{pmatrix} \tag{2.12}$$

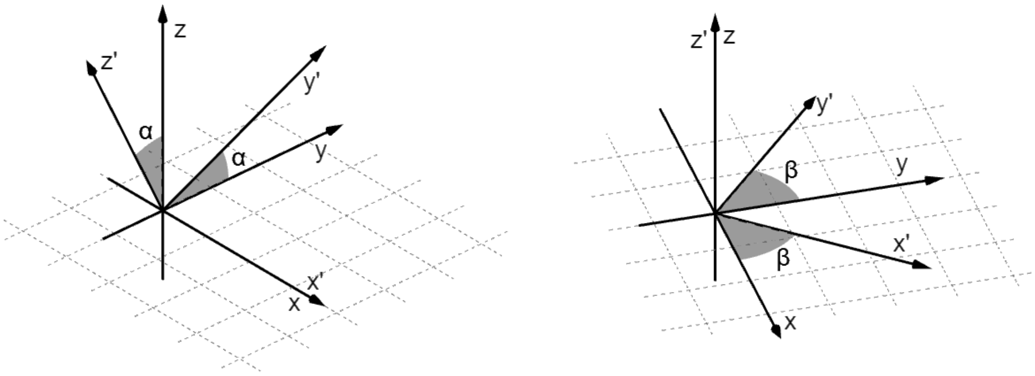

Figure 2.11: Images for assisting the derivation of the rotation matrices (2.10) and (2.11). The initial $xyz$-Cartesian CS is rotated around a primary axis resulting in a $x'y'z'$-Cartesian CS.

The azimuth axis is able to rotate around the $x$-axis by adjusting the elevation angle, as seen in Figure 2.10b. For $\varphi = 0°$, the azimuth axis is parallel to the $z$-axis. Rotating around the azimuth axis is equivalent to first setting $\varphi = 0°$, then rotating around the $z$-axis and finally rotating back to the initial position of the azimuth axis. Using (2.10) and (2.11), the rotation matrix of the azimuth axis can be expressed as:

$$R_a(\theta, \varphi_i) = R_x(\varphi_i) R_z(\theta) R_x^{-1}(\varphi_i) \tag{2.13}$$

Here $\varphi_i$ is the orientation of the elevation axis at the moment the azimuth rotation is executed. Notice that the reverse rotation is expressed by the inverse of $R_x$.

Using, (2.9), (2.12) and (2.13), the position of the initial object sample point, for any orientation $(\theta, \varphi)$ given a initial position $P_0(x_0, y_0, z_0)$, can be written as:

$$
\begin{aligned}
P_s(x_0, y_0, z_0, \theta, \varphi) &= R_e R_a P_0 \equiv R_a R_e P_0 \\
&= R_x(\varphi) R_z(\theta) R_x^{-1}(\varphi) R_x(\varphi) P_0 \\
&= R_x(\varphi) R_z(\theta) P_0 \\
&= \begin{pmatrix} 1 & 0 & 0 \\ 0 & \cos\varphi & -\sin\varphi \\ 0 & \sin\varphi & \cos\varphi \end{pmatrix} \begin{pmatrix} \cos\theta & -\sin\theta & 0 \\ \sin\theta & \cos\theta & 0 \\ 0 & 0 & 1 \end{pmatrix} \begin{pmatrix} x_0 \\ y_0 \\ z_0 \end{pmatrix} \\
&= \begin{pmatrix} x_0 \cos\theta - y_0 \sin\theta \\ x_0 \sin\theta \cos\varphi + y_0 \cos\theta \cos\varphi - z_0 \sin\varphi \\ x_0 \sin\theta \sin\varphi + y_0 \cos\theta \sin\varphi + z_0 \cos\varphi \end{pmatrix} \\
&= \begin{pmatrix} x_s \\ y_s \\ z_s \end{pmatrix}
\end{aligned}
\tag{2.14}
$$

Notice that, $\varphi_i = \varphi$, for $R_a$, because $R_e(\varphi)$ is the preceding rotation. In the case where the rotations are reversed $(R_e R_a)$, $\varphi_i$ is zero, and consequently, the result is equal.

### Special Cases For Calibration

The description for the object sample point (2.14) is only of value, if all variables are known. Something that might pose a problem is the offset location $P_0$, (2.9). The initial (zero) position of the scan object is set manually for the GRACE system, and because of this, generally, the exact location of the sample point, with respect to the rotation centre, is unknown. However, because the path of a unique sample point $P_s$ is recursive and can be described by sinusoidal functions (2.14), the initial position can be determined by mapping (part of) the spherical surface on which the sample point $P_s$ exists.

Two requirements of the scan object are suggested, for an accurate determination of the initial offset position:

1. The surface must be convex
2. A cross-section of the surface must have a line of symmetry

The first requirement ensures that in the scanning process, only a single point on the surface is orthogonal to the optical axis. A single match for each orientation is beneficial for the reliability of the data. The second requirement is necessary for the determination of the OC of a non-spherical object and is explained in detail in this section.

In (2.14), it can be observed, that only the last two arguments of the sample position ($y_s$ and $z_s$), depend on the elevation, $\varphi$. Additionally it can be seen that for $\varphi = \frac{\pi}{2} \cdot \mathrm{k}, \forall \mathrm{k} \in \mathbb{Z}$, only two arguments of the point $P_s$ depend on the azimuthal angle, $\theta$. These relations can also be determined intuitively from Figure 2.10b.

Using the microscope camera feed of the GRACE system, positional information of the object for the $x$- and $y$-axis can be easily extracted from the images of the object. To obtain $z$-axis data, the object has to be refocused for each data point, which is, compared to the image analysis for the $x$- and $y$-axis, quite a time consuming process.

For simplicity and speed, it is chosen to determine the offset position using two consecutive methods. The first method called, *azimuth calibration*, is used to determine the $x_0$ and $y_0$ offset values. For this method, described in detail in subsection 3.1.1, the elevation angle is set to zero, which reduces (2.14) to:

$$P_s(x_0, y_0, z_0, \theta, 0) = \begin{pmatrix} x_0 \cos\theta - y_0 \sin\theta \\ x_0 \sin\theta + y_0 \cos\theta \\ z_0 \end{pmatrix} \tag{2.15}$$

The first two arguments of the sample point $P_s(x_0, y_0, z_0, \theta, 0)$, $x_s$ and $y_s$, describe a circular path in a horizontal plane at height $z_0$, starting at $P_0(x_0, y_0, z_0)$ for $\theta = 0°$. By determining a number of points on this circle, the (rotation) centre can be derived, which includes $x_0$ and $y_0$.

The azimuth calibration method can be used for any scan object in the GRACE system, because the surface is only rotated around the camera-axis, and thus, the same point is sampled each time. Notice that the determination of the horizontal offset position $(x_0, y_0)$, is only of value, if it describes the offset between the OC and the RC, because we want to align those with each other[7].

Similarly, rotation around the elevation axis can be exploited to determine $z_0$. For $\theta = 0°$, (2.14) reduces to:

$$P_s(x_0, y_0, z_0, 0, \varphi) = \begin{pmatrix} x_0 \\ y_0 \cos\varphi - z_0 \sin\varphi \\ y_0 \sin\varphi + z_0 \cos\varphi \end{pmatrix} \tag{2.16}$$

When $x_0$ and $y_0$ are zero, for example, by executing the azimuth calibration method, (2.16) can be further reduced to:

$$P_s(0, 0, z_0, 0, \varphi) = \begin{pmatrix} 0 \\ -z_0 \sin\varphi \\ z_0 \cos\varphi \end{pmatrix} \tag{2.17}$$

Note that this final simplification of (2.16) to (2.17) is most beneficial if the (initial) sample point lays above the object centre, because only the $z_0$ offset described in (2.17).

Note that, for the elevation calibration, the sample point on the surface of the object does change, compared to the azimuth calibration, because the object is rotated around an axis non-parallel to the viewing direction of the camera. In (2.17), $z_0$ is a constant, which only holds for an object with equal radius along the scanning cross-section, such as a sphere or an ellipsoid at a particular orientation.

Earlier in this section, a requirement for the scan object is suggested, namely that a cross-section of the surface has a line of symmetry. In case of a non-circular cross-section, $z_0$ from (2.17) is not a constant anymore. At each angle $\pm\varphi$, the height offset $z_0$ is multiplied with an (initially) unknown multiplier. There are many possible solutions[8] to estimate $z_0$ (and $y_0$ in case of (2.16)), based on a set of symmetry points, but that is out of the scope of this project[9].

In chapter 3, the semi-automatic azimuth and elevation calibration methods, which use on (2.15) and (2.17), are explained in detail. Additionally a method is developed, using (2.14), to *correct*

---

[7] Notice that this is also the reason why, earlier in this section, (for a non-spherical object) "it is proposed that the orientation of the object is chosen in a way, that minimises the horizontal offset ($x_g$, $y_g$) of the initial sample point".

[8] Possible solutions for the determination of $z_0$ might involve the estimation of the amplitude of a circle, which touches the mapped cross-section on the inside and or outside, depending on the shape. Assuming (2.16), which requires the determination of $z_0$ and $y_0$, this problem might be a nice braincracker optimisation problem.

[9] This project focuses on establishing a working and well documented basis for geometry scanning, using a spherical calibration object to verify the results and discover possible points of attention

the geometry data, in case an object was scanned with a offset position, which is known. This post process geometry correction method is described in section 3.3, and the results, shown in section 4.4, are quite interesting.

### 2.3.5 Goniometer Rotation Axes Misalignment

Up to this moment, the goniometer setup has been considered an ideal goniometer. In this section, some practical non-ideals about the goniometer setup are shortly discussed. This is not a very detailed or well documented analysis and just reports on possible points of attention that have been discovered during the project. Specifications of the rotation stages such as, eccentricity, wobble and backlash are not taken into account and are not investigated, because these are assumed to have negligible effect[10].

With the newly added geometry scanning capabilities to the GRACE system, geometrical accuracy has become more important. It is hypothesised that, besides the calibration of the object position, the calibration of the goniometer setup itself could be responsible for most geometrical inaccuracies measured, using the reference object. Assumptions about right angles and intersecting axes are made, however measurement have shown that some of these assumptions can not be taken for granted.

During the installation and calibration of the goniometer setup, a number of critical calibration points for the axes of the goniometer were found:

1. The intersection of the azimuth and elevation axis
2. The right angle between the $x$- and the $y$-axis
3. The orthogonality of the $z$-axis with respect to the optical table
4. The orthogonality of the azimuth axis with respect to the optical table (for $\varphi = 0°$)
5. The orthogonality of the optical axis with respect to the optical table

Most parts of the goniometer setup are relatively easy to verify and adjust[11]. However point one and point three brought some difficulties. The error in the orthogonality of the $z$-axis is a small enough, but measurable, physically and in the geometry data.

The intersection, or rather, the absence of an intersection between the rotational axes of the goniometer, has a direct effect on the obtainable accuracy of the raw geometrical data. The offset distance $y_m$, as depicted in Figure 2.12, influences the accuracy of the developed calibration methods for the correction or determination of the initial position. The error $y_m$ can be determined using the developed azimuth and elevation calibration methods. This goniometer calibration procedure is described in section 3.2. The goal of this method is to minimise the $y_m$ error, which depends on the accuracy of manual adjustments on the goniometer setup, using the image frame as a measurement device. Results about the realignment of the rotation axes is reported in section 4.3.

---

[10] The stability related specification of the linear and rotational stages can be found in for example the STANDA product catalogue [27], using the part number found in subsection A.1.1.

[11] As a reference and guide, images are provided in subsection A.3.4, showing some of the parts being calibrated and their reference surfaces.

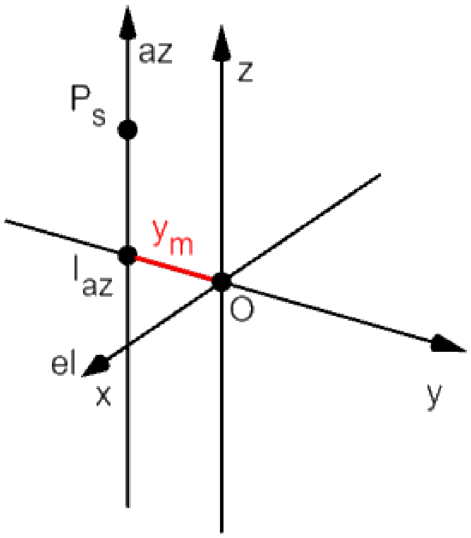

Figure 2.12: Identification of the non-zero distance between the two rotational axes of the goniometer of the GRACE system.

# Chapter 3

# Methods

GRACE, the goniometric research apparatus for compound eyes, is developed to obtain properties of compound eyes in an automated manner. For example, the automated charting of the visual space of insect compound eyes [7].

New methods are developed to obtain the geometrical properties of scanned objects. A point of attention is the reference point to which the obtained geometrical data is related, since this changes the obtained measurement data, as described in the previous chapter. To summarise: in practice, there is an error between the geometrical reference point of the object and the desired reference point. Calibration methods are developed to minimise the error between the actual and desired reference point, to obtain an accurate representation of the geometry of the object.

In this chapter, four methods are presented. In the first section, the two object position calibration methods are described in detail. Then, a section is dedicated to a method, which can be used to re-calibrate the two rotation axes of the goniometer, crucial for the accuracy of the data, as described in subsection 2.3.5. The final section describes a data correction method.

## 3.1 Semi-Automatic Object Calibration

Semi-automatic object calibration methods has been developed to increase the accuracy and reliability of the geometry data as well as the effective repeatably of these scans. The results enable new methods to be implemented, for example, a method to obtain accurate 3D models of compound eyes.

As described in section 2.3, the object position calibration has been split into two consecutive methods. The first methods, aligns the position of the scan object on the azimuth axis, while the second method aligns the position of the scan object on the elevation axis. These methods are semi-automatic, meaning there are some manual steps to be performed. In the following two subsections, the calibration methods are described up to a point, which should allow for an experienced operator of the GRACE system, to execute them successfully.

### 3.1.1 Azimuth Calibration Method

In this section, the azimuth calibration method is presented used to align the centre of an object on the azimuth axis. This section describes the start conditions, execution and results of the azimuth calibration function[1]. The azimuth calibration function is applicable to a variety of scan

---

[1] `CalibrationAZaxis_JJ` can be found at [1]

objects, as described in subsection 2.3.4.

A flow diagram is presented in Figure 3.1, which shows the semi-automatic process for calibration of the azimuth axis. Some conditions have to be met before calling the function:

- The GRACE setup should be initialised.
- The object should be roughly centred, such that it stays fully or partially[2] within the ROI while making a 360° turn around the azimuth axis.
- The azimuth plane, should be perpendicular to the optical axis. In other words, the elevation has to be set to 0°.
- The object's surface should be in focus and (ideally) be free of contaminations[3].
- The object should be the only distinguishable object in the ROI at all times[4].

The semi-automatic process summarised: the azimuth calibration function rotates the object at constant speeds, while taking images, for a full rotation around the azimuth axis. The object's centre of these images is determined on the fly and stored. After the full rotation, the current object centre, $P_{oc}$, is set manually by the user by clicking on the desired position in the interactive window that has appeared. This step is chosen to be performed manually, to enforce user interaction and verification of the results. But, this step can also be performed automatically.

Because the object has been rotating at constant speed, and the time between each image taken is about equal, the rotation centre can be calculated by taking the average of all the sample points, described by (2.15):

$$P_{rc\_a}(x_r, y_r, z_0) = \overline{\mathbf{P_s}(x_0, y_0, z_0, \theta_\mathbf{c}, 0)} = \begin{pmatrix} \overline{x_0 \cos\theta_\mathbf{c} - y_0 \sin\theta_\mathbf{c}} \\ \overline{x_0 \sin\theta_\mathbf{c} + y_0 \cos\theta_\mathbf{c}} \\ z_0 \end{pmatrix} = \begin{pmatrix} \overline{\mathbf{x_c}} \\ \overline{\mathbf{y_c}} \\ z_0 \end{pmatrix} = \begin{pmatrix} x_r \\ y_r \\ z_0 \end{pmatrix} \tag{3.1}$$

Here $\theta_\mathbf{c} = [\theta_1 : \theta_{step} : \theta_n]$, were $\theta_1$ is the first position for which $\theta > 0°$, $\theta_n$ is the last position for which $\theta < 360°$ and $\theta_{step}$ is approximately the angular speed multiplied by the time between the capture of two images. The subscript $r$, of $x_r$ and $y_r$ denotes that these are coordinates *relative* to the current CS for which the origin doesn't necessarily lay at the intersection of the two rotation axes[5]. The sets $x_c$ and $y_c$, are the $x$- and $y$-coordinates determined by the image analysis function for all the images of the object.

The movement required to centre the object on the azimuth axis, $\vec{v}_a$, is the difference between the current location $P_{oc}$ and the determined location of the azimuth axis:

$$\vec{v}_a(x, y) = P_{rc\_a} - P_{oc} \tag{3.2}$$

After the current position of the object is determined and the azimuth calibration function has determined the required movement of the object, the movement of the object should be

---

[2] If the object only stays partially within the ROI, the functions should be run twice since the object's centre can't be detected accurately for all azimuth positions.

[3] It should be noted that the function used to determine the sample point, is made for the calibration object (section 2.2).

[4] If (a part of) the object isn't distinct enough from the background, the function that determines the centre of the calibration sphere isn't able to produce an unambiguous result.

[5] The origin of the Cartesian CS is usually depicted at the intersection of the two rotation axes. However, because the origin is defined manually, it may actually differ from the intersection of the rotation axes. This is not a problem during calibration, because the movement relative.

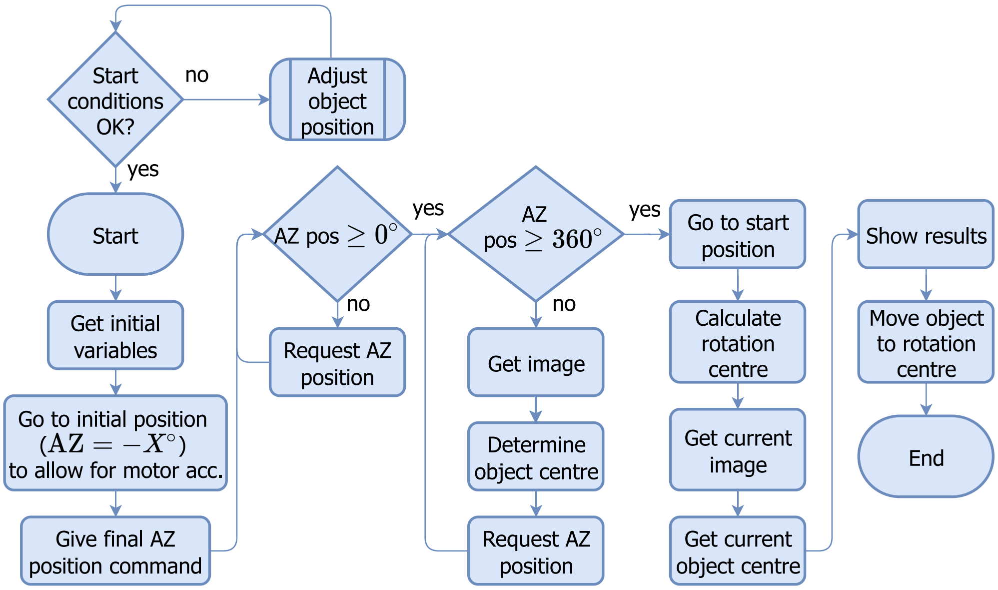

Figure 3.1: Flow diagram of the azimuth calibration process using the `CalibrationAZaxis_JJ` function [1].

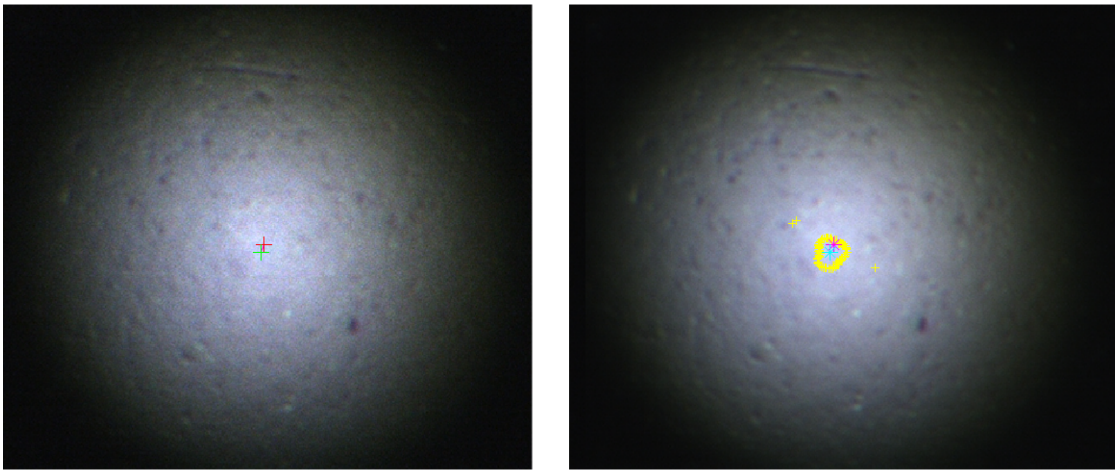

Figure 3.2: Middle section cut-out of the results screen presented at the end of the azimuth calibration procedure. Markers are present for the current object centre (red), the object centres during rotation around the azimuth axis (yellow) and the determined rotation centre (green and cyan on the left and right, respectively). It can be seen in the right image that the object is already almost centred perfectly on the azimuth axis because the yellow markers are close to the cyan marker. The (manually set) OC (red) is near the yellow markers. This indicates coherence between the automatically determined OCs and manually defined centre.

performed. This is a manual step, because the object mount is not motorised. The user is provided with a live view of the object and markers to indicate the current position of the object

(red), goal position (green) and scan results (yellow), as seen in Figure 3.2.
Note that function doesn't require any inputs, and all input variables are automatically retrieved if the GRACE setup is initialised. Specifics can be found in the function code at [1]. The results of this method, applied to a non-centred object, are analysed in section 4.3.

### 3.1.2 Elevation Calibration Method

In this section, the elevation calibration method is presented used to align the centre of an object on the elevation axis. This section describes the start conditions, execution and results of the elevation calibration function[6].

As for any point rotated around an axis, the OC rotated around the elevation axis, describes a circular path. The difference for the elevation calibration, compared to the azimuth calibration, is that the sample point $P_s$ is not a fixed point on the object anymore. The sample point changes position, because the object is rotated around an axis, which is non-perpendicular to the optical axis. The sample point moves over a cross-section of the object, which intersects with the optical-axis and is orthogonal to the elevation axis. For the GRACE goniometer setup, as depicted in Figure 2.10a, this is the $yz$-plane. The cross-section of the object should be suitable for determining the OC. As described in subsection 2.3.4, the easiest cross-section is circular.

The elevation calibration function is designed to map the cross-section of the scan object. From the results, the object offset position in the $yz$-plane is determined.

A flow diagram is presented in Figure 3.3, which shows the semi-automatic process for calibration of the elevation axis. Some conditions have to be met before calling the function:

- The GRACE setup should be initialised.
- The object's surface should be in focus and centred in the image frame.
- The azimuth axis should be parallel to the optical axis, i.e. $\varphi_{start} = 0°$.
- The object should be roughly centred, such that it stays (partially) within the ROI, for all discrete subsequent elevation steps.
- The scan parameters, such as the focus range and elevation step size should be set appropriately[7].
- (optionally) it is recommended to have the object centred on the azimuth axis, such that (2.17) instead of (2.16) holds.

The semi-automatic process is summarised: the elevation calibration function moves the object around the elevation axis. The object is centred and focused, after which the sample point is stored. This process is repeated for all specified object elevation orientations[8]:

$$\varphi_{\mathbf{c}} = [-90° : \varphi_{step} : 90°] \tag{3.3}$$

When the scanning process is finished, the results of the $y$- and $z$-axis is visualised in a plot. To determine the initial offset position $P_s$ in the $yz$-plane $(y_0, z_0)$, as for example described by

---

[6] `CalibrationELaxis_JJ` can be found at [1]

[7] The focus range parameter should be set to at least twice the maximum height difference that can occur between the discrete elevation steps for the specified range.

[8] Note that a larger elevation range helps with the accuracy of the function fitting of the results, however the object might limit the usable range. If possible, a range of about half a rotation is found appropriate.

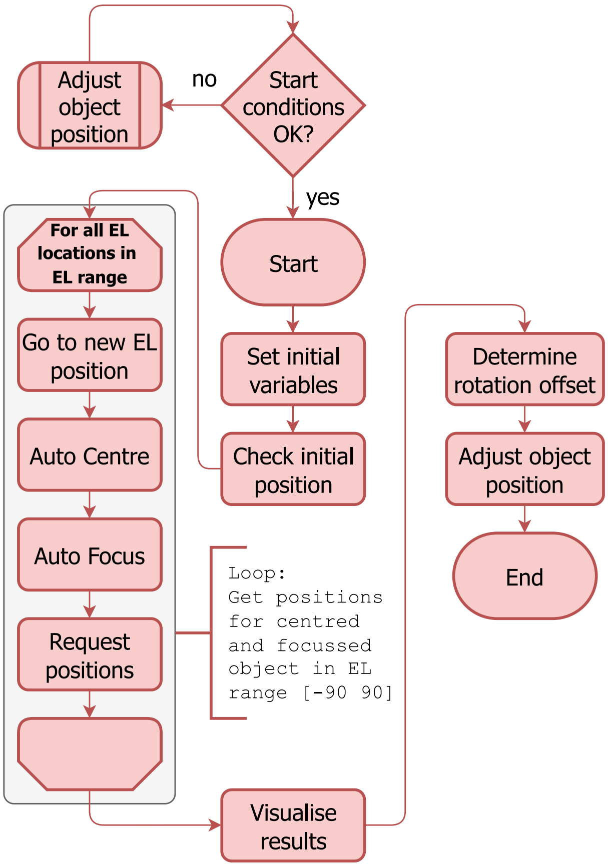

Figure 3.3: Flow diagram of the elevation calibration process using the `CalibrationELaxis_JJ` function [1]. The start conditions are met using well-known manual or automated methods. When these are met, the function can be started. When completed, the final (movement) step for the calibration object is done manually as described in section 2.1.2.

(2.16), we make use of function fitting. By simulating the results for spherical calibration object, the approximate offset-position can be determined[9].

The offset position can either be corrected, or it can be recorded such that the geometrical data can be adjusted afterwards by the post-process correction methods, described in section 3.3.

The manual adjustment of the object is potentially more difficult than for the azimuth calibration method. If the object has to be moved in the direction parallel to the optical axis, a static camera feed can not be used during the manual alignment, because the object will be moved out of focus.

In subsection A.2.1 a workflow can be found, (manual) horizontal and vertical object adjustment step, the final step of the semi-automatic elevation axis calibration method.

---

[9] A MATLAB live script called `Visualization_RC_errorv4`, found at [1], is made to simulate the results of the elevation calibration method for a spherical object. Note that in this script, the offset position of the object is given by a radius and an elevation offset angle. This makes it easier to match the measured results of the elevation calibration method. Note that the measurement data is the raw sensory data of the goniometer and thus doesn't directly describe the position of the object as described in subsection 2.3.2 and 2.3.3.

The elevation calibration function doesn't require any inputs[10]. All input variables are automatically retrieved if the GRACE setup is initialised. Specifics can be found in the function code at [1]. The results of this method, for the non-centred spherical calibration object, are found in section 4.2.

## 3.2 Goniometer Rotation Axes Calibration

The alignment of a scientific setup can be quite tedious and there has been no record for the calibration of the GRACE setup so far. In subsection 2.3.5, the alignment of the goniometer axes themselves is shortly discussed, which concluded that the alignment between the two rotational axes is critical for the accuracy of the geometrical data.

In this section, an alignment procedure for the two rotational axes based on the azimuth and elevation calibration methods is described. This method can be used to (re)align the rotational axes of the goniometer, using the spherical calibration object as depicted in Figure 2.4b. In order to make the goniometer calibration description unambiguous and concise, it is assumed that the other parts of the goniometer can be considered as an ideal setup[11].

### 3.2.1 Alignment possibilities

Before the goniometer rotation axes calibration method is described, first the two possible alignment options for the statically mounted elevation and azimuth axis are described.

The alignment between the two rotational axes of the goniometer can (only) be adjusted by exploiting the available play in the bolt mounts of the static connections. In Figure 3.4 it can be seen that for mounting the azimuth stage, there are three bolts which mount the azimuth stage to the right-angle bracket. The right-angle bracket is again mounted to the elevation stage with four bolts.

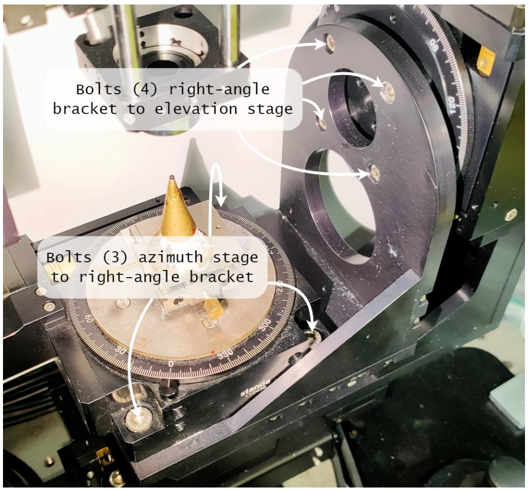

Figure 3.4: Indication of the bolt locations of the azimuth stage and the right-angle bracket with which the azimuth stage is connected to the elevation stage.

---

[10] Some variables are hardcoded and adjusted inside the function as it was still in the development phase.

[11] In subsection 2.3.5, the orthogonality of the $z$-axis is also noted to be non-ideal, however, in this case, this isn't of any concern for the misalignment between the two rotational axes, $y_m$, because the $z$-axis approximately perpendicular to the $y$-axis.

When loosening the bolts of either the azimuth stage or the right-angle bracket, the alignment between the two rotational axes can be adjusted. The azimuth stage is naturally supported by the right-angle bracket, which make it the easiest option for adjustments. There is however a limit to the available play in the bolted connection, which might make it necessary to remount the right-angle bracket. Note that when (re)mounting the right-angle bracket, the azimuth stage should be perfectly horizontal for the elevation value of zero degrees[12].

### 3.2.2 Rotation Axes Alignment Method

In this section, it is described how the alignment offset between the two rotation axes of the GRACE goniometer is determined and how to resolve it. A flow diagram is provided and explained in detail.

To determine the misalignment of the rotation axes, the location of the axes must be determined in a reference frame. The location of the axes is determined using the spherical calibration object (section 2.2) and the azimuth and elevation calibration methods (section 3.1). An overview of all the steps involved is visualised in a flow diagram, Figure 3.5. The whole process consists of two main parts, namely the determination of the offset between the rotation axes and the adjustment of the setup to reduce the error.

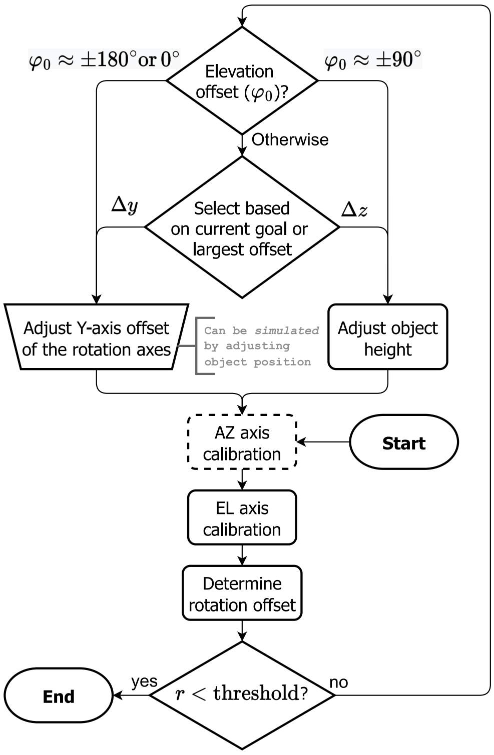

Figure 3.5: Flow diagram of the goniometer calibration method. The box with a dashed line is optional, because if, for example, only the height of the object is changed, it is unnecessary to run the azimuth calibration again.

---

[12] A temporary support on the optical table can be used to keep the bracket horizontal.

The preparation consists of mounting the spherical calibration object on a suitable $xyz$-stage which is securely placed on the azimuth stage.

The azimuth calibration method is used to centre the calibration object on the azimuth axis. If properly centred, the horizontal alignment errors for the $x$- and $y$-axis should be about zero[13], under the assumption of intersecting rotation axes.

Using elevation calibration method, the offset position of the calibration object in the $yz$-plane is determined. If the $y$ component is non-zero[14], there is an alignment error between the two rotation axes, as depicted in Figure 2.12.

Based on the determined offset position in the $yz$-plane, which lays at distance $r$ from the origin with an offset angle of $\varphi_0$, a choice should be made. It can be attempted to either adjust the $y$-axis offset of the rotation axes, or, the object height can be adjusted.

*Right option:* when the elevation offset angle ($\varphi_0$) is close to ±90°, the accuracy of the $y$-axis offset might not be accurate enough. For small changes in the estimated offset angle, the $y$-axis offset position varies relatively much. For an accurate determination of the $y$-axis offset, it is advisable to operate near the symmetry points, as indicated in Figure 3.6. So, based on the current offset angle, it might be more beneficial to first adjust the height of the calibration object[15] to achieve a more accurate value for the $y$-axis offset.

*Left option:* when the elevation offset angle ($\varphi_0$) is close to zero or ±180°, the largest contribution to the current object offset position is made by along the $y$-axis. The contribution made by the $z$-axis is about zero, as can be seen in Figure 3.6. In subsection 3.2.1 the alignment possibilities of the $y$-axis are described. To adjust the $y$-axis micrometer offset in an accurate and controlled approach, multiple steps are involved. In subsection A.2.2 these steps are described.

After the adjustments of the goniometer setup, verify the results by evaluating the results of the elevation calibration procedure again. The azimuth calibration procedure is optional, because it is only relevant if the calibration object has been moved along the $x$-axis. Dependent on the achieved calibration results, it can be decided to do multiple iterations to fine-tune the results.

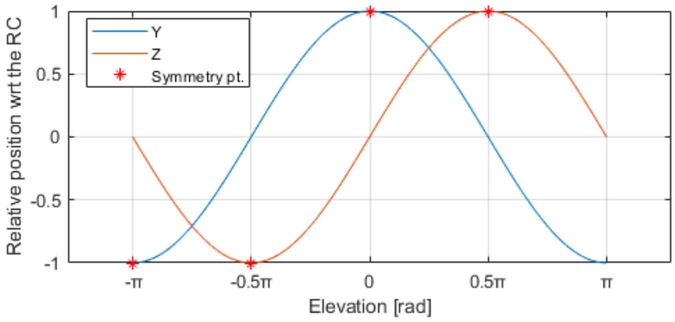

Figure 3.6: Visualisation of a point rotating around the elevation axis, starting on the $y$-axis for $\varphi = 0$. Four points of symmetry exist, indicated by the (red) star markers, two for each axis.

Notice that in Figure 3.5 it suggested that the $y$-axis offset can also be *simulated*. By adjusting the object position along the $y$-axis instead of adjusting the goniometer setup itself, allows the operator to test the result of a certain adjustment without actually adjusting the goniometer

---

[13] A target value could be less than 10 $\mu$m for example.

[14] I.e. other than the $y$-axis offset determined after executing the azimuth calibration method

[15] When mounted on the $xyz$-stage, Figure 2.4b, pliers can be used to adjust the height.

itself. An additional benefit is that more calibration attempts[16] can be finished within in a given time, beneficial for adjusting the height of the object.

Another use of this method is to establish a performance baseline of the GRACE setup, using the known geometry of the spherical calibration object. Additionally dependent on the accuracy and assumptions, orientation dependent behaviour of the setup could also be characterised.

## 3.3 Post-Process Correction Method - SEER

In some cases, the initial position error of an object scanned with the GRACE system can be larger than desired. A positional error causes the geometrical data to be morphed in a non-linear fashion, resulting in a shape which doesn't accurately represent the scanned object.

The post-process correction method can be used to correct geometrical data of an object, which was positioned at an offset position during geometry scanning. The OC offset location can be described by (2.14), when $P_{oc} = (x_0\ y_0\ z_0)'$.

In the post-process correction method called spherical error estimation and reconstruction (SEER), (2.14) is used to calculate the expected position of the OC, at all sample positions. The main application of the SEER method, is to correct geometrical data of objects scanned at known offset positions. Other applications could be the determination of the geometry scanning characteristics of the GRACE setup, using a known calibration object.

Using the spherical calibration object and the SEER method, visualised in a flow diagram in Figure 3.7, raw sensory data from the goniometer is processed and the differences between the expected results and the measurements are determined[17]. The results are discussed in chapter 4

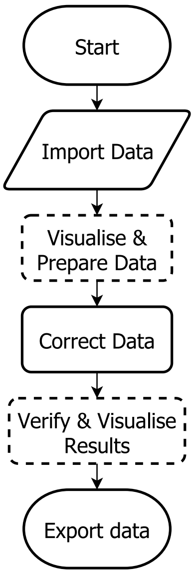

Figure 3.7: Spherical error estimation and reconstruction (SEER) method. The boxes with the dashed lines indicate that it is an optional step.

---

[16] Multiple attempts are probably needed, because it is assumed the object position and goniometer adjustments are all done manually. The adjustments are relatively susceptible to human error, because it is expected that the adjustment resolution required lays in the range of 1-20 micrometer.

[17] MATLAB scripts starting with `SEER_JJ_scratchv4_data` implement the SEER method. No separate script exists (yet) for this method.

# Chapter 4

# Results & Analysis

In this chapter, the results of the developed methods are described and analysed. Maintaining the presentation order of chapter 3, first, the azimuth and elevation calibration results are presented. Thereafter, the calibration results of the goniometer setup are analysed and discussed. The chapter is concluded by a number of scan results of the calibration sphere: in subsection 4.4.1, the geometry scan results are presented for a very well centred spherical calibration object, revealing an object orientation dependency in the results. In subsection 4.4.2 - 4.4.4 the morphed shape of the spherical calibration object is presented, caused by the non-ideal offset position of the object. It is shown that by using the SEER method (section 3.3), the expected geometry of the calibration object is recovered. Based on the data presented, the performance of the GRACE system is characterised.

## 4.1 Azimuth Calibration

In this section, an example is given of the result that can be achieved by using the azimuth calibration method. The results of this method may vary dependent on the accuracy of the manual object position adjustment, as indicated in the method, subsection 3.1.1.

After the initial conditions for the azimuth calibration method are met, the procedure can be initiated. Within a minute, the user is presented with a scan-result screen[1], similar to Figure 4.1.

In the right window of Figure 4.1, an image of the current object position is presented, with an overlay of the obtained data. The yellow markers indicate the object centres, obtained during the movement of the object around the azimuth axis. The cyan marker, indicates the rotation centre (RC) determined from the yellow markers. The object centre (OC), obtained after scanning, is indicated by the magenta marker and is used as a manual verification of the results as described in the method.

It can be seen that the yellow markers are equally spaces, indicating that the time required to capture and image and determine the OC is about constant, which is required for the azimuth calibration method. Additionally, it can be observed that the current OC, indicated by the magenta marker, is very close to the circle drawn by the yellow markers. The closer the magenta marker is to the first and last yellow marker, the more agreement between the obtained OCs and the manually determined OC there is. For reference, the distance between the OC and RC displayed in Figure 4.1, is about 300 pixels or 220 $\mu$m.

---

[1] Potential manual steps might be involved for setting the object centre, dependent on the function settings.

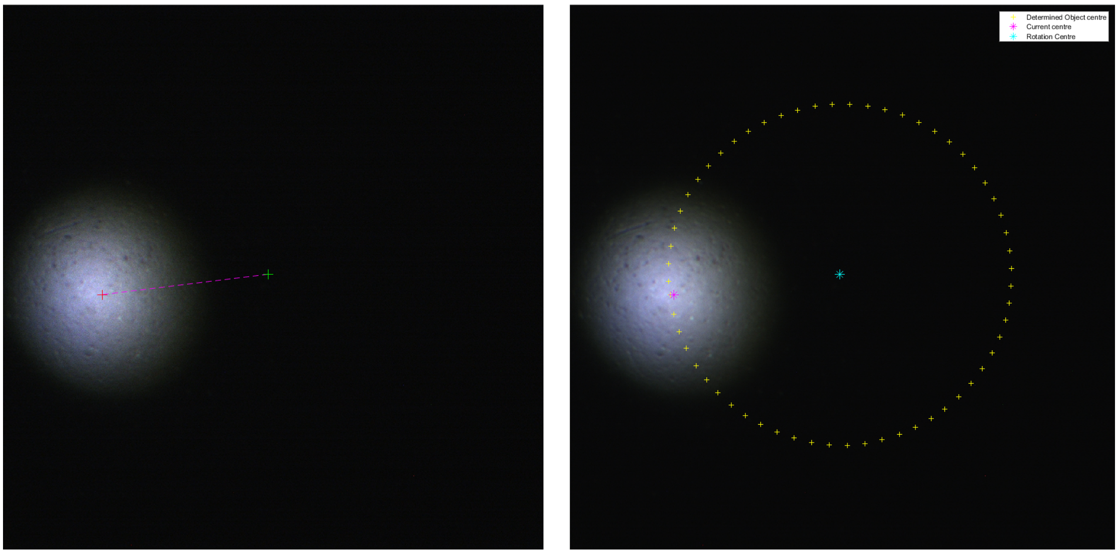

Figure 4.1: Result of the azimuth axis calibration method. Left, the live preview of the digital camera. Right, a snapshot with the results of the calibration procedure. Markers are present for the current OC (red/magenta), the OCs during rotation around the azimuth axis (yellow) and the determined location of the RC (green/cyan). The dashed magenta line between the red and green marker indicates the direct path between the current location of the OC and the RC. For reference, the image resolution is 1100 pixels (818 $\mu$m) square.

The left window of Figure 4.1, is a live preview, used during the (manual) adjustment of the object. The red and green marker show the current and ideal position for the OC, and are equivalent to the magenta and cyan marker. The dashed magenta line indicates the direct path between these markers. In other words, the dashed magenta line indicates the direct path between the OC and the location of the azimuth axis.

The position adjustment of the calibration object in the $xy$-plane, is made using the thumbscrews on the $xyz$-calibration stage, see Figure 2.4b. The live-preview window shows the position of the object during the position adjustment. To verify the (manual) object position adjustment made, the azimuth axis calibration function can be rerun.
Figure 4.2 shows the result of the azimuth calibration function, after the object centre is positioned close to the azimuth axis. Note that the ROI of the image frame has been reduces compared to the previous image. The ROI is only reduced for illustrative purposes.

It can be observed that the yellow markers are all located in a small neighbourhood, compared to the size of the (visible part of the) object. The shape drawn by the yellow markers isn't fully circular anymore, but there are no outliers and the results look very stable. The radius or average distance between the yellow markers and the cyan marker, representing the RC, is very small: all yellow markers fit within a circle with $r = 15$ pixels. This indicates that the alignment of the spherical calibration object and the azimuth axis only has an error of about 10 $\mu$m.

When the positional accuracy of the (calibration) object is as accurate as shown in Figure 4.2, where the yellow markers are all very close to the RC and they are also still able to display an circular-like path. The location of the manually set object centre (magenta/red), used for alignment purposes, might be taken with a pinch of salt. A small estimation error for the manually set OC is expected. Ideally, the magenta marker is on the circular path of the yellow markers and the yellow markers indicate the exact centre of the reference object.

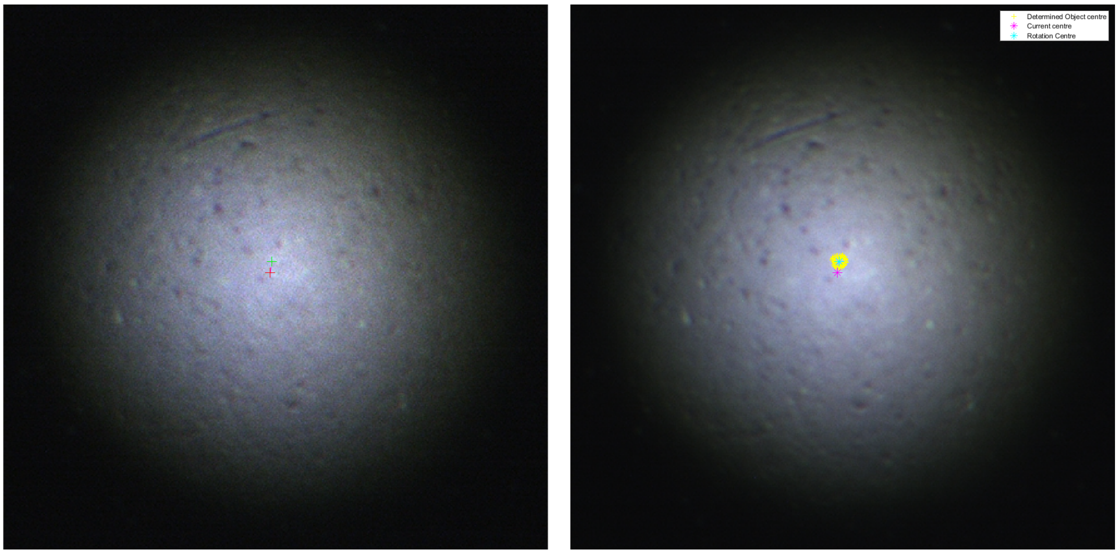

Figure 4.2: Azimuth calibration result, after (repeatedly) aligning the object centre with the rotation centre. Image resolution 400 pixels (297 $\mu$m) square. The white box in the top right corner is a legend for the right plot.

## 4.2 Elevation Calibration

In this section, first a short recap about the measurement quantity is given. Thereafter, the results of the elevation axis calibration method are presented and analysed. In the discussion, chapter 5, some notes are found about the execution of the function in different conditions. Most steps of the elevation calibration method (subsection 3.1.1) are performed automatically. However, as for the azimuth calibration method, some manual steps are required for the repositioning of the scan object. For all elevation calibration results presented in chapter 4, the object centre is located on the azimuth axis, unless otherwise specified. This eases the analysis of the results due to the reduced DOF, as shown in subsection 2.3.4.

Recall from chapter 3, that the calibration for a rotation axis is performed by rotating an object around the axis and recording the position of the sample point. Based on the coordinate system of the GRACE setup (Figure 2.3a, 2.10a), the position of the sample point $P$, rotated around the elevation axis, can be described by a projection of that point on the $yz$-plane.

The result of the elevation calibration function[2] is a recording of the goniometer its (raw) sensory data, as described in subsection 3.1.2. The $y$- and $z$-data describes the object movement required to return the object to the reference position, at the current elevation position. For the spherical calibration object, this means the movement data describes the position of the OC with respect to the RC, as explained in subsection 2.3.2. In theory, the results are a snipped of two sinusoidal function, as displayed in Figure 3.6.

Figure 4.3a shows one of the results, produced by the elevation calibration function. Both lines show sinusoidal behaviour. Notice that both the $y$- and $z$-data is shifted vertically (with

---

[2] The elevation calibration function is called `CalibrationELaxis_JJ` and can be found at [1].

respect to Figure 3.6), because the coordinates are set to zero at the initial elevation position of zero degrees.

Upon closer inspection of the results in Figure 4.3a, it can be observed that the elevation offset position of the object, $P_0$, doesn't lay on the $z$-axis. The $z$-graph isn't symmetrical around the initial elevation angle of zero degrees, as is expected for an elevation offset of ±90°. This contradicts with our initial expectations, because the spherical calibration object is centred on the azimuth axis.

Based on the results presented in Figure 4.3a, it is clear that the theoretical framework, based on the goniometer coordinate system (Figure 2.10a), isn't totally accurate. Experimentally it has been determined that the main source of error for this inaccuracy in the goniometer setup, is the absence of an intersection between the two rotation axis (Figure 2.12). The *rotation axes alignment method*, found in section 3.2, is developed to reduce the distance between the two rotational axis. The results of this method are presented the next section, section 4.3.

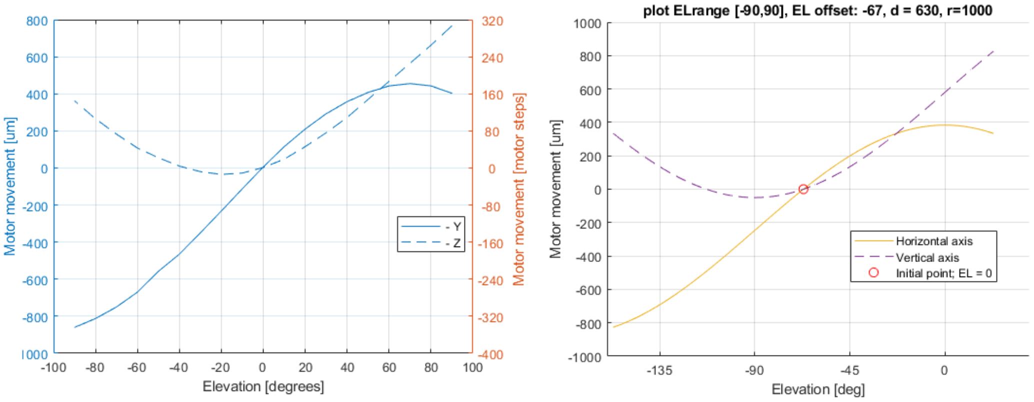

(a) (b)

Figure 4.3: **(a)** Results obtained after running the calibration function of the elevation axis. **(b)** Approximation of the measurement data, Figure 4.3a.

To complete the elevation calibration procedure, the object offset position should to be determined and corrected. For illustrative purposes, we assume that the results found in Figure 4.3a are accurate and can be described by Equation 2.16.

From the initial measurement results (Figure 4.3a), the object position could be estimated. It might however, be difficult to quickly and accurately estimate the elevation offset position, since the elevation range is limited (subsection 2.3.1), and thus only part of the sinusoidal waves is available. However, because we have a mathematical description of the object position, (2.16), we can also try to determine the object position by matching the simulated results to the measured results.

Using an experimental helper function[3], the offset position of the spherical calibration object is simulated. The input parameters of the offset position in the $yz$-plane, are set using polar coordinates $(d, \varphi_0)$. The benefit of this, is that it is easier to match the results of the elevation calibration function, because the position and amplitude is controlled separately. The elevation offset $\varphi_0$ shifts the sinusoidal functions in the graph while $d$ only controls the amplitude.

---

[3] The experimental helper function to simulate the elevation offset position for a spherical object is called `Visualization_RC_errorv4` and can be found at [1].

Figure 4.3b shows the results for an estimated elevation offset position[4] of $(630\,\mu\text{m}, -67°)$ for a spherical object with a radius of $1000\,\mu$m. The results are plotted for a elevation range, equal to that of the measurement data, centred around the elevation offset position. The initial sample point, $P(\mathbf{0})$, is indicated in the simulated results by a red circle and is mainly used for verification purposes.

The simulated results, do appear to (approximately) match the measurement data (Figure 4.3). The locations of the graphs look similar and also the amplitude matches approximately. Using the estimated offset position, we can (manually) adjust the object position. It is recommended to limit the position adjustment to a single axis[5] and redo the elevation calibration again to verify the results.

## 4.3 Goniometer Calibration

In the previous section, it is discovered that the theoretical coordinate system of the goniometer Figure 2.10a, does not accurately represent the five axes of the real goniometer, Figure 2.2. The main difference between the real and theoretical system, accounting for the largest error during a geometry scan, is the distance between the two rotation axes of the goniometer (Figure 2.12). Using a combination of the developed azimuth and elevation calibration methods, a new method is developed to reduce the measured error.

In this section, first, an introductory summery about the goniometer calibration method is given, to give the reader some additional insight into the method. Thereafter, the (final) results of the method are presented and analysed.

Calibration of the goniometer is performed by using the azimuth and elevation calibration methods, as shown in Figure 3.5. By assuming the object is perfectly centred on the azimuth axis and determining the offset position in the $yz$-plane, the distance between the two rotation axes, $y_m$ (see Figure 2.12), is found. To correct the misalignment between the two rotation axes, a number of (potentially tedious) calibration steps has to be done. To get the alignment error as small as possible, micrometer precision is required. This requires accurate measurement, and taking the right choices when choosing which axes to adjust. In the following sections a walkthrough of the process is described.

The first decision symbol in the flow diagram of the goniometer rotation axes alignment method, GRAAM for short (Figure 3.5), asks if the elevation offset (approximately) matches the value for any of the four symmetry points Figure 3.6. This decision is introduced to act on the largest part of the misalignment *vector*. I.e. when the elevation offset angle, $\varphi_0$, is for example, ten degrees, most of the misalignment error is contributed by a misalignment along the $y$-axis. The decision, to act on a specific axis is based on the fact that if the elevation angle is near a symmetry point (0, 90, 180 or 270 degree), the accuracy of the offset position along the other axis is most inaccurate. I.e. it changes relatively much for small changes in the elevation offset value.

In the flow diagram (Figure 3.5), it is also indicated that the $y$-axis offset can be simulated, by adjusting the object position along the $y$-axis. Adjusting the position of the calibration object on the calibration stage (Figure 2.4b), is faster and easier than adjusting the position of the rotation

---

[4] The elevation offset position is also reported in Cartesian coordinates by the experimental helper function `Visualization_RC_errorv4`. For the offset location discussed in section 4.2, $(630\,\mu\text{m}, -67°)$ is equal to about $(246, -580)\mu$m, based on the RCS Figure 2.10b, or $(246, 580)\mu$m, based on the GCS Figure 2.10a.

[5] When using the calibration stage (Figure 2.4b), the horizontal position of the object is changed slightly when adjusting the height of the spherical calibration object.

axes. Temporarily simulating the position of the azimuth axis is a safe bet when partially testing the method or reducing the $y$-axis offset before adjusting the $z$-axis offset. Also note that the adjustment of the $y$-axis offset of the rotation axes can also have a very negative outcome when not performed with micrometre-level precision, since an adjustment of multiple times the current misalignment error is easily made. A number of steps are suggested when adjusting the $y$-axis, these are described in subsection A.2.2.

### 4.3.1 Final Results

In this section, the elevation calibration graphs obtained after the final adjustment of the $y$-axis alignment are shown. Additionally, some points of congestion are described to inform the current and future team of the GRACE project.

The calibration results of the final goniometer calibration results are displayed in Figure 4.4a. The azimuth calibration results are displayed in Figure 4.5, to provide all the available position information. From the elevation calibration results shown in Figure 4.4a, it can immediately be seen that the measurement results do not align with the expectation of two sinusoidal graphs, as seen in Figure 3.6. The data measured from the $z$-axis looks to be skewed, since the azimuth calibration results show the spherical calibration object is well centred on the azimuth axis. Also the elevation calibration measurements that preceded the final elevation measurement, indicated some unexpected behaviour for the $z$-axis when the amplitude of the elevation offset position decreased.

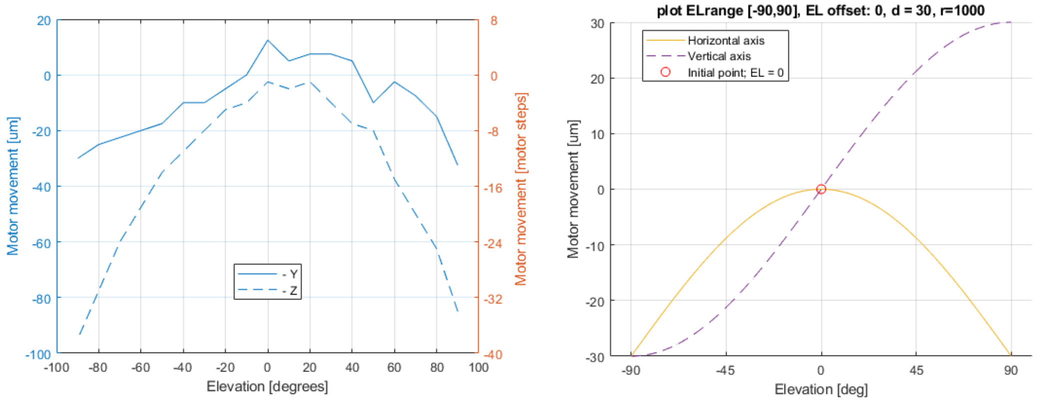

(a) (b)

Figure 4.4: **(a)** Final goniometer calibration results. **(b)** Curve fitting approximation of the data in Figure 4.4a. The fitment is mainly based on the $y$-graph.

The elevation calibration measurement results shown in Figure 4.6a also shows a similar scenario. However, these measurements were created during a *simulated* $y$-axis offset, i.e. the object position was changed instead of the rotation axis alignment.

By comparing Figure 4.6b to Figure 4.6a, it can be seen that the expectations of the $y$-axis match the estimated elevation offset position results quite well. However, instead of a convex parabola, the $z$-axis describes a linear path by coincidence. The measurement results show that the object height for this measurement is almost the same everywhere, while its position on the

$y$-axis changes about 150 $\mu$m between $\varphi = -90°$ and $\varphi = 90°$.

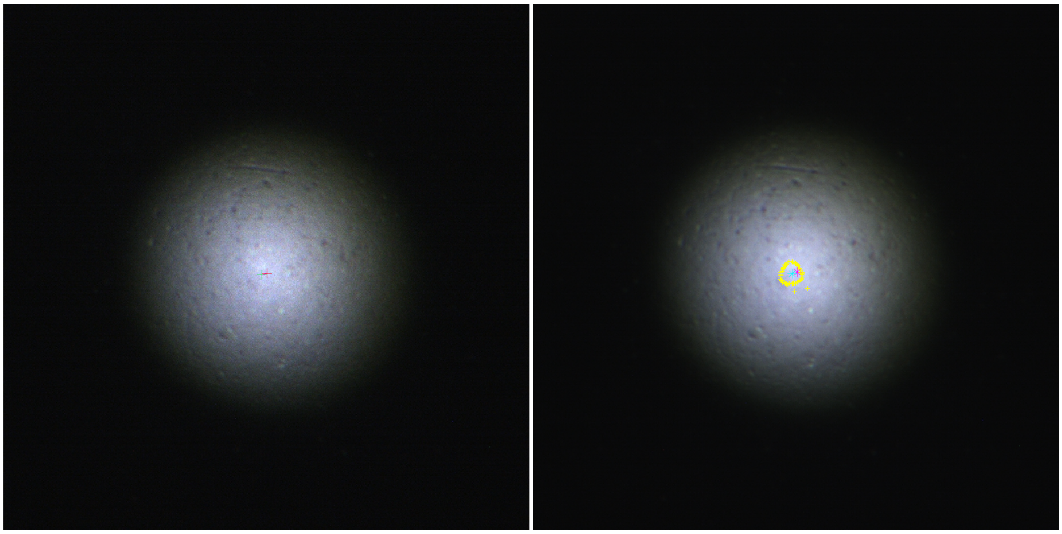

Figure 4.5: Azimuth calibration result, preceding the final elevation calibration shown in Figure 4.4a.

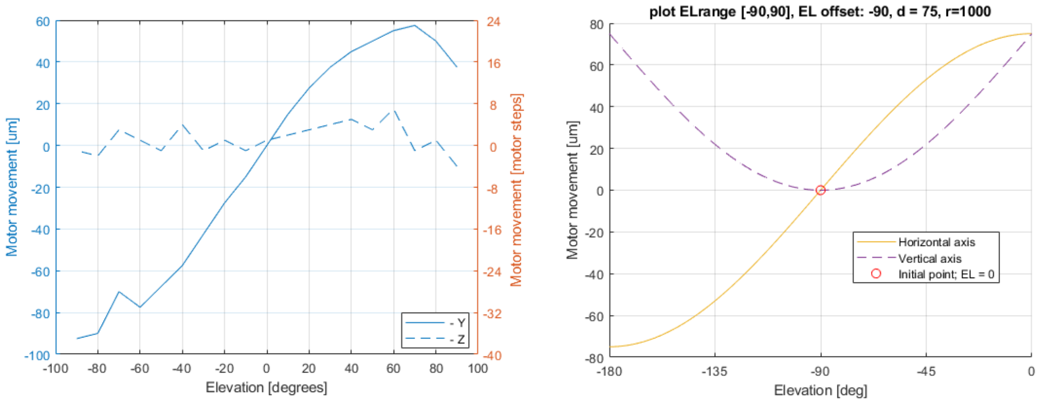

(a) (b)

Figure 4.6: **(a)** Goniometer calibration results for a *simulated* $y$-axis offset. **(b)** Curve fitting approximation of the data in Figure 4.4a. The fitment is mainly based on the $y$-graph.

Based on the results presented in Figure 4.6 and Figure 4.4, along other intermediate elevation calibration results and the results presented in section 4.4, we strongly believe that: the $z$-axis results measured have a gravity induced offset. A gravity induced offset is hypothesised, because the $z$-axis movement data values are lower than expected, past a certain elevation threshold. As indicated by Figure 4.6, the induced offset increases for larger elevation angles.

Additional evidence for the gravity hypothesis is brought by the hemispherical 3D visualisations of the next section, which also show this behaviour, very consistently. No evidence against the gravity hypothesis has been found.

It is hypothesised that the gravity induced offset might be caused by mechanical play in one or potentially multiple of the mechanical joints between the calibration object and optical table. However, no conclusions about the gravity hypothesis are made, because it is not scientifically investigated.

To conclude upon the goniometer calibration results. Based on the estimated object position seen in Figure 4.4 and the azimuth calibration result shown in Figure 4.5, the results seem to show that the alignment error between the rotation axes of the goniometer is about 20 to 50 micrometer. This is quite an improvement from the initially estimated alignment error of about $300\,\mu$m (subsection A.3.1). At the end of the next section, we will also evaluate the alignment error using a more statistical approach.

## 4.4 Object Scan Results

After the goniometer calibration, four scans of the spherical calibration object are made. The first scan is centred on the azimuth and elevation axis, using the prescribed methods. For the second mapping, the centre of the calibration object is placed at an offset along the $y$-axis. In the third scan, the centre is placed at an additional $x$-offset with respect to the second scan. And finally, in the fourth and last scan, the object is offset along all three axes. The parameters of the different scans are summarised in Table 4.1 and Table 4.2.

In the four following subsections, the data for each scan is analysed and described. The mapping of the offset calibration object, results in a morphed geometry representation of the object. The mathematically based post-processing correction method called SEER, is used to demorph the geometrical data back to the original object shape. The goal of this section is to show that an object placed at any known offset location, can still be accurately imaged by the GRACE system.

The first section provides a baseline of the results that can be expected. In each of the sections that follow, the obtained measurement results, present themselves in a more and more altered state. From one perspective, the results may look-alike, however from another perspective they are certainly different.

Table 4.1: Object scan result (OSR) reference name, offset position $P_0$ in micrometres and motor step units, appendix reference for additional images and the data folder ID of the respective object mappings. Note the offset is defined with respect to the origin, according to the RCS, as depicted in Figure 2.10b.

| **OSR referenced as** | **Offset (x,y,z)** [$\mu$m] | **Offset** (x,y,z) **[M]** | **More Figures** | **Data folder ID** |
|---|---|---|---|---|
| **First** | [0,0,0] | [0,0,0] | subsection A.4.1 | 20220107 |
| **Second** | [0,-600,0] | [0,-240,0] | subsection A.4.2 | 20220110 |
| **Third** | [-450,-600,0] | [-180,-240,0] | subsection A.4.3 | 20220114 |
| **Fourth** | [-600,-450,-755] | [-240,-180,-302] | subsection A.4.4 | 20220413 |

Table 4.2: Scan parameters for the different calibration object mappings.

| **Referenced as** | **AZ Step** [°] | **AZ range** [°] | **#AZ steps** | **EL Step** [°] | **EL range** [°] | **#EL steps** | **#Samples** |
|---|---|---|---|---|---|---|---|
| **First** | 30 | 0:Azstep:360 | 13 | 10 | 0:Elstep:90 | 10 | 130 |
| **Second** | 10 | 0:Azstep:360 | 37 | 10 | 0:Elstep:90 | 10 | 370 |
| **Third** | 10 | 0:Azstep:360 | 37 | 5 | 0:Elstep:90 | 19 | 703 |
| **Fourth** | 10 | 0:Azstep:360 | 37 | 3 | 0:Elstep:90 | 31 | 1147 |

Something that should be noted about the data, is the definition of the initial sample position or initial reference point. Two interpretations for the initial reference position are used. Both of these assume the position of the first sample point along the $x$- and $y$-axis is zero. The difference between the two interpretations of the reference position, is the defined initial height. It is either chosen to take the surface height of the object as zero, or it is chosen to set the surface height equal to the known or estimated distance from the defined OC to the surface.

For the spherical calibration object, the distance is equal to the radius. For fly eyes, the distance is defined from the surface of the eye, also known as the cornea pseudopupil (CPP), down to the height were the imaged deep pseudopupil (DPP) has the smallest diameter [24].

Both interpretations have their pros and cons. In the data-processing of this project, it is chosen to convert all the data to the zero surface height interpretation. The zero surface height is also the method reported in recent literature [24]. Two of the four object scan results haven been recorded using the OC position as the defined zero location. Additionally some scans do have a small initial none-zero position saved as the first position. The raw sensory data is adjusted to comply to the initial *zero condition*[6].

It should be noted that, for all recorded data displayed in this section, some data conversion steps are used which are not explicitly stated. The initial sample position is defined zero and the data is converted from the (raw) sensory data to the *position* data format, see Table 2.3. In this section, the data is seen in the $x$-, $y$- and $z$-graphs is referenced to the initial zero location. The histograms and the geometry figures presented are referenced to the OC. This is achieved by adding the known object height (sphere radius) to the measured $z$-axis position data, which describes the measured height difference with respect to the initial object height. More details about the data processing and plotting can be found in the SEER scrips and data visualisation MATLABlive script[7].

### 4.4.1 No Offset Mapping

The mapping of any object is made using the general scan method as described in subsection 2.3.1. The obtained results are recorded in a table where each column stores a parameter. The table is (by default) sorted in ascending order for (first) the elevation parameters and (then) the azimuth parameters, i.e. the order is equal to the order in which the sample points are scanned. Each sample point represents a selected orientation of the goniometer, for which the motor positions and an image are recorded after auto-focusing and auto-centring.

The mapping data of the calibration object is visualised in a few different ways: 1a. The $x$-, $y$- and $z$-data are plotted in separate graphs with the expected object centre *path*. 1b. similar to 1a, but the data is sorted in the ascending order for the elevation column instead of the azimuth column. 2. The $x$-, $y$- and $z$-data is plotted in a histogram. 3. A 3D mesh plot is made using the data of all five goniometer axes[8]. Each visualisation method approaches the data from another point of view, which helps to quickly asses and understand the obtained geometrical data. In Figure 4.7, the course of the data for the different sample points is visualised. For the $x$- and the $y$-data, the amplitude of the raw measurement data is stays within a range of 40 micrometer from the expected results. This is very reasonable considering the non-zero but small calibration error between the two rotational axes (section 4.3), and the not perfectly centred calibration

---

[6] In the SEER scripts (e.g. `SEER_JJ_scratchv4_data7jan.m`, [1]), this can be found in the script section called ”Adjust raw sensory data”.

[7] See `VisualizeBallData_improved_method_JJ.mlx` and for example, `SEER_JJ_scratchv4_data7jan.m`.

[8] The script used to create the 3D plots is called `VisualizeBallData_improved_method_JJ.mlx` and can be found at [1].

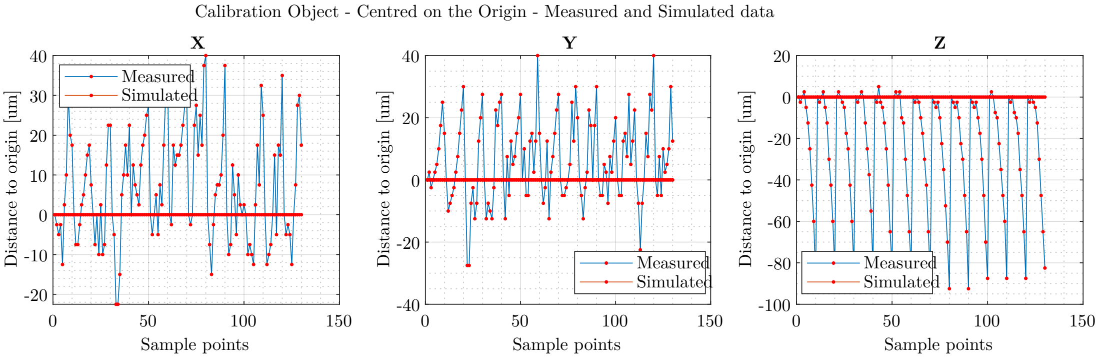

Figure 4.7: Measured $x$-, $y$- and $z$-data and the simulated $x$-, $y$- and $z$-data for the object centre.

object (estimated offset is about $10\,\mu\text{m}^{9}$). Additionally there are also other variables like the repeatability and accuracy of the auto-focus (AF) and auto-centre (AC) functions[10] and the non-orthogonality of the $z$-axis of the goniometer setup.

To investigate upon the expected position offset induced sinusoidal behaviour in the data, which cannot easily be seen in the current display of the data, the moving mean of the data is calculated. In Figure 4.8 the data can be seen with a moving mean. The moving mean in the $x$-data graph shows some sinusoidal like behaviour, which might be correlated to the azimuth axes offset. Additionally, it can be observed that the local minima in the $z$-graph also show a weak sinusoidal behaviour with a small amplitude. According to the sample position description formula, (2.14), which are implemented in the SEER scripts[11], an object offset along the $x$-axis results in an offset similar to the local minima in the $z$-graph and the trend seen in the $x$-graph.

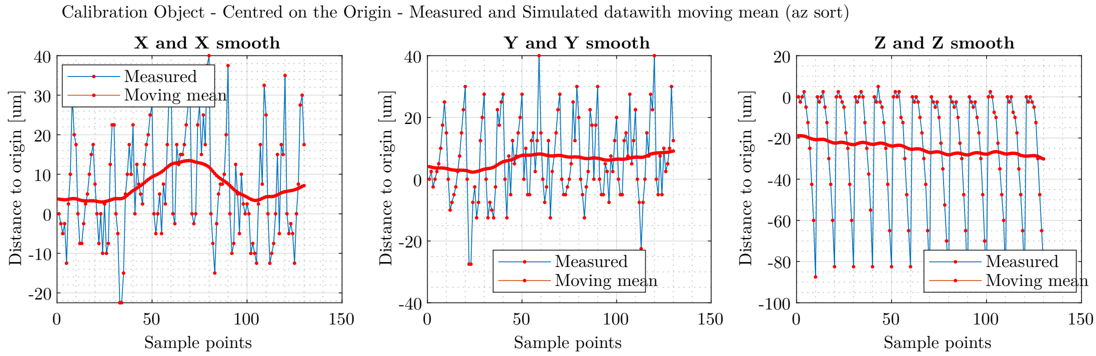

Figure 4.8: Measured $x$-, $y$- and $z$-data and the moving mean of the data. Data samples sorted in the ascending order for the azimuth data.

The elevation offset position can (potentially) be easier observed, by sorting the data for the

---

[9] Azimuth calibration of this scan, preceding the object scanning, is presented in Figure 4.5. The distance between the azimuth axis and OC is estimated to be about $10\,\mu$m, see section 4.1.

[10] In this project the AF and AC functions were redesigned to increase accuracy and repeatability at the cost of additional time. These functions are called `AFv2_JJ.m` and `AC_sphere.m` and can be found at [1].

[11] For example, see the section called *"Position Estimation Calculation"* in the script called `SEER_JJ_scratchv4_data7jan.m`, [1].

elevation data-column instead of the azimuth data-column. The measurement data plotted in Figure 4.9, is ordered for the elevation values. I.e. all sample points of a single elevation values are plotted sequentially. In the $x$- and $y$-data graph, the moving mean has a clear upward trend. The $z$-graph on the other hand, has a clear downward trend. Both trends seem to be correlated to the elevation, however as could also already be seen in the first $z$-graph, in Figure 4.7, the trend in the $z$-graph is the most clear and has the least noise.

However, none of these trends can be fully explained by a single offset location, assuming an ideal goniometer setup, for which (2.14) are valid. The large trend in the $z$-graph could be explained by an offset along the $z$-axis, however the $y$-data doesn't (fully) follow this trend, when simulating the offset position. The same is true for the trends of the other graphs. Based on the experience with the setup, it is hypothesised that the trend of the $z$-data is potentially caused by gravitational forces, as also earlier indicated. The trend in the $x$- and $y$-data might be explained by the misalignment of the azimuth axis and the optical axes, due to the $z$-axis not being orthogonal to the optical table. There is however still room for other interpretations of the results. None of these hypothesises were evaluated during this project.

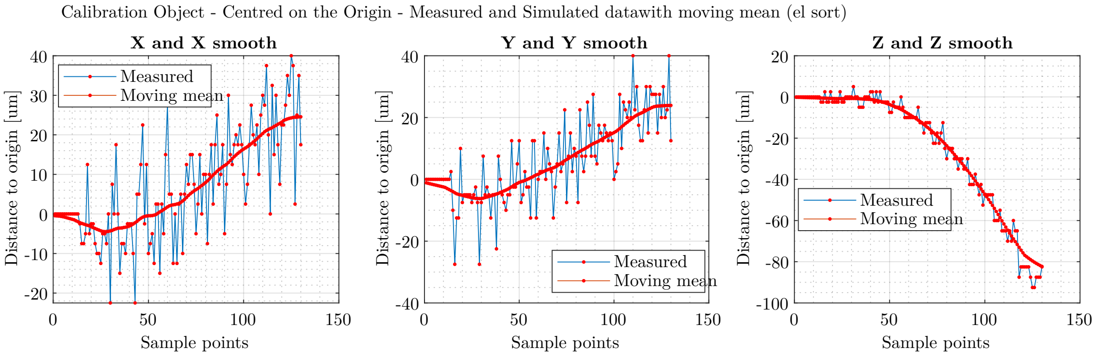

Figure 4.9: Measured $x$-, $y$- and $z$-data and the moving mean of the data. Data samples sorted in the ascending order for the elevation data.

To gain additional insight into the data, the distribution of the data is examined. In Figure 4.10, the histograms of the measured $x$-, $y$- and $z$ position data can be seen. Note that the $z$-data has been modified by adding the radius of the spherical calibration object. This way, the histogram describes the (measured) height distribution of the object. The initial sample position is reported multiple times in the histograms, because it is sampled multiple times (subsection 2.3.1). This does explain the high bin count at zero and at the radius value.

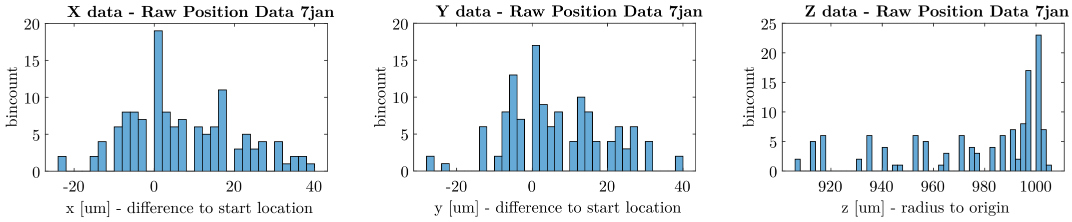

Figure 4.10: Histograms of the measured $x$-, $y$- and $z$-data. The bin width is 2.

As seen in Figure 4.10, the $x$- and $y$-data is normally distributed, but marginally skewed to

the left. The $z$-data on the other hand has a straight tail and is heavily skewed, indicating that the measured radius of the calibration object isn't normally distributed. This also hints to an elevation dependent offset, because it is expected that the $z$-data is constant, based on the spherical calibration object.
The plots of the 3D visualisation confirms the repeating shark-fin pattern of the $z$-data, seen in Figure 4.7. When viewing the measured object data along the $x$-axis ($yz$-plot Figure 4.11) and along the $y$-axis ($xz$-plot Figure 4.12), it can be seen that the hemispherical mesh plot is somewhat tugged in around the edges. The grey translucent hemisphere illustrates the expected geometry, i.e. it is a hemisphere with a radius of 1000 $\mu$m.

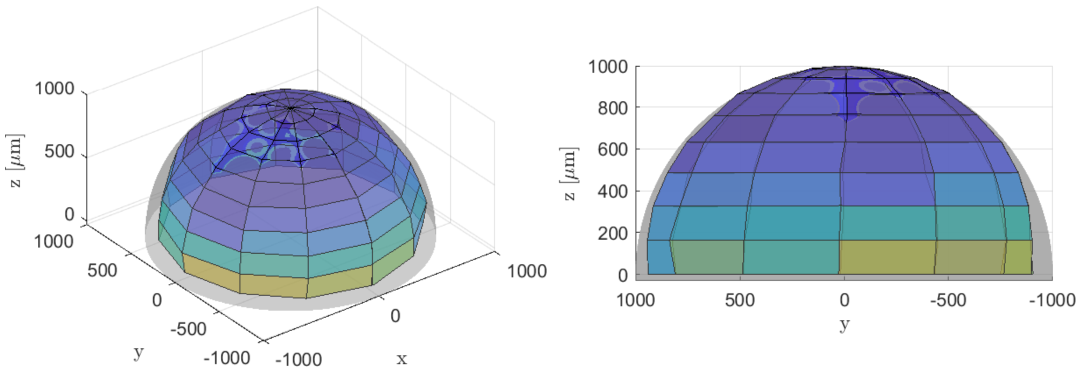

(a) $xyz$-plot (b) $yz$-plot

Figure 4.11: 3D mesh plot of the measured goniometer data. Azimuth and elevation viewing angles are [-37.5 30] and [-90 0] for the left and right plots, respectively. The height values are also use to colour the mesh.

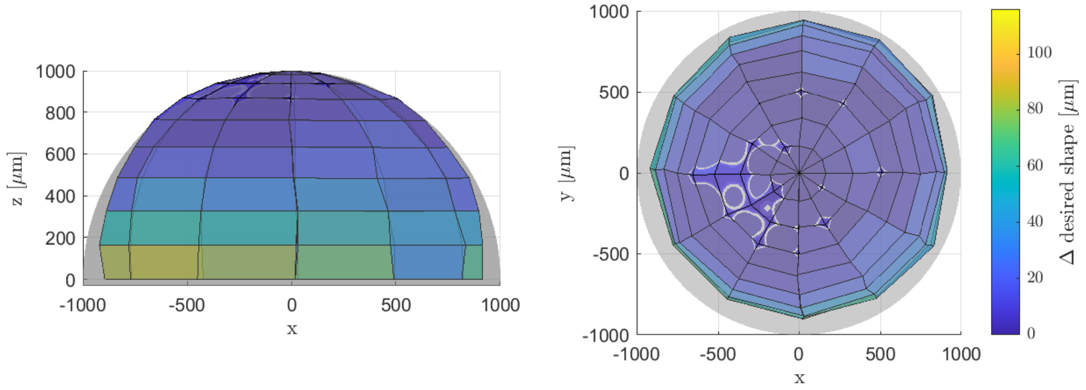

(a) $xz$-plot (b) $xy$-plot

Figure 4.12: 3D mesh plot of the measured goniometer data. Azimuth and elevation viewing angles are [0 0] and [0 90] for the left and right plots, respectively. The height values are also use to colour the mesh.

To conclude this first section, the results of the reference scan look very promising. The hemispherical scan of the spherical calibration object capture the shape of the object accurately and consistently. To increase the accuracy even further, suggestions are made in the discussion, chapter 5. Statistics about the radii of the 3D plot can be found in Table 4.3, subsection 4.4.4.

### 4.4.2 Y-offset Mapping & Reconstruction

The well calibrated position of the calibration object is changed to have an offset of 600 $\mu$m in the negative $y$-axis direction. The offset is thirty percent of the diameter of the spherical calibration object examined.
The $x$-, $y$- and $z$-results of the mapping of the off-centre sphere are plotted in Figure 4.13. Compared to the noise like signal from the reference measurement (Figure 4.7), the sinusoidal behaviour, described by (2.14), is immediately apparent for this particular order of the sample points. Notice that the data is shifted such that the initial sample position matches the $y$-axis offset position. The data is shifted to ease the data analysis.

The measured and simulated results are hard to distinguish at this level of overview. For a better comparison between the measured and simulated data, a selection of sample points is visualised in Figure 4.14. In Figure 4.14 it can be seen that the overall amplitude differences between the measured and estimated data is comparable to the reference object mapping. The error range is for each axis is about equal, but this time it can be observed that there is a clearer trend in the difference between the simulated and estimated position data of the sample point.

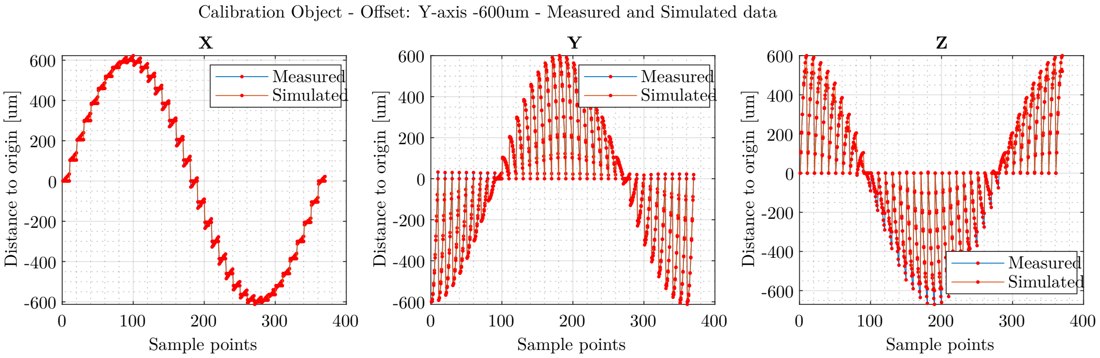

Figure 4.13: Measured $x$-, $y$- and $z$-data and the simulated $x$-, $y$- and $z$-data for the OC.

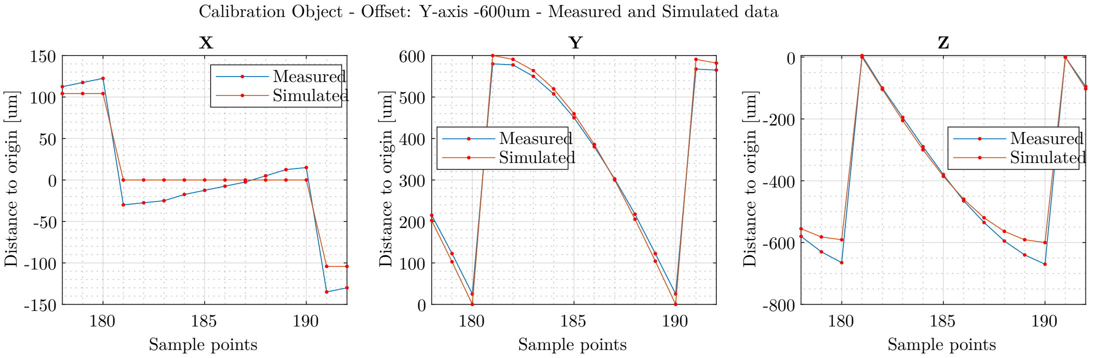

Figure 4.14: Measured $x$-, $y$- and $z$-data and the simulated $x$-, $y$- and $z$-data for the OC.

The 3D visualisation of the data can be seen in Figure 4.15 and 4.16. These plots look nothing like the ideal grey translucent hemisphere, which is centred on the origin. The face colour depicted in the images indicates the distance between the measured and expected positions of the sample points. The colorbar indicator present in Figure 4.16 is valid for all other views of the geometrical data.

Notice that the there is an intersection of the surface at a height of approximately 1000 $\mu$m above the $x$-axis. The geometrical shape makes a figure eight when seen from above, except for the top part which creates a sort of umbrella. Apart from the minimal deviations, this figure is mathematically described by (2.14).

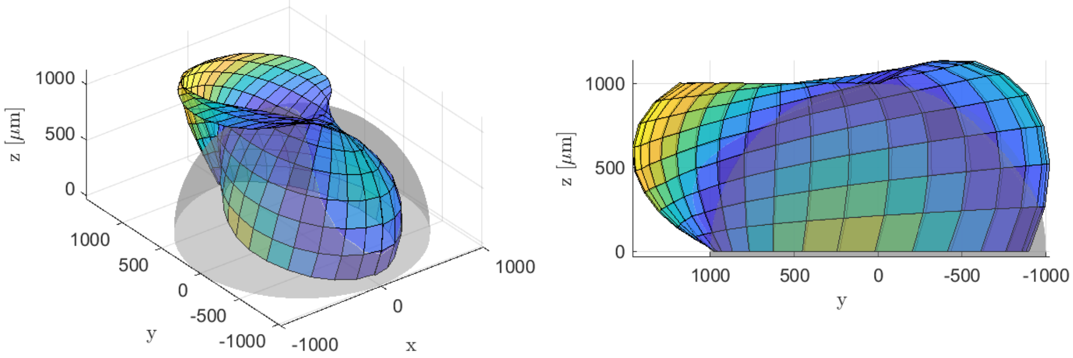

(a) $xyz$-plot (b) $yz$-plot

Figure 4.15: 3D mesh plot of the measured goniometer data. Azimuth and elevation viewing angles are [-37.5 30] and [-90 0] for the left and right plots, respectively. The height values are also use to colour the mesh.

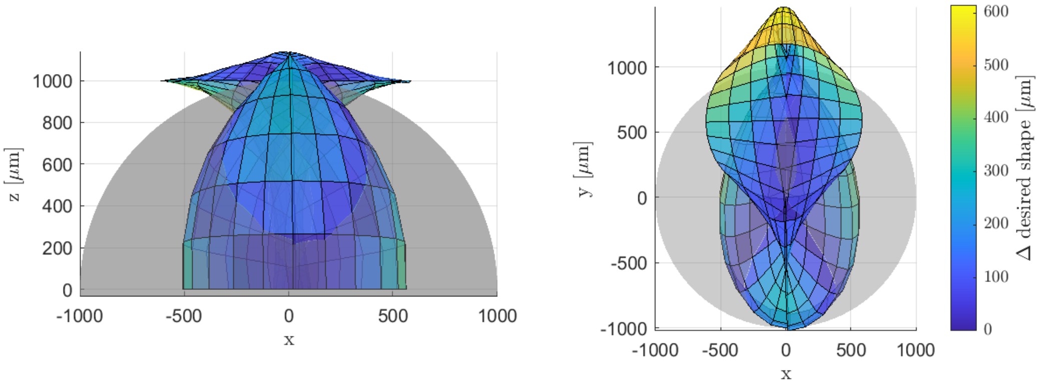

(a) $xz$-plot (b) $xy$-plot

Figure 4.16: 3D mesh plot of the measured goniometer data. Azimuth and elevation viewing angles are [0 0] and [0 90] for the left and right plots, respectively. The height values are also use to colour the mesh.

### Spherical Error Estimation & Reconstruction

A transformation to the data is applied by the SEER post-processing, the spherical error estimation and reconstruction process (section 3.3). The histograms of the adjusted data (Figure 4.17) looks quite similar to the histograms of the first well aligned scan results (Figure 4.10). Notice that the number of sample points have been increased.

The results of the $x$-axis and $y$-axis is less centred around zero, compared to the well aligned results. but the difference on a scale of the 1000 micrometre radius is relatively small. The height data is consistently lower than the expected 1000 micrometre radius of the calibration object, which we also saw in the reference results.

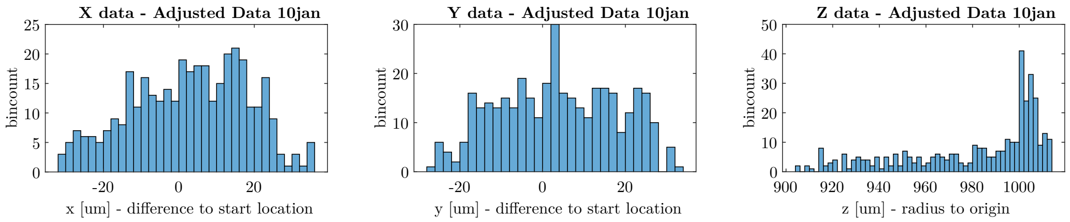

Figure 4.17: Histograms of the measured $x$-, $y$- and $z$-data. The bin width is 2.

The 3D visualisation of the adjusted data, seen in Figure 4.18 and 4.19, reveals a hemispherical shape. This shape largely represents the actual shape of the calibration object and is also very similar to the reference results from subsection 4.4.1. Some statistical data about the radius for the raw and adjusted (reconstructed) data of this second sphere mapping can be found in Table 4.3. From this table, it can be seen that the standard deviation (std) of the radii data is $33\,\mu$m which is similar to the std of the first mapping.

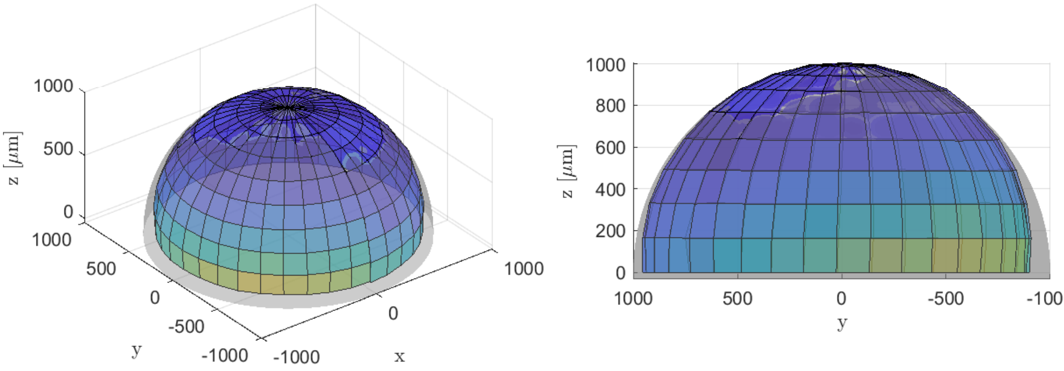

(a) $xyz$-plot

(b) $yz$-plot

Figure 4.18: 3D mesh plot of the measured goniometer data. Azimuth and elevation viewing angles are [-37.5 30] and [-90 0] for the left and right plots, respectively. The height values are also use to colour the mesh.

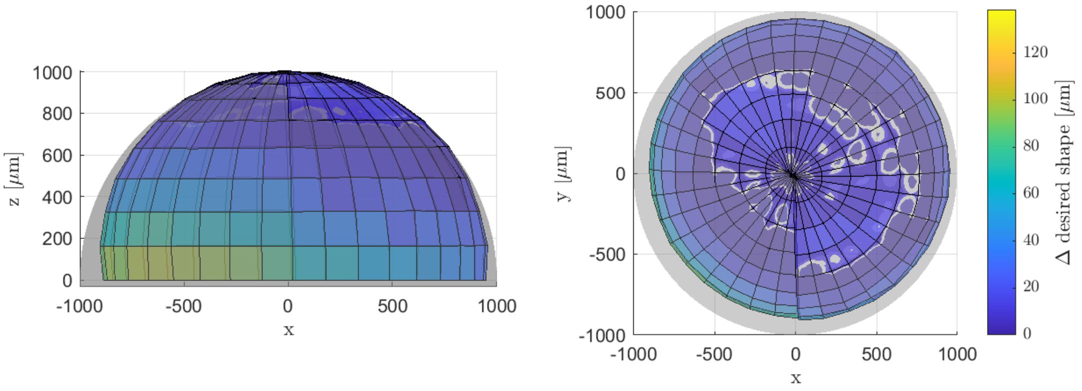

(a) $xz$-plot (b) $xy$-plot

Figure 4.19: 3D mesh plot of the measured goniometer data. Azimuth and elevation viewing angles are [0 0] and [0 90] for the left and right plots, respectively. The height values are also use to colour the mesh.

### 4.4.3 XY-offset Mapping & Reconstruction

The mapping of the results of the third calibration object measurement is similar to that of the second calibration object measurement. The only difference between these mappings is the offset position and the elevation step, as can be seen in Table 4.1 and 4.2. The raw position measurement results of this two axes offset measurement do follow the expectations, as seen in Figure 4.20.

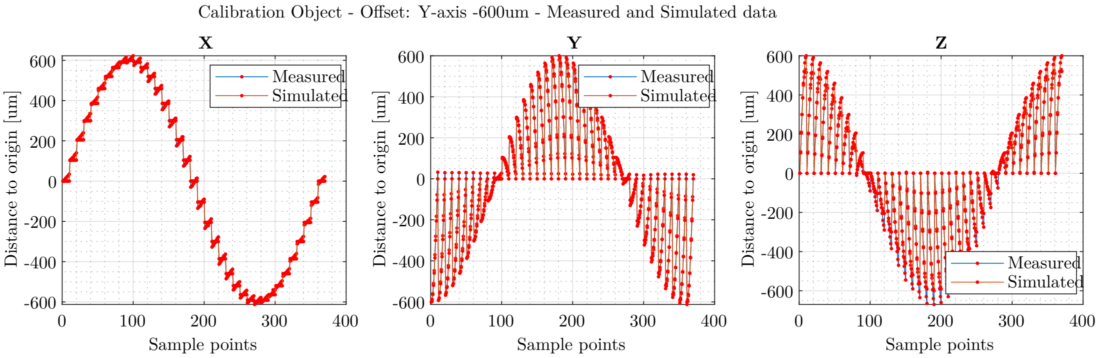

Figure 4.20: Measured $x$-, $y$- and $z$-data and the simulated $x$-, $y$- and $z$-data for the object centre.

Looking ahead to the statistical data of the third mapping, the results are even more consistent than the previous two scans, based on the standard deviation value. A 3D visualisation of the raw and the adjusted data can be seen in Figure 4.21 and 4.22, respectively. The measured geometry is somewhat different shaped, compared to the previous section, but it still has quite some similarities.

To view the geometry from all direction, it is recommend to recreate the plots using the available files. An instruction sheet is provided on Github, in a separate folder [1].

Additional images and details about the data can be found in the appendix, subsection A.4.3.

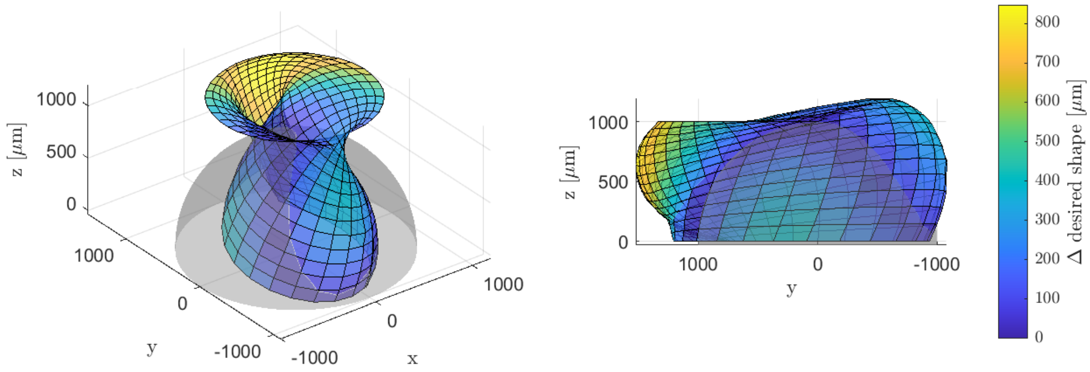

(a) $xyz$-plot (b) $yz$-plot

Figure 4.21: 3D mesh plot of the measured goniometer data. Azimuth and elevation viewing angles are [-37.5 30] and [-90 0] for the left and right plots, respectively. The height values are also used to colour the mesh.

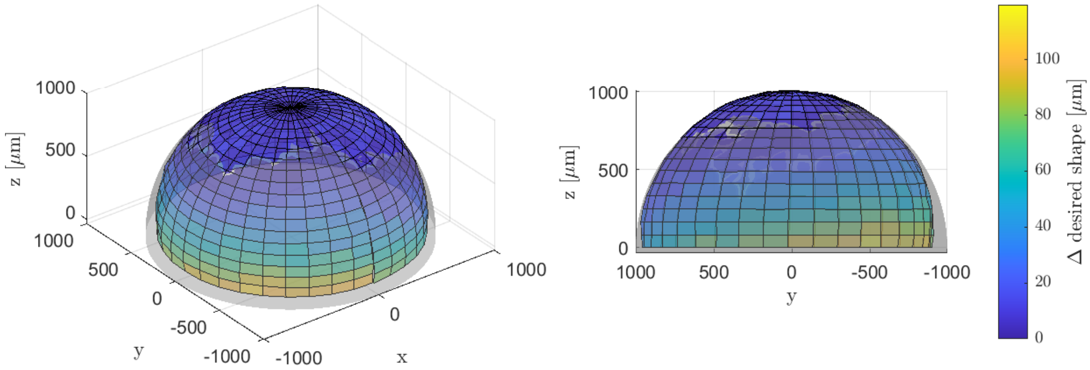

(a) $xyz$-plot (b) $yz$-plot

Figure 4.22: 3D mesh plot of the measured goniometer data. Azimuth and elevation viewing angles are [-37.5 30] and [-90 0] for the left and right plots, respectively. The height values are also use to colour the mesh.

### 4.4.4 XYZ-offset Mapping & Reconstruction

For the last and final mapping, the spherical calibration object is placed at an offset location which does not lay on any plane spawn by two of the Cartesian axes, as is the case for the first three object mappings. The result of this mapping truly tests if the mathematical description of the sample point holds, since it tests all axes relations simultaneously.

In this section, first the appearance of the data is referenced to the formula which describe the sample point, to approach in another way. Thereafter the 3D visualisation of the data is shortly discussed, after which we explore the reconstruction of the original object geometry. Finally a short statistical analysis about the four different object scans is presented.

The measurement results of the $xyz$-offset mapping are presented in Figure 4.23. The raw position measurement results do differ from those presented in subsection 4.4.2 and 4.4.3. The difference in appearance between the measurement results can be explained by the $z_0$ terms of (2.14). In the earlier scans, were only a offset location in the horizontal plane is considered, the overall sinusoidal appearance (for the data ordered in the way the data is obtained) is determined by the $\theta$ terms of (2.14). The $\varphi$ terms are responsible for the short term behaviour of the data, presented by the rapid vertical movement. As a side note, the $x$-data depends only on one rotational axis, thus its appearance won't become more complex. That is, for a spherical scan object at least. So with the addition of the non-zero $z_0$ term, the overall appearance of the $y$- and $z$-data is altered, because it is added to the overall result instead of only being a multiplier, (2.14).

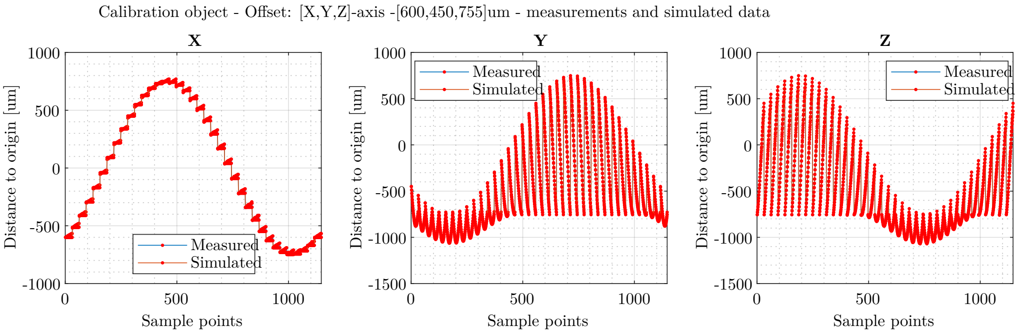

Figure 4.23: Measured $x$-, $y$- and $z$-data and the simulated $x$-, $y$- and $z$-data for the object centre.

The 3D visualisation of the raw positional data is presented in Figure 4.24. It can be observed that the geometry is quite a bit larger than the actual object size, depicted as the grey translucent hemisphere. If we had to describe the figure, after observing it from all sides, then we would say that it looks like a short hollow cylinder which is first pressed from the sides, after which the top part is made more narrow and shifted to the back of the cylinder. Then the top part of the short flattened hollow tapered cylinder is folded in on it self by rotating around an axis parallel the long side of the flattened cylinder, while maintaining its round top shape and not being restricted by its own shape.

To try to reconstruct the actual shape of the calibration object, the SEER script is used once more. Histograms of the resulting data can be seen in Figure 4.25. It can be observed that the $x$- and $y$-data is slightly more spread than we have seen in the previous reconstructions.

In Figure 4.26 it can be seen that this slightly larger spread is present due to the sinusoidal behaviour of the data. Since the behaviour is present in the $x$-graph, it is possible that the actual offset position is somewhat different from the estimated offset position. However, this can only be true if there is a equally sized sinusoidal behaviour in the other graphs, assuming no other more complex behaviour is present. It is true that the errors in the data can be reduced by tuning the offset position. However, without any justification and thorough investigation, this is founded. Still, the quality of the data is comparable to that of the earlier scans.

When the data is sorted for the elevation data, as seen in Figure 4.27, we can observe trends similar to those observed in the reference measurement (Figure 4.9). In the additional images in the appendix, section A.4, it can be seen that this is the case for all object scan result. Based

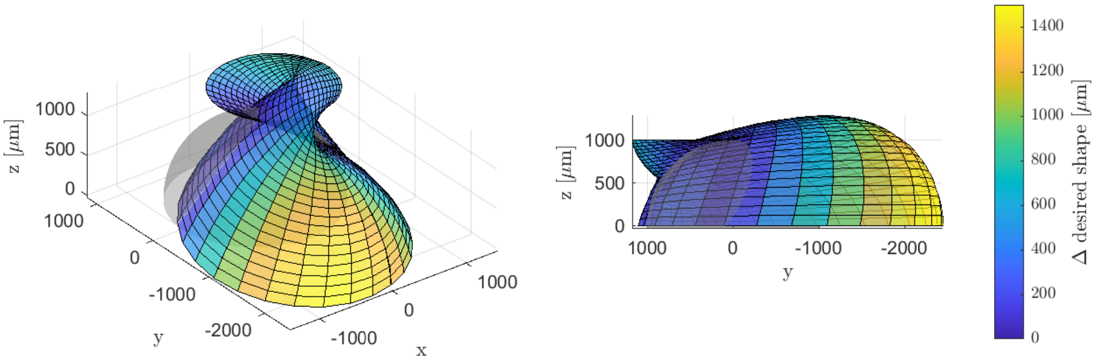

(a) $xz$-plot

(b) $xy$-plot

Figure 4.24: 3D mesh plot of the measured goniometer data. Azimuth and elevation viewing angles are [-37.5 30] and [-90 0] for the left and right plots, respectively. The height values are also use to colour the mesh.

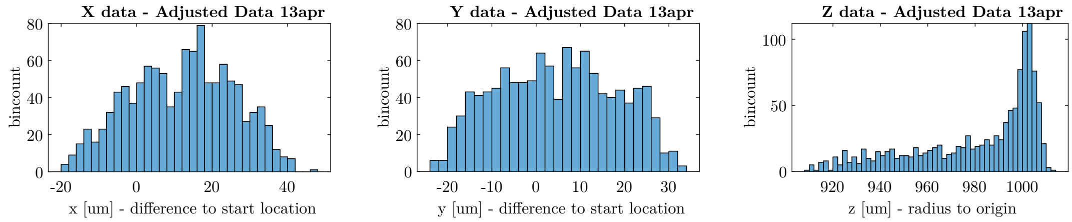

Figure 4.25: Histograms of the measured $x$-, $y$- and $z$-data. The bin width is 2.

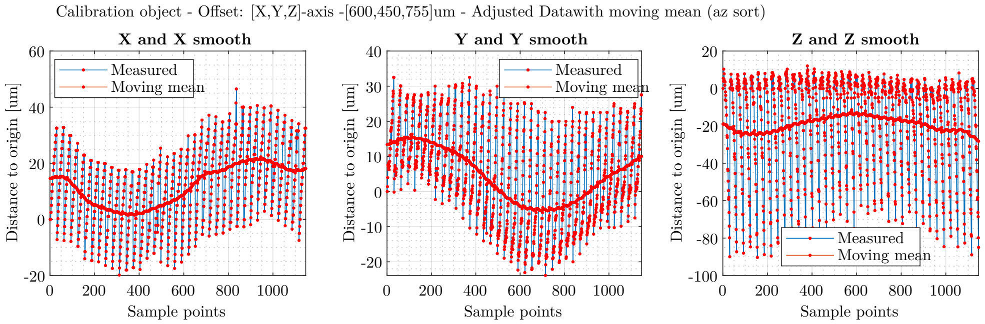

Figure 4.26: Measured $x$-, $y$- and $z$-data and the simulated $x$-, $y$- and $z$-data for the object centre.

on the consistency of the trends, it is highly likely that the trends can be reduced by improving the calibration of the goniometer setup, if possible.

In Figure 4.28 the 3D visualisation of the reconstructed object scan results is seen. The results are as expected from the data analysed earlier. The tugged edge of the hemisphere is still present and the data looks consistent.

Lastly the statistical data of all the four object scan results is presented, Table 4.3. The reported

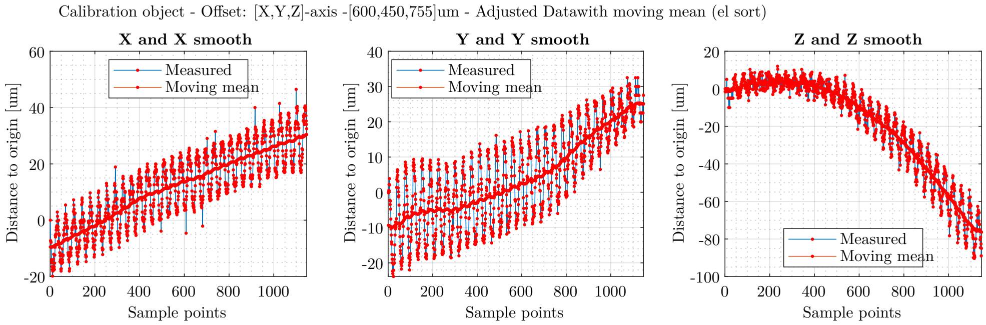

Figure 4.27: Measured $x$-, $y$- and $z$-data and the simulated $x$-, $y$- and $z$-data for the object centre.

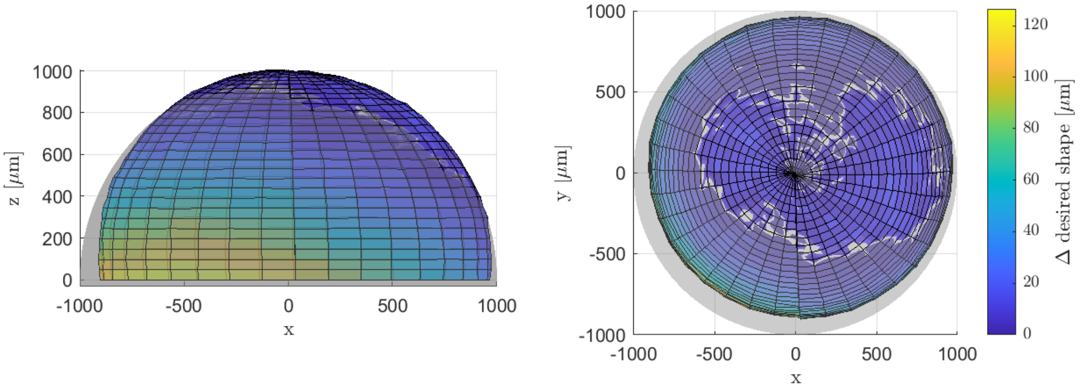

(a) $xz$-plot

(b) $xy$-plot

Figure 4.28: 3D mesh plot of the measured goniometer data. Azimuth and elevation viewing angles are [0 0] and [0 90] for the left and right plots, respectively. The height values are also use to colour the mesh.

minima and maxima are a simple indicator to show the boundaries of the measured geometry. The mean and the median in combination with the first two helps to identify if there are (local) outliers, such as the tugged edge seen in all the hemispherical plots. The mean and median might also be used to identify if the data is skewed, and if it is, the median is the proper statistic to refer to[28]. The standard deviation (std) is an indicator of the dispersion of a dataset relative to its mean. For the scans of the spherical calibration object, the std is an indicator of the robustness and performance of the GRACE setup, since it is a combination of the object position, achieved by the semi-automatic calibration method, and the repeatability of the auto-centre (AC) and auto-focus (AF) functions.

From the results presented in Table 4.3, it can be seen that the results of the reference scan and the reconstructed data are very similar. The difference between the highest point measured between these results is only 2.1 micrometer. Also the std values of these measurements are similar. The difference between the highest and lowest reported std value of these four scans is 3.8 micrometer. Also, the median of the radii measured, of the reference scan and all reconstructed geometry results, do represent the actual morphology of the spherical calibration object very well (diameter is 2000 $\mu$m, nominal diameter $\pm 1.3\,\mu$m). The data shows that the GRACE setup can produce consistent, repeatable and accurate results.

Table 4.3: Statistical data of the radii of the different calibration object mappings. All values are in $\mu$m. The raw data is directly correlated to the results obtained from the goniometer axes. The adjusted data is the raw data processed by the SEER post-processing function [1].

| **Statistics data** | **1st raw** | **2nd raw** | **2nd adjusted** | **3rd raw** | **3rd adjusted** | **4rd raw** | **4rd adjusted** |
|---|---|---|---|---|---|---|---|
| **max** | 1014.0 | 1613.8 | 1014.6 | 1847.0 | 1015.8 | 2498.8 | 1016.1 |
| **min** | 884.4 | 507.6 | 861.9 | 474.2 | 880.4 | 725.9 | 873.8 |
| **mean** | 974.9 | 1113.9 | 979.4 | 1227.1 | 985.6 | 1462.1 | 981.6 |
| **median** | 988.6 | 1107.6 | 993.7 | 1227.4 | 999.0 | 1432.0 | 995.0 |
| **range** | 129.6 | 1106.2 | 152.7 | 1372.8 | 135.4 | 1772.9 | 142.2 |
| **std** | 32.0 | 257.4 | 33.3 | 330.3 | 29.5 | 376.1 | 30.2 |

# Chapter 5

# Discussion & Recommendations

To enable the three-dimensional morphology mapping of an object, a mathematical description of the sample points with respect to a single point is required. A practical complication is matching the reference point of the object with the reference point of the object description.

The results indicate that by using the developed position calibration methods, the position of a spherical object can be matched to a reference position, with an error down to ten micrometer in the horizontal plane and an error of less than fifty micrometer overall. The obtained measurement results demonstrate that the geometry of a well positioned object can be determined accurately. For a well positioned sphere, the overall standard deviation of the measured radius is 32 micrometer. Additionally, it is illustrated that by calibrating the goniometer of the GRACE system, the accuracy of the goniometric results are improved. Furthermore, the object position analysis supports the theory that an object position error, leads to a morphed morphology of the object geometry, which can be described by mathematical equations. Finally, the measurement results suggest that, if the position error is known, the morphology of an object can be recovered from a morphed morphology without compromise.

During the course of the work, there were some unexpected results. Namely, the relation between measured $z$-axis data and the elevation values, expressed as a tugged in edge, visible in the geometry figures presented in the results section. Initially is was thought that this relation (Figure A.17) took place because of an object position misalignment. However, the data of the other axes didn't correlate with the theory of an object misalignment, based on (2.14). It is hypothesised that a possible explanation for the consistent difference between the measured positions and the expected positions is caused by gravity.

The hypothesis is that the consistent difference between the measured positions and the expected positions is originates from a gravity force. This seems likely, because gravity causes lateral forces on (among other things) the measurement object and the three-axis calibration stage to which it is attached, if the stage is oriented non-horizontally. The results are also consistent with 'pushing', the object further and further down. It could also be possible that there is another explanation for this phenomenon. More research towards this is required to come to a conclusion.

Another unexpected result encountered during the project is the microscopic view of the ceramic ball bearings (subsection 2.2.2). The dark spots, lines and other visual markers caused, initially, some confusion, because the surfaces are very smooth, or in technical terms, they have a very low surface roughness. However it turned out that these *image artefacts* were caused by moisture and other debris, which was brought onto the surface of the balls by handling them bare handed. It has been empirically determined that cleaning the calibration object with a tissue if often sufficient.

## Limitations of applicability - rotation axes calibration methods

The developed rotation axes calibration methods are specifically designed for the spherical calibration object, to maximise the achieved accuracy and performance. Because of this initially limited design, the application of the methods is limited outside their intended use.

The first limitation by design, is the requirement of the scan object to be spherical, which is also the thing we want to renounce. This initial limitation is chosen on purpose, because it is required to verify the validity of the designed methods. Or as a variation of related quotes: Without a strong foundation, there is nothing to build on. However, even if objects are not perfectly spherical, the rotation axes calibration methods can still be used to approximately centre the object. The azimuth calibration method actually doesn't have a defined shape limitation, although it is recommended to use a convex shape, concerning the image analysis. The elevation calibration method however, does require the shape to be convex and at least symmetrical along a single cross-section, because this allows for the identification of a symmetry point. Using the symmetry point, the elevation offset orientation can be determined, used to define the object offset position.

Another limitation is of the methods, is the image analysis capabilities, used to evaluate an image and determine the object centre position. The image analysis functions are specifically designed for the spherical calibration object and are not tested on other objects. These parts of the methods could be adjusted or replaced, to enable the use for other objects or specimen, such as the Musca domestica[1].

## Limitations of performance - geometry scanning

For the geometry scanning, performance is expressed in terms of speed, i.e. the time it takes to complete a scan, and in terms of accuracy, i.e. the difference between the intended sample positions and the actual sample positions. Both of these performance metrics, can is some cases be improved without changing the other, however, often there is a trade-off between speed and accuracy.

The accuracy of the obtained geometry is a function of the number of sample points and the accuracy of those sample points. The scan resolution and in turn the number of samples, is controlled by the operator. The accuracy of the sample points, depend on the initial object position, but partially, also on the performance of the auto-centre and auto-focus functions, which contribute to the local variations of the sample positions. These functions however are outside the scope of this thesis.

The speed at which a scan can be completed, depends fundamentally on the number of samples that are taken. Assuming each sample point is treated equally, each sample point of the object has to be centred and focused, to make sure it is referenced to (approximately) the same reference point each time. These reposition actions take time and determine the number of samples scanned per unit of time.

Other notable accuracy dependencies are the axes calibration of the GRACE system and the rigidity of the object mount.

---

[1] A recommendation is to add an additional input option to a general function of the method, to allow for species specific options to be selected. Such parameter would allow for an easy adoption of new species that need specific image analysis settings.

## Limitations of offset position - rotation axes calibration methods

The amplitude of the offset position, that can be handled by the rotation axes calibration methods, is limited, because the object has to stay within the image frame during the data collection process of the two methods. For the azimuth calibration method, this means that the horizontal offset has to be less than (at least) half of the imaged region of interest. The elevation calibration method is different however, because it already uses the AF and AC functions to change the position of the object. The limits in the maximum offset position for the elevation calibration method, depend on the elevation step size configured, as well as on the size of the imaged region. Because the elevation step size can be configured down to one hundredth of a degree, the maximum offset position for the elevation calibration method practically isn't bound by the method itself.

## Validity of assumptions

In this project, some assumptions are made. For the azimuth calibration method, it is assumed that the angular distance between each sample point, used to determine the position of the rotation axis, is equal. The acceleration and deceleration during the execution of the method is compensated. From the data, the distance between each sample point looks similar. However, besides the human verification of the results, there are no automatic mechanisms made, to verify if the distance between samples is indeed the same. During the whole project, no evidence has been found that the distance between the samples varied significantly, that is, there has been no record, which showed the processing time between the capture and analysis of images, using a processing loop, varied significantly. Based on this observation, the method is assumed appropriate.

Some assumptions about the calibration of the goniometer setup are made. For instance, it is assumed the vertical axis and the optical axis are parallel, and it is assumed that for an elevation angle of zero degrees, the azimuth axis is also parallel to the optical axis and vertical axes. It has however been experimentally determined that the vertical axis isn't parallel to the optical axes. Additionally the angle between the vertical axis stage and the optical table, measured in line with the $xz$-plane, deviates from the expected ninety degrees. Unlike other non right angles, this one could not solely be solved by loosening and tightening bolts. This deviation was taken for granted, but does effect the accuracy of the geometry results.

## Future Work

Further research is needed to make the position calibration methods of this project applicable to the intended use of the GRACE system, namely, compound eyes. Points of future work, which are intended to improve the geometry scanning capabilities of the GRACE system are listed below:

- Further development of the developed rotation axes calibration methods of this project, to make them applicable to a wider range of scan objects.

- Object position prediction is something to explore. Either in the sense of extending the sample horizon without the essential need for auto-centering and auto-focussing, or by using interpolation between a coarse mesh of sample points, to more time efficiently re-sample the object at a higher resolution.

- Incorporate the SEER functionality into a dedicated function instead of a single script for each dataset. It is advised to incorporate a system which stores the specific settings used for the processing of each function. For example, a small script placed in each data folder, which calls the SEER function, if used.

- Additional calibration of the goniometer setup is required to improve upon the current accuracy limits of the goniometer. For the calibration of the vertical axis, it is proposed that a small thin sheet of incompressible material is placed at one end, in between the two surfaces of the $x$-axis and the right-angle bracket, on which the vertical axis is mounted. The small addition of material could compensate for the current non-ideal state.
- A repository for the project files that helps developers store, manage, track and control changes to their work. This can be integrated into the MATLAB project, created during this research project.
- Continuous object tracking and position adjustments, would make it possible for the azimuth calibration method to allow any offset position, instead of being limited to the imaged region. For the elevation calibration method, the current object tracking method could be optimised by automatically decreasing the elevation step size if the object moves out of the image frame.
- Copy of a recommendation of [12]: ”...it is strongly recommended to fix the LED controller. Grey filters did work effectively in reducing the intensity whilst keeping the LED shining at max intensity, but are rather inconvenient for the current setup.” To this I would like to add that taking the average of a number of recorded image frames was used to compensate for the fading effect of the LED controller at slightly lower than maximum brightness values, to prevent image saturation in combination with a Grey filter. An additional benefit of this was the reduced noise of the images.
- A motorised object stage for automated object positioning calibration.

Other points of attention for future projects are the development of generalised and widely applicable auto-focus (AF) and auto-centre (AC) functions, which mainly concerns the selection of a proper image analysis function to select a sample point. Similarly, the developed image capture, analysis and processing functions can be catalogued and potentially fused into a generalised function with a number of child functions. And last but not least, it is recommended to take notes on the methods and functions used in the sphere scanning script, used for for creating the geometry data in this project. The MATLAB *dependency analyser*, available in projects, has also been found a valuable asset.

# Chapter 6

# Conclusion

This research aimed to identify which methods are needed to accurately map the geometry of an object scanned using the GRACE system. Based on the analysis of the five axes goniometer, it can be concluded that a calibration method for each of the rotation axes is mandatory. Geometry measurement results show that the developed methods behave as expected.

This research clearly illustrates that it is possible to semi-automatically calibrate the position of a spherical object. Furthermore this research illustrates that it is possible to accurately measure the geometry of a small concave object using goniometer data and a microscope for position feedback.

To better understand the implications of these results, future studies could address paths towards the further development of these methods, enabling geometry scanning for compound eyes. Another possibility is to develop the application of object position forecasting, to significantly increase the throughput of the GRACE system.

Detailed maps of geometrical properties of compound eyes are valuable for the creation of accurate artificial compound eyes used in applications such as medical imaging, industrial engineering, space engineering and vision and navigation systems. This research project has laid the fundamental groundwork to enable geometry scanning of compound eyes by illustrating it is possible for a reference object.

Additionally, the developed mathematical position model could be explored for the application of position estimation to increase the throughput of the GRACE system. A higher throughput could be beneficial for quantitative studies of Arthropods, used by biologists to obtain a better understanding of the evolution of vision.

# Appendix A

# Appendix

## A.1 Hardware Listing

### A.1.1 STANDA & Digital Camera

Table A.1: Main Standa parts listed and the digital camera.

| Description | # | part number | Notable specifications or other |
|---|---|---|---|
| Digital Camera -<br>Point Grey Blackfly | 1 | BFLY-U3-23S6C-C | Color camera, 1/1.2” sensor format, 2.30MP,<br>resolution 1920x1080, max fps: 41, configurable exposure time and more |
| motor controller | 3 | 8SMC4-USB-B9-2 | 2-axis, many parameters configurable using Xilab,<br>closed loop feedback system with the motors |
| motorised linear stage | 3 | 8MT175-50 | Linear range 50 mm, 2.5um per step. Specs note 1/8 step possible. |
| motorised rotary stage | 2 | 8MR191-28 | max rotation speed: 8 turn/min. Resolution 0.6arcmin, wobble 0.5arcmin |
| base plate | 1 | 3UBP175 | LxWxH, 115x90x9.7 mm, weight 0.3 kg |
| Joystick | 3 | 8JXY-03 | Motor speed and acceleration is configured separately (XILab) |
| power supply | 3 | PUP120-17 | 36V, 3.34A, 100W (2 power bricks in use, 1 spare) |

### A.1.2 STANDA Motor Controller Documentation

On the Standa documentation web page [29], the following relevant documentation can be found:

- User Guide
  - PDF [30]
  - HTML [31]
- Programmer Guide
  - PDF [32]
  - HTML [33]
- Software [34]

## A.2 Additionals

### A.2.1 Elevation Calibration Workflow - Object Positioning

This workflow guides the operator through the final manual step of the elevation axis calibration method, subsection 3.1.2. For reference, the results of the elevation calibration function, `CalibrationELaxis_JJ`, are presented in section 4.2 and section 4.3.

An object positioning error for the $y$ and $z$-axis is found by using the elevation calibration function. These positioning errors can be solved individually or consecutively. Note that adjusting the $z$-error of the calibration sphere object holder shown in Figure 2.4b, will likely introduce an error in the horizontal plane. So, it is advised to first resolve the error in the vertical direction and thereafter resolve the position errors in the horizontal plane. It is advised, to first fully read both the $y$-axis and $z$-axis procedures, before proceeding.

An example is provided for the error described in section 4.2:

$$[y_0, z_0] = [-246, 580]\,\mu\text{m}$$

Note that this position error is referenced to the goniometer coordinate system, Figure 2.10a.

To reduce $y_0 = -246\,\mu$m to zero, the calibration object should be moved in the *positive* direction. The steps are provided below:

1. Mark the current position of the object in the live preview window of the digital camera[1].
2. Adjust the goniometer position of the $y$-axis ($246\,\mu$m) by calling the `STANDAMovMot_JJ` or `STANDAGoPosition_JJ` function. Note that the default position input units are (discrete) *motor steps*[2].
3. Adjust the position of the calibration object back to its original position marked in step 1. Note it might be the case that the object has *left* the ROI of the camera. This is not a problem as the object can also physically be seen while it is adjusted.
4. $y$-axis adjustment is finished.

To reduce $z_0 = 580\,\mu$m to zero, the calibration object should be moved in the negative direction in this particular case[3]. The steps for adjusting the the height of the scan object are:

1. (optionally) call `STANDAPositions_JJ` with or without a motor ID input to recall some or all positions of the goniometer as a reference.
2. Adjust the goniometer position of the $z$-axis ($-580\,\mu$m), which is towards the microscope, by calling the `STANDAMovMot_JJ` or `STANDAGoPosition_JJ` function with the appropriate input.
3. Adjust the position of the calibration object back to its original position.
4. (optionally) call `AFv2_JJ`, with appropriate input, to determine if the adjusted height was correct[4]. If the difference between the (new) manually set height and the height found by

---

[1] This can be made by, e.g. dragging the corner of a window to a marker on the object.

[2] The function `STANDAgetMotorIDs` can be called to retrieve the motor identification numbers (motIDs) and precisely `STANDAgetConstants_JJ("micrometersPerStep")` can be called to retrieve the conversion factor between micrometres and motor steps.

[3] Note that the negative direction is with respect to vertical axis of the GCS, which indicates the object has to be moved closer to the microscope or up with respect to the optical table.

[4] Note that the optional input argument ”debugging” provides additional feedback about the auto-focussing. Alternatively, the function `AF_JJ` can also be used instead of `AFv2_JJ`

autofocusing is too large, go back to step 3 and move the object for the difference noted.

5. $z$-axis adjustment is finished.

Practical causes of error are the limited accuracy of the $xyz$-stage and the precision of the determined rotation offset. The elevation calibration can be repeated to potentially achieve better results.

### A.2.2 Goniometer Rotation Axes Alignment Workflow - Y-axis Offset Adjustment

In the flow diagram of the goniometer calibration method, a box is present indicating 'Adjust the Y-axis offset of the rotation axes'. Here some steps are written down which can be used to achieve the $y$-axis offset adjustment. Note that it is also written that the adjustment can be *simulated*. This is done by adjusting the object position (using the object mount). Note however that this means the azimuth calibration should be skipped, because it will revert the $y$-axis adjustment.

To correct the $y$-axis offset between the two rotation axes of the goniometer, $y_m$, it is advised to follow the steps written down below.

1. Move the object to the origin, as indicated in Figure 2.12, using the motorised $y$-axis of the goniometer. I.e. do a (STANDA) motor-call which moves the object a distance of $y_m$[5].
2. Mark the position of the object in the camera live-view of the GRACE system, for example by placing the mouse or the corner of a window at a clearly distinguishable point of the sphere. It is recommended to take a screenshot as well.
3. Move the object back to it's original position, using the motorised $y$-axis of the goniometer.
4. Carefully loosen either the azimuth stage or the right-angle bracket.
5. Move the object to the position, marked in step two. Note that an offset along the $x$- or $z$-axis is acceptable.
6. Tighten the loosened bolts and check the position of the calibration object in the live view. Note that the tightening of the bolts can move the object, either by rotational friction forces or because the limits of the play in the mounting of the azimuth stage or right-angle bracket are reached.
7. If the results are not satisfactory, some of the above steps can be repeated[6].

Go back to the method, subsection 3.2.2, or its results, section 4.3.

### A.2.3 Derivation - Mapping Area

The mapping area of the GRACE system is limited by the elevation, as given by (2.2) in subsection 2.3.1. In this section, we'll derive the mapping area, based on the maximum elevation angle.

---

[5] Note that is it assumed that the offset $y_m$ is relatively small and the displacement of the spherical calibration object can take place within the area imaged by the camera.

[6] For an offset below $100\,\mu$m manual adjustments are not easy. Tapping or other techniques might be used.

The mapping area is a sphere with part of it cutoff. The part that is cutoff can be referred to as a spherical cap. The area of a spherical cap is given by:

$$A = 2\pi r^2(1 - \cos\theta) \tag{A.1}$$

Here $A$ is the area of the cap, $r$ is the radius of the sphere and $\theta$ is the angle of the cap, as seen in Figure A.1.

The area of the sphere minus the cap gives the scannable range of the GRACE system. This evaluates to about 67 percent of the surface area of a sphere.

The area of a sphere is $4\pi r^2$. The area of the cap which represents that part which cannot be scanned is:

$$\begin{aligned} A_{cap} &= 2\pi r^2(1 - \cos(180° - 110°)) \\ &= 2\pi r^2(1 - \cos(70°)) \\ &\approx 2\pi r^2 \cdot 0.6580 \\ &= 4\pi r^2 \cdot 0.329 \end{aligned} \tag{A.2}$$

Neglecting the fact, that the camera sees slightly past the edge of the cap, 32.9 % of the sphere cannot be reached by the GRACE system. From this is can be concluded that, for an elevation limit of 110 °, about 67 % of the spherical scanning area can be scanned by the GRACE system.

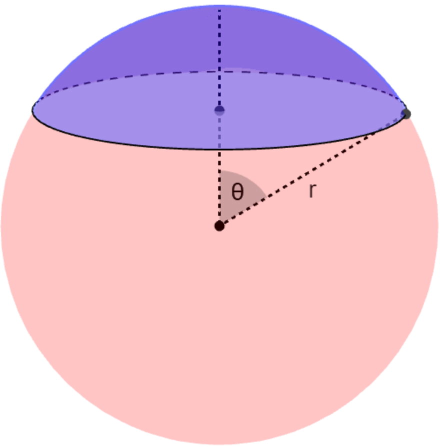

Figure A.1: Sphere cap in blue.

## A.3 Additional Images

### A.3.1 Goniometer Calibration 10x Improvement

The Y-axis offset error has been decreased by about a factor of 10. This is based on the estimated object centre positions determined using the simulation results shown in Figure A.3a and A.3b. The vertical offset for these simulated positions is [Y, Z], [306,-257] micrometer for the first measurement and close to [30,0] micrometer for the last measurement.

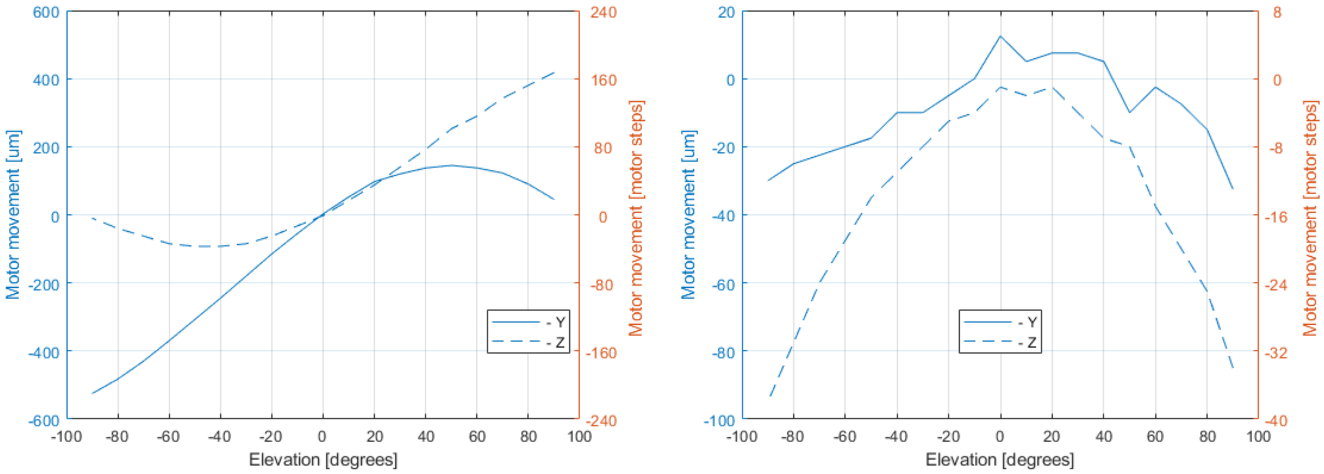

Figure A.2: Elevation calibration results measured for the first and last elevation calibration scan during the goniometer rotation axes calibration. Left the first measurement and on the right the last measurement. Note that in the last measurement the measurement for the Z-axis are skewed due to an elevation dependent offset.

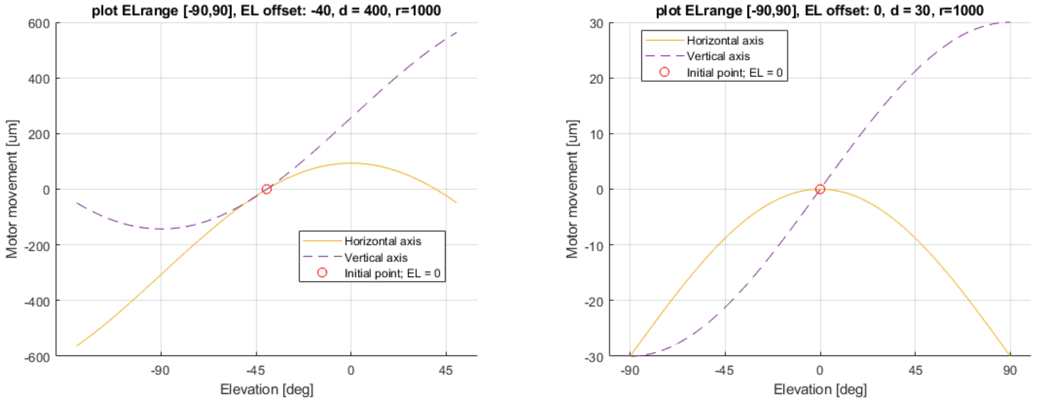

(a)

(b)

Figure A.3: **(a)** First curve fitting elevation calibration. **(b)** Last curve fitting elevation calibration. Note the difference in the amplitude.

### A.3.2 Boca Ball Bearing Images

Note that for all images, there is surface contamination.

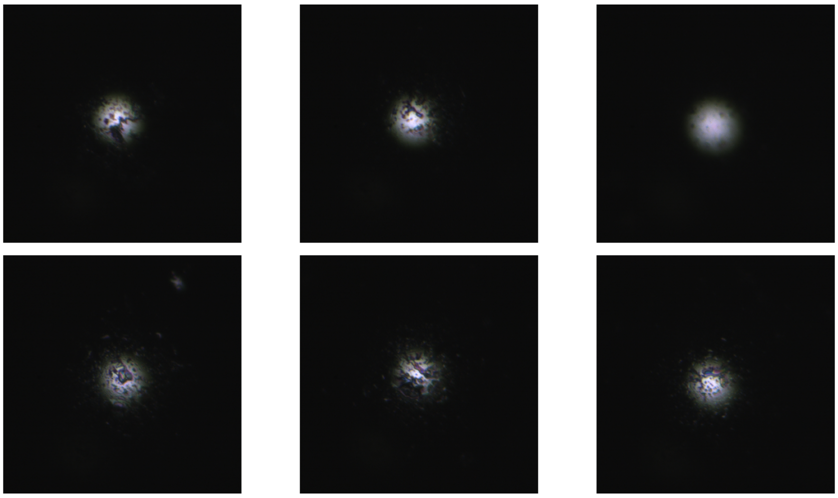

Figure A.4: Images of a 1 mm $Si_3N_4$ (black) ball bearing, from different perspectives.

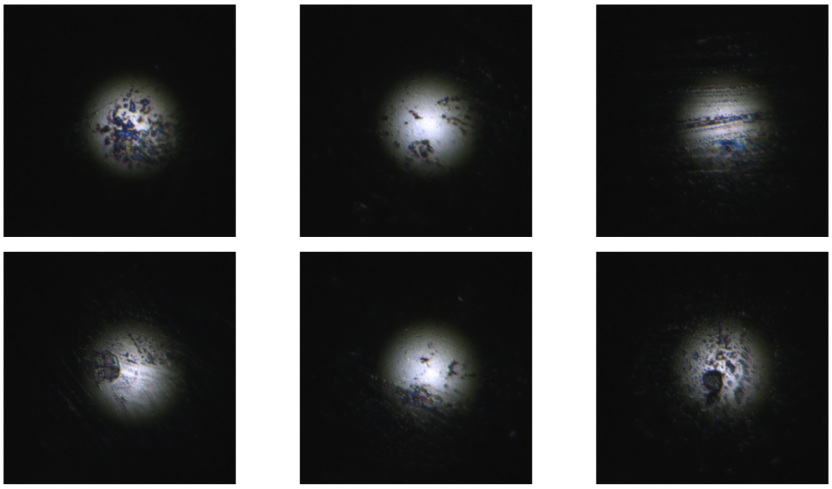

Figure A.5: Images of a 2 mm $Si_3N_4$ (black) ball bearing, from different perspectives.

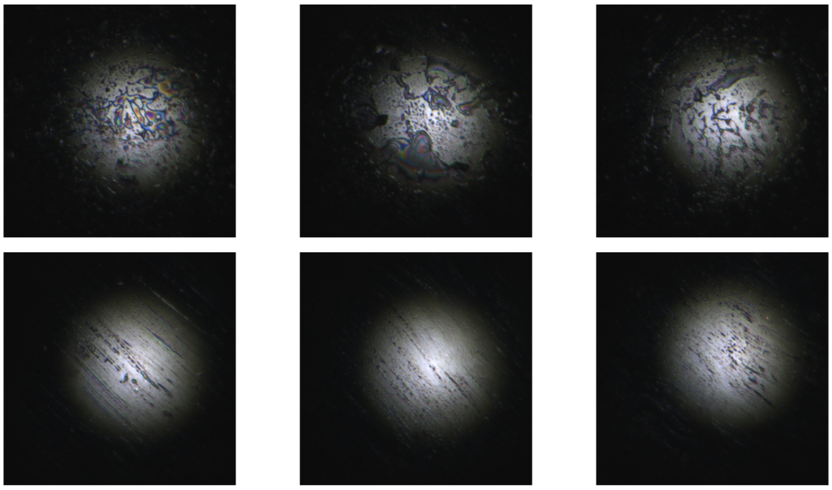

Figure A.6: Images of a 3 mm $Si_3N_4$ (black) ball bearing, from different perspectives.

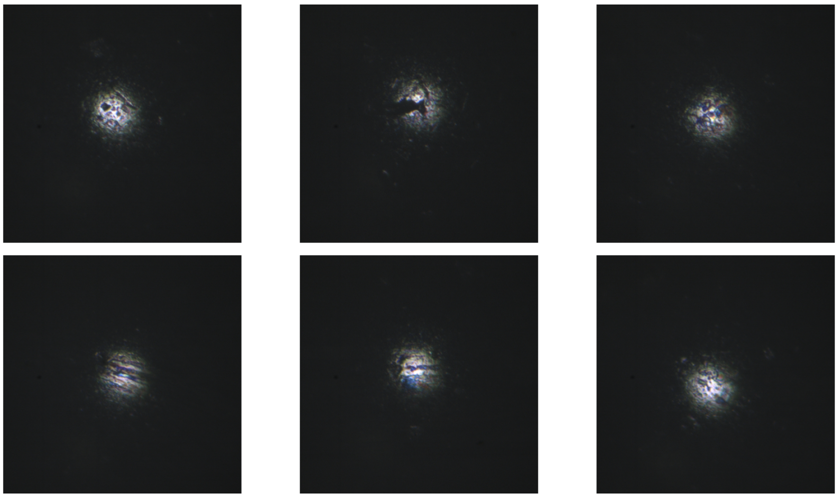

Figure A.7: Images of a 1 mm $ZrO_2$ (white) ball bearing, from different perspectives.

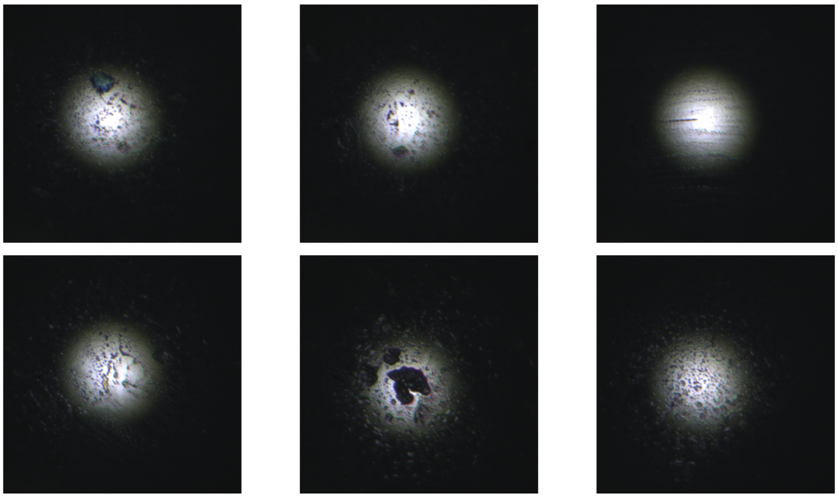

Figure A.8: Images of a 2 mm $ZrO_2$ (white) ball bearing, from different perspectives.

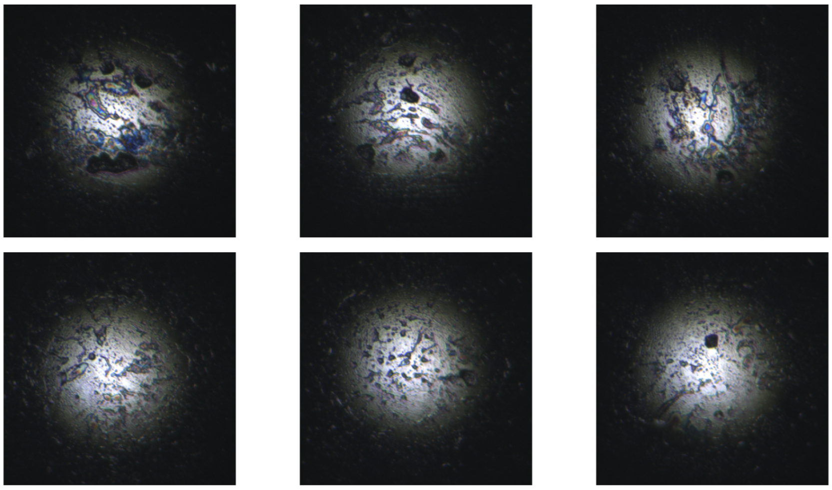

Figure A.9: Images of a 3 mm $ZrO_2$ (white) ball bearing, from different perspectives.

### A.3.3 Ball Bearing Image Analysis

Centre cut outs of a selection of the 3 mm black and white ball bearing images (Figure A.6 and A.9) can be seen in Figure A.10 and A.11. From these images, the brightness of each column is taken (average of highest values) and plotted. These plots visualise the maximum brightness from left to right. In Figure A.13 and A.12 it can be seen that the brightness of the white samples is higher than for the black samples (under the same light conditions). The black samples have lower brightness values outside the 'visible region', which indicates a higher contrast ratio compared the white samples. The higher contrast value of the black samples let to the choice of using those as a reference object subsection 2.2.1.

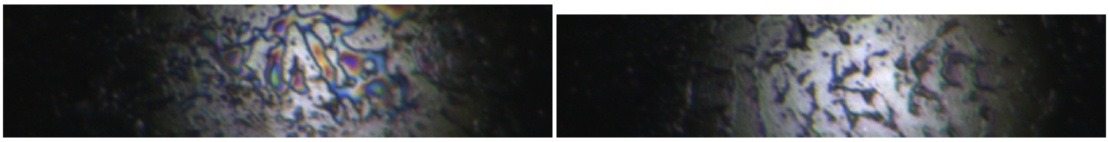

Figure A.10: Centre cut out of the 1st and 3rd sample from Figure A.6.

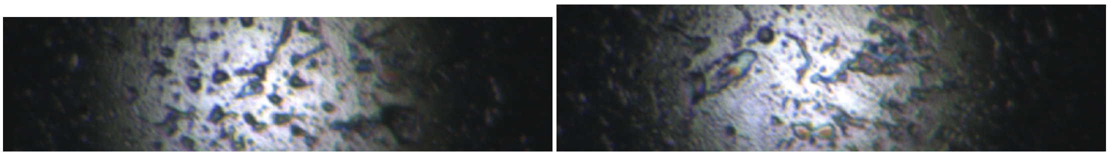

Figure A.11: Centre cut out of the 5th and 4th sample from Figure A.9.

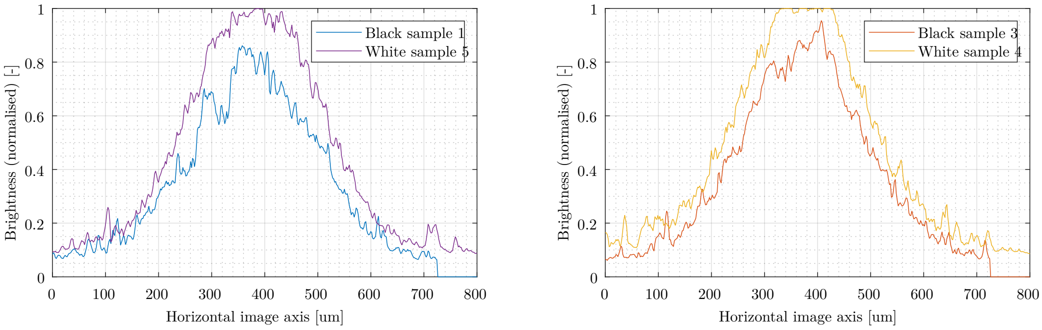

Figure A.12: Comparison of the white and black ball bearing brightness graphs. The samples that are compared are selected based on their similarities.

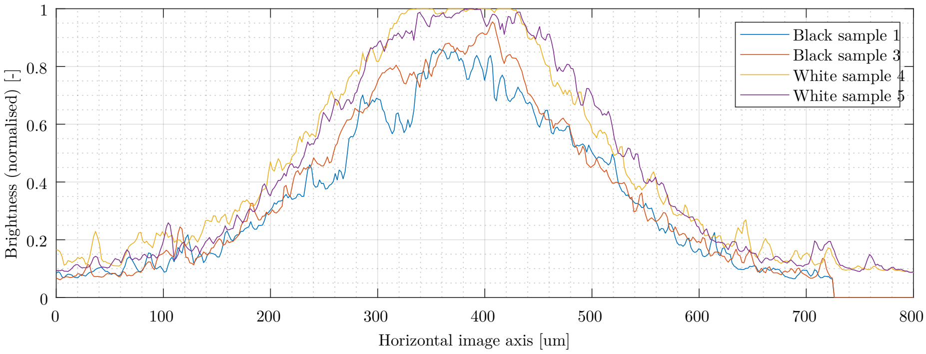

Figure A.13: Comparison of four brightness graphs of different samples from Figure A.10 and A.11.

### A.3.4 Goniometer Calibration

In this section, a selection of images is shown, which were made during the (re)construction of the GRACE setup, after the move from the *old* lab NB5113.0013 to the *new* lab LB5171.0312. Some of these images refer to the recalibration of the goniometer, briefly discussed in subsection 2.3.5. Some deviations in the goniometer setup were measured using a square. To exclude as much non-ideals as possible, all parts of the GRACE setup were calibrated using the square, among various other methods. Figure A.14 gives an impression.

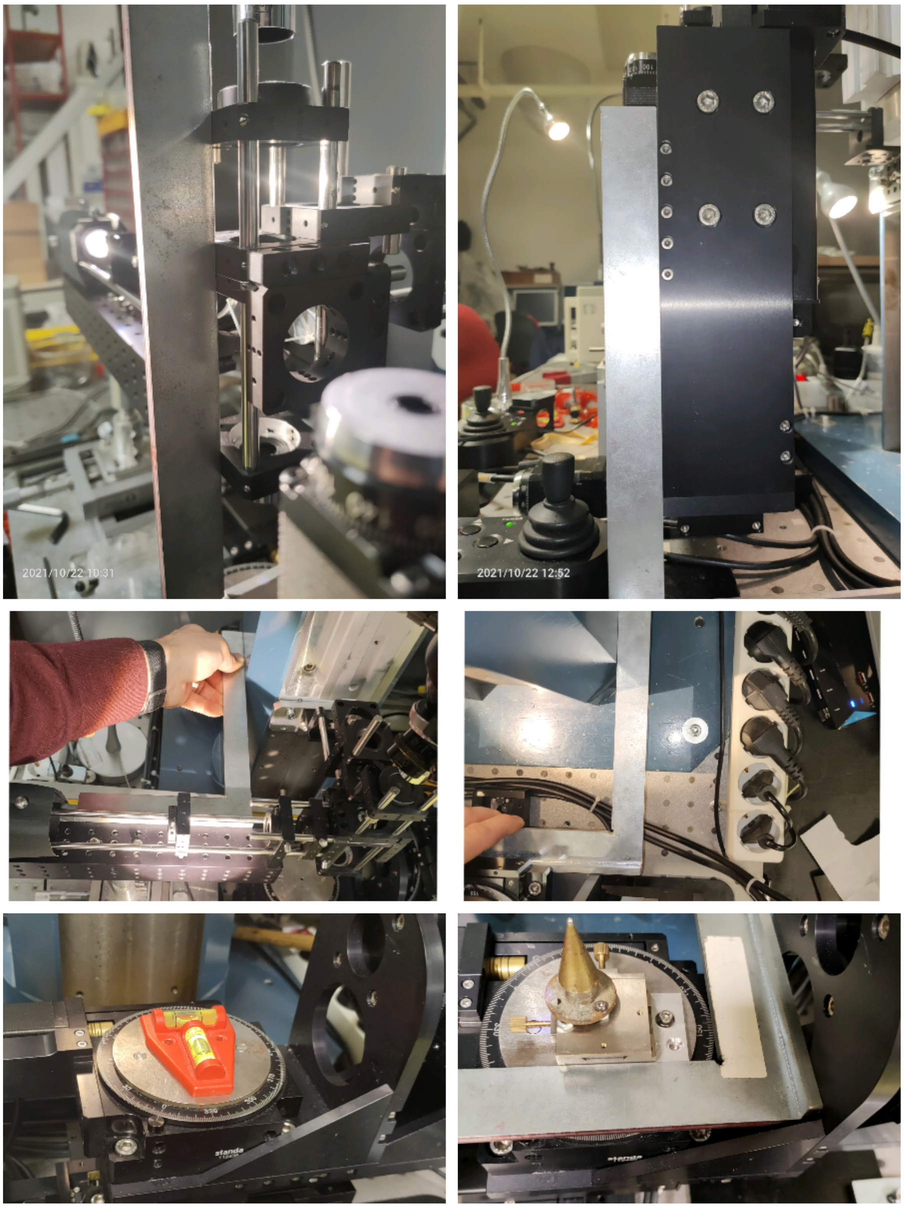

Figure A.14: Impression of calibrating the GRACE setup using a square. Additionally, various surfaces were compared using a small or larger spirit level.

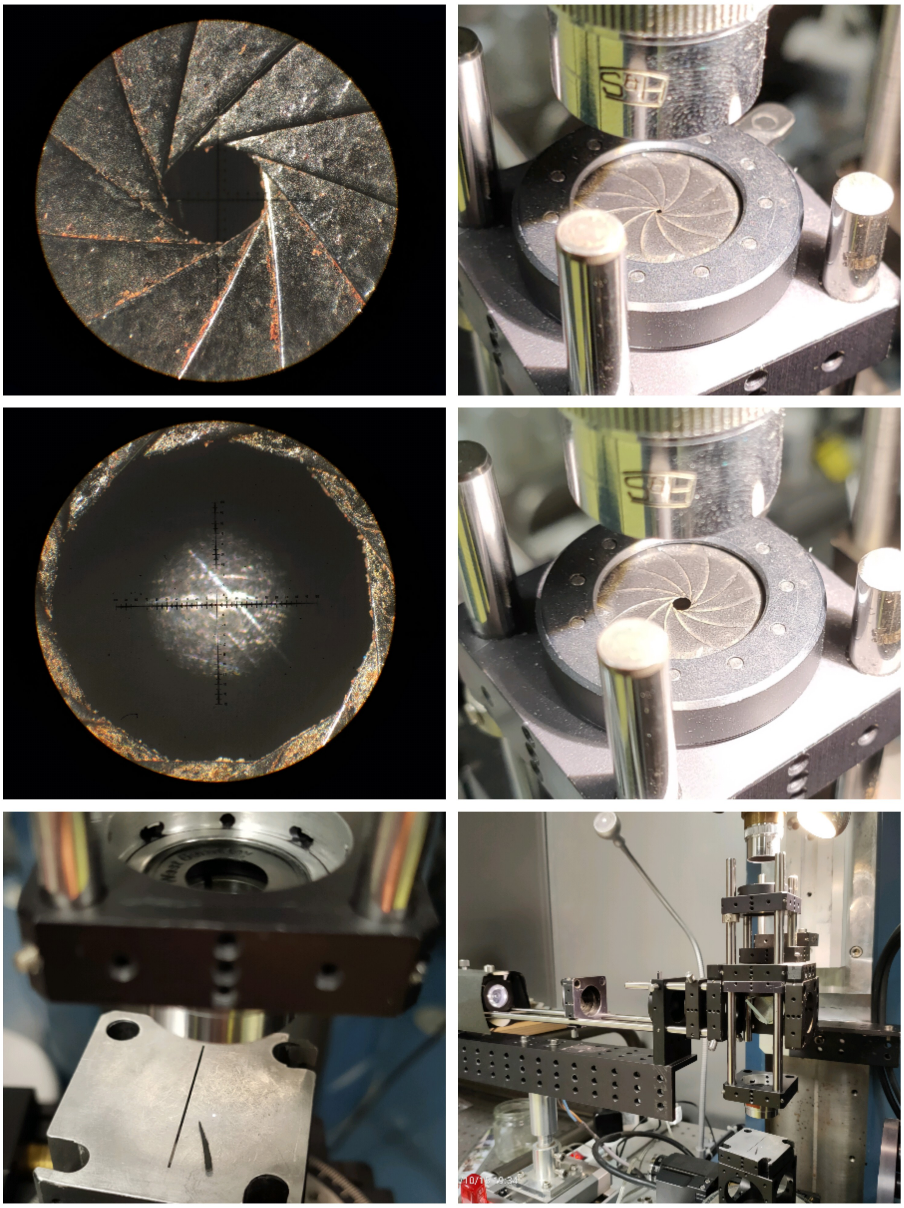

Figure A.15: Initial microscope testing after switching to the x5 lens.

### A.3.5 Focussing for Zstack data

A script or function called referenced to as Zstack is used to take a number of images for a certain height range resulting in 4D image data files. By running the Z-stack data through an script which eveluates the image sharpness, its basically (simulating) autofocus after the scan is already done. This allowed for the confirmation of the current Sumfourier method giving the best results when compared to 5 other selected candidates from previous work [17].

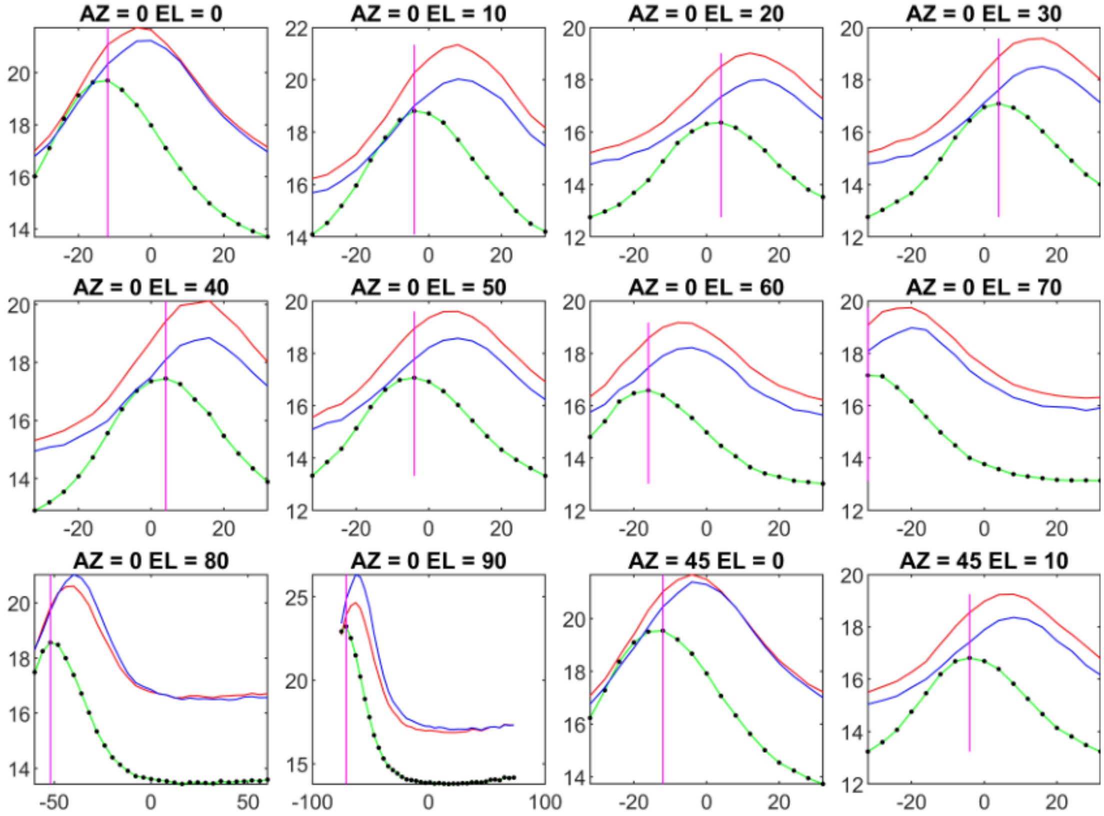

Figure A.16: Show best focus values for a specific colour channel. Magenta line indicates location of maximum focus-value for that channel. The data corresponding to the red, green and blue colour channels are coloured similarly in the plots.

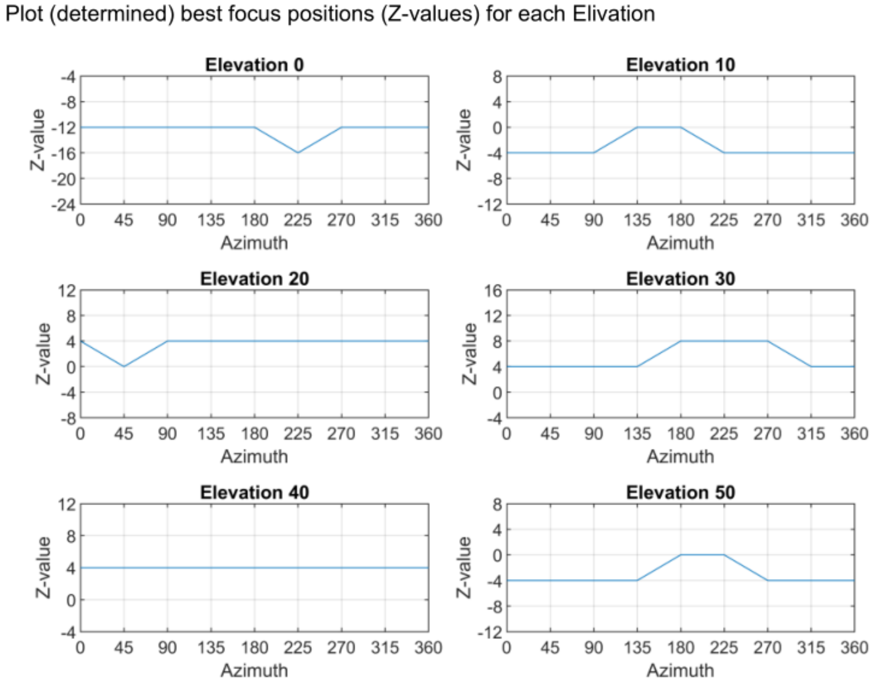
Plot (determined) best focus positions (Z-values) for each Elivation
Elevation 0
Elevation 10
Elevation 20
Elevation 30
Elevation 40
Elevation 50
Z-value
Azimuth
0 45 90 135 180 225 270 315 360
-4 -8 -12 -16 -20 -24
8 4 0 -4 -8 -12
12 8 4 0 -4 -8
16 12 8 4 0 -4
12 8 4 0 -4
8 4 0 -4 -8 -12

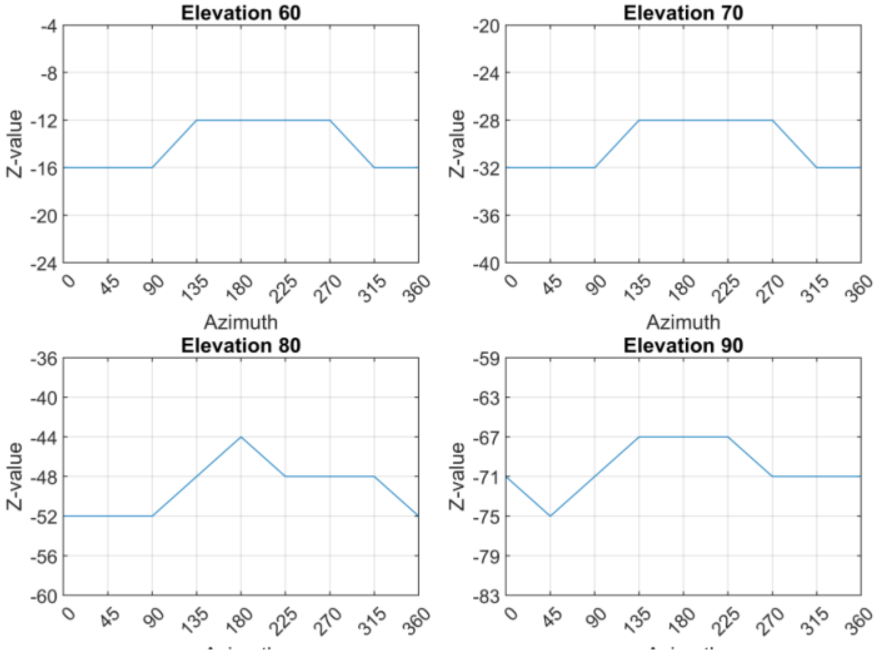
Elevation 60
Elevation 70
Elevation 80
Elevation 90
Z-value
Azimuth
0 45 90 135 180 225 270 315 360
-4 -8 -12 -16 -20 -24
-20 -24 -28 -32 -36 -40
-36 -40 -44 -48 -52 -56 -60
-59 -63 -67 -71 -75 -79 -83

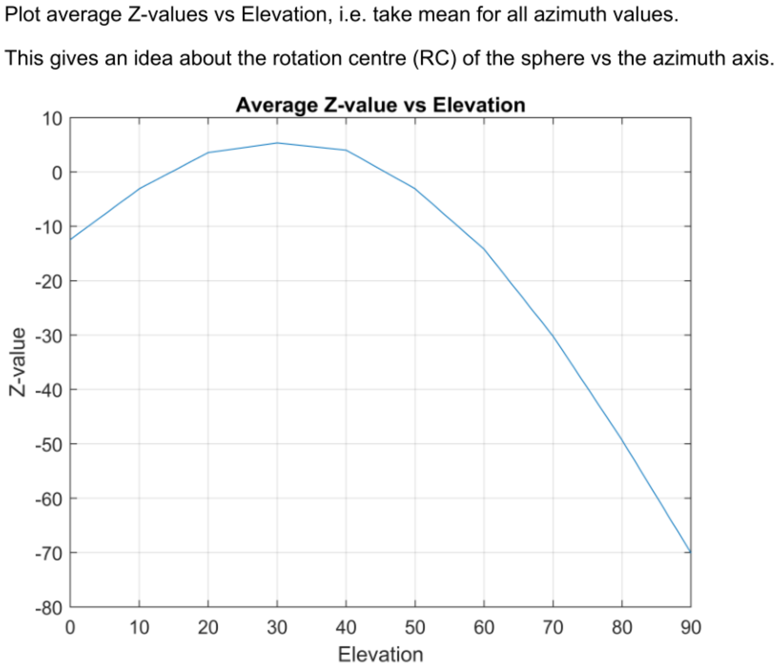

Plot average Z-values vs Elevation, i.e. take mean for all azimuth values.

This gives an idea about the rotation centre (RC) of the sphere vs the azimuth axis.

Figure A.17

### A.3.6 getsnapshotMulti_JJ

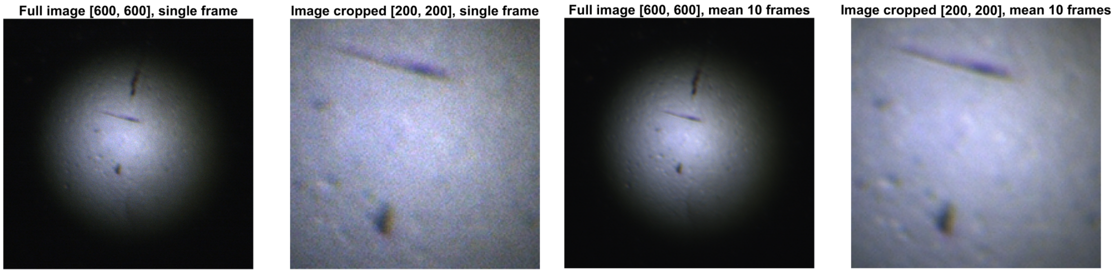

Figure A.18: Example of results made possible by the `getsnapshotMulti_JJ` MATLABfunction. By capturing multiple frames and averaging them into one image (frame) noise is reduced. This is a low complexity technique to reduce noise.

## A.4 All 3D image data in succession

Here all the different plots created from the raw and adjusted data of the three calibration offset scans are showed for the first time or repeated from the thesis. The parameter about the specific scans can be found in Table 4.1 and 4.2.

## A.4.1 First: No Offset Mapping

Data can be recreated using `SEER_JJ_scratchv4_data7jan.m` and `VisualizeBallData_improved_method_JJ.m`, which can be found at [1].

### First: Raw Data

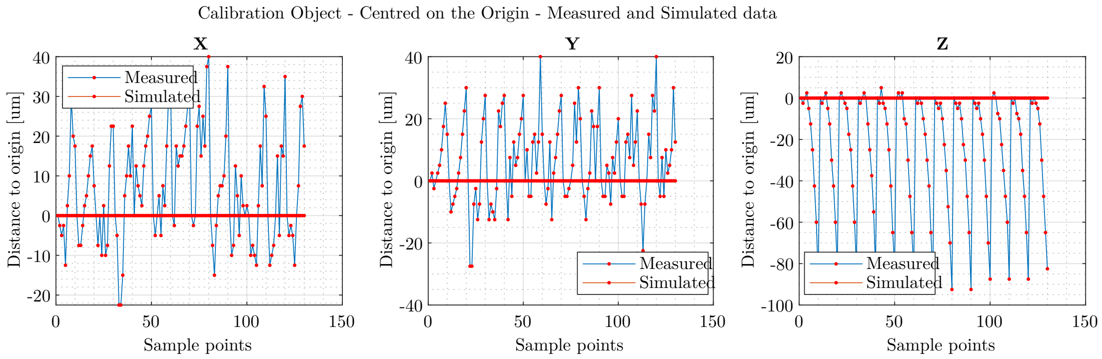

Figure A.19: Measured $x$-, $y$-, and $z$-data and the simulated $x$-, $y$-, and $z$-data for the object centre.

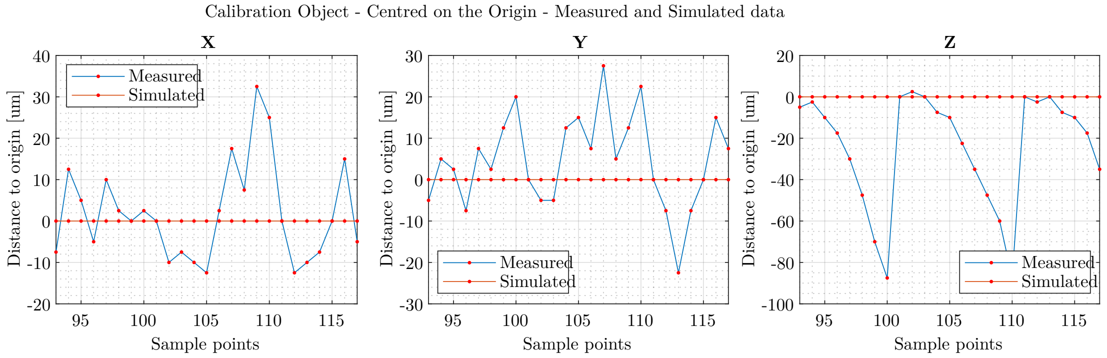

Figure A.20: Measured $x$-, $y$-, and $z$-data and the simulated $x$-, $y$-, and $z$-data for the object centre.

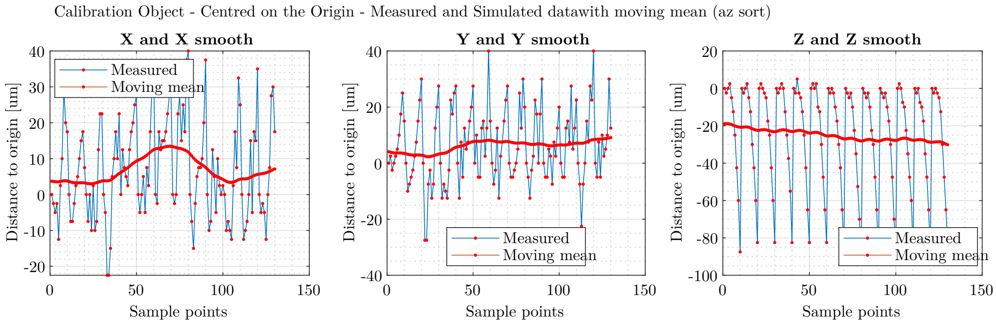

Figure A.21: Measured $x$-, $y$-, and $z$-data, including a moving mean. Note that the data is sorted for the (by default) azimuth values.

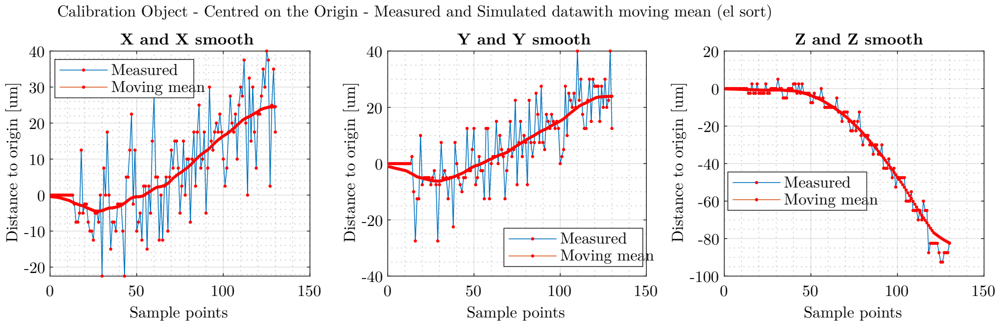

Figure A.22: Measured $x$-, $y$-, and $z$-data, including a moving mean. Note that the data is sorted for the elevation values.

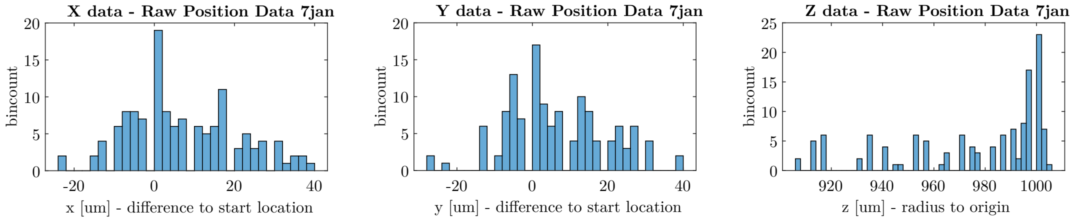

Figure A.23: Histograms of the measured $x$-, $y$-, and $z$-data. The bin width is 2.

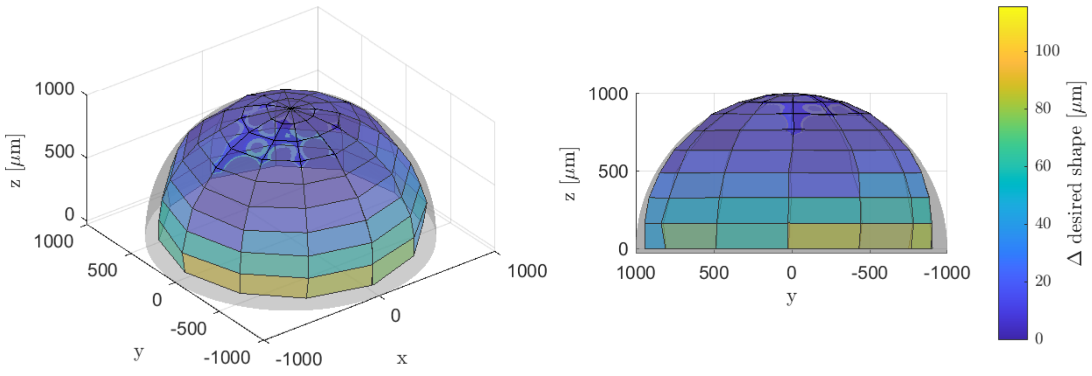

(a) XYZ

(b) YZ

Figure A.24: 3D mesh plot of the measured goniometer data. Azimuth and elevation viewing angles are [-37.5 30] and [-90 0] for the left and right plot respectively. The height values are also use to colour the mesh.

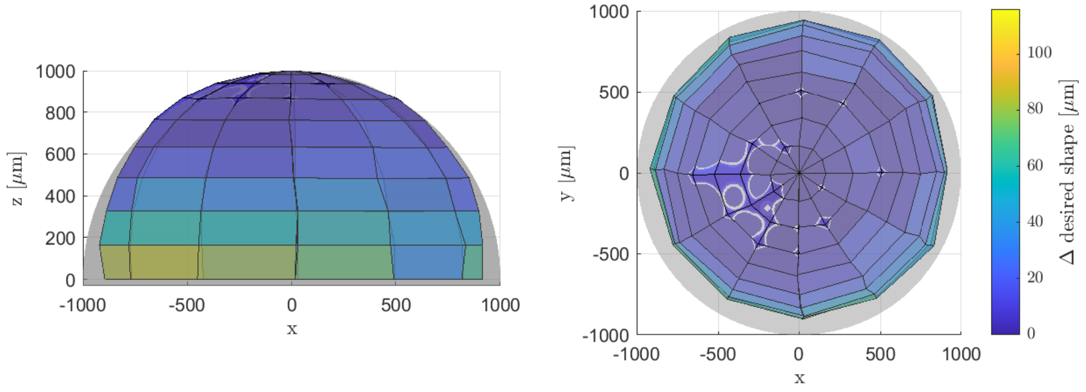

(a) XZ

(b) XY

Figure A.25: 3D mesh plot of the measured goniometer data. Azimuth and elevation viewing angles are [0 0] and [0 90] for the left and right plot respectively. The height values are also use to colour the mesh.

### A.4.2 Second: Y-offset Mapping

Data can be recreated using `SEER_JJ_scratchv4_data10jan.m` and `VisualizeBallData_improved_method_JJ.m`, which can be found at [1].

### Second: Raw Data

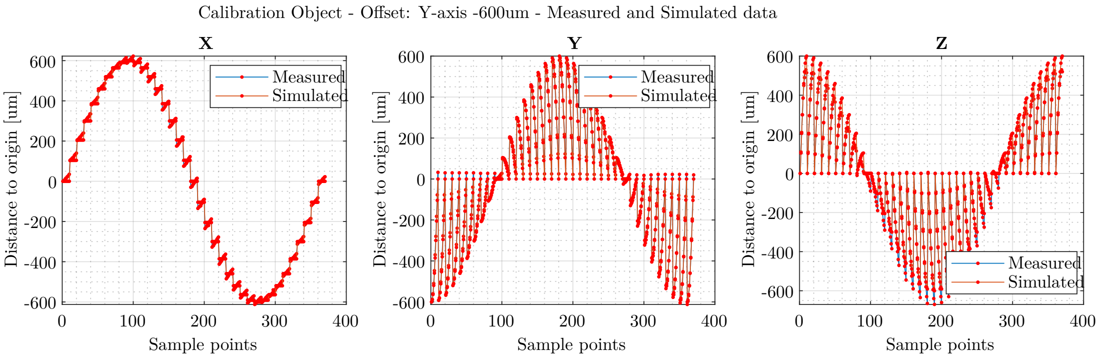

Figure A.26: Measured $x$-, $y$-, and $z$-data and the simulated $x$-, $y$-, and $z$-data for the object centre.

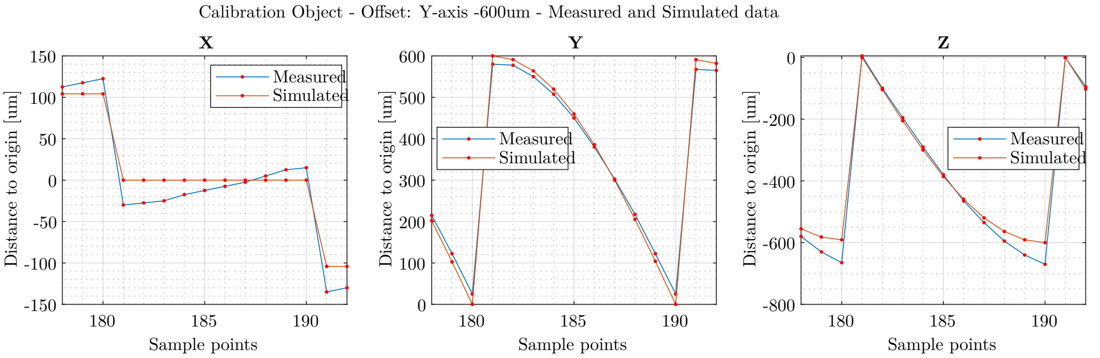

Figure A.27: Measured $x$-, $y$-, and $z$-data and the simulated $x$-, $y$-, and $z$-data for the object centre.

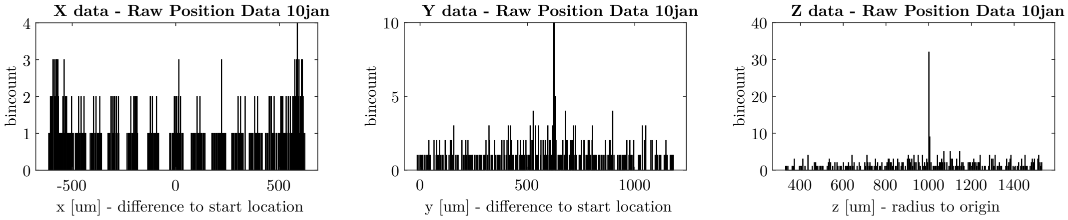

Figure A.28: Histograms of the measured $x$-, $y$-, and $z$-data. The bin width is 2.

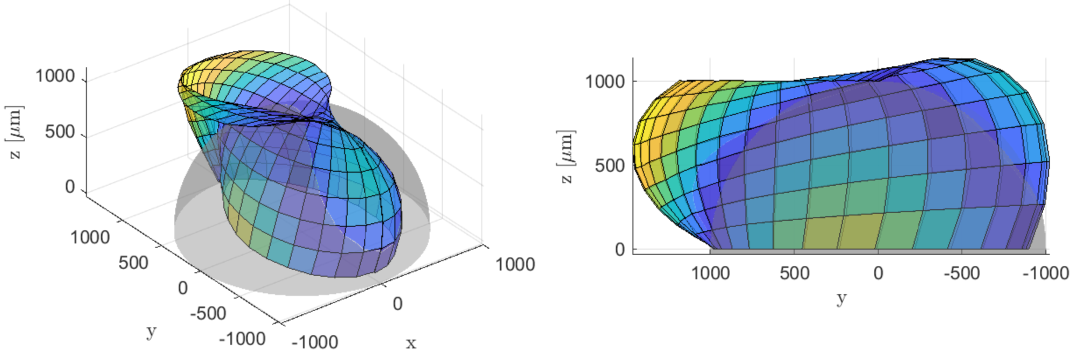

(a) XYZ

(b) YZ

Figure A.29: 3D mesh plot of the measured goniometer data. Azimuth and elevation viewing angles are [-37.5 30] and [-90 0] for the left and right plot respectively. The height values are also use to colour the mesh.

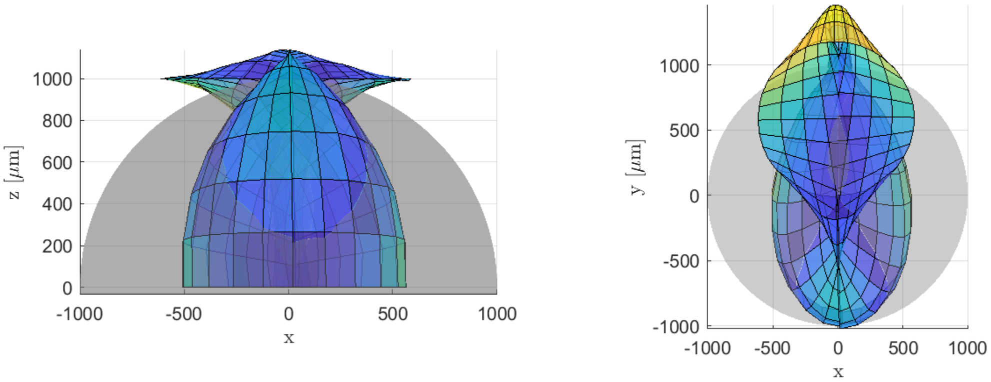

(a) XZ

(b) XY

Figure A.30: 3D mesh plot of the measured goniometer data. Azimuth and elevation viewing angles are [0 0] and [0 90] for the left and right plot respectively. The height values are also use to colour the mesh.

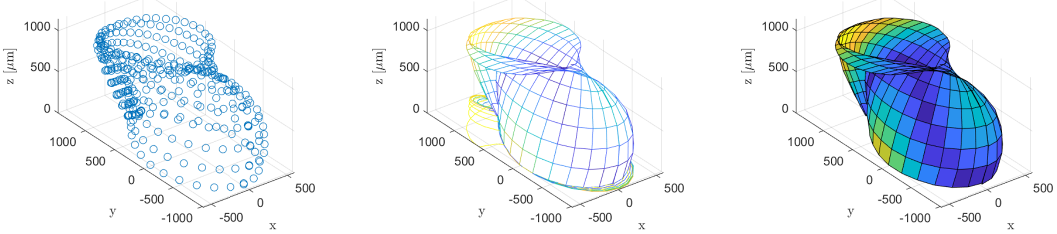

Figure A.31: Bonus figures, results plotted with *scatter3*, *mesh* and *surf*.

## Second: Adjusted Data

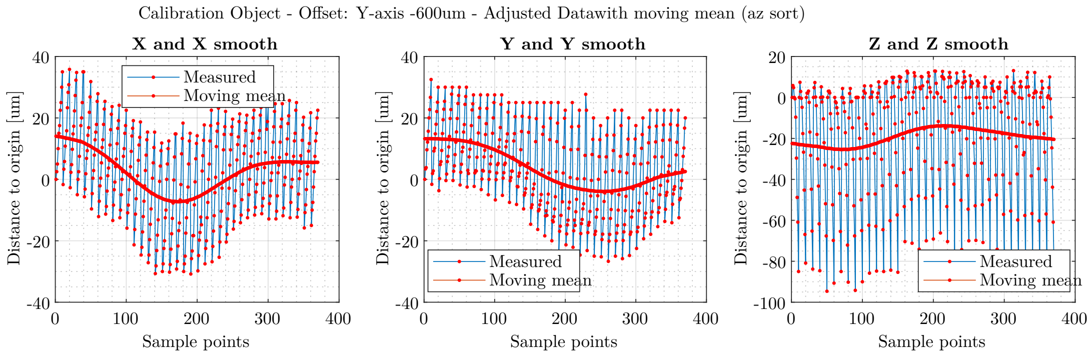

Figure A.32: Measured $x$-, $y$-, and $z$-data, including a moving mean. Note that the data is sorted for the (by default) azimuth values.

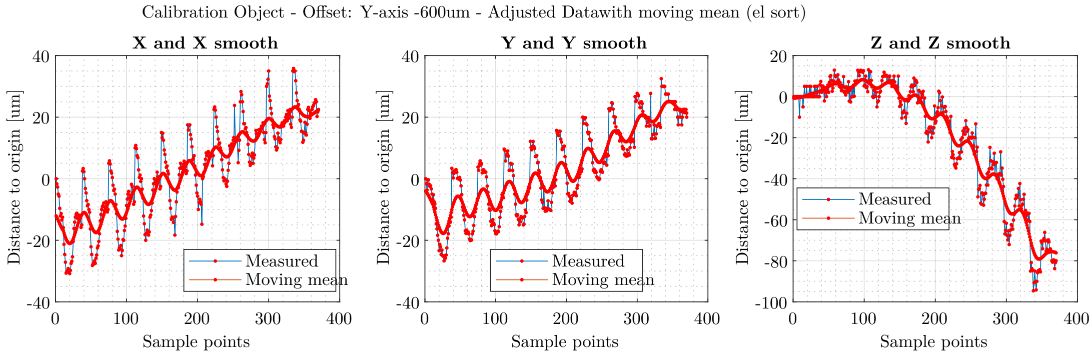

Figure A.33: Measured $x$-, $y$-, and $z$-data, including a moving mean. Note that the data is sorted for the elevation values.

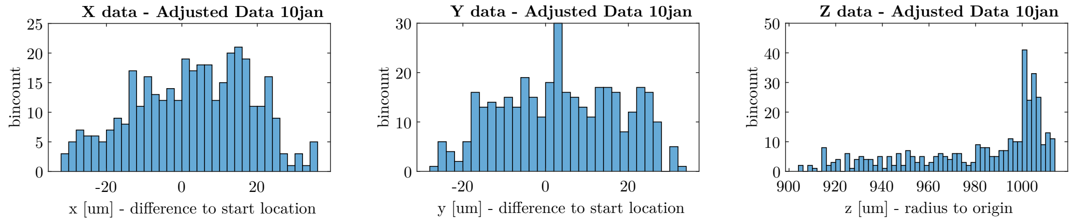

Figure A.34: Histograms of the measured $x$-, $y$-, and $z$-data. The bin width is 2.

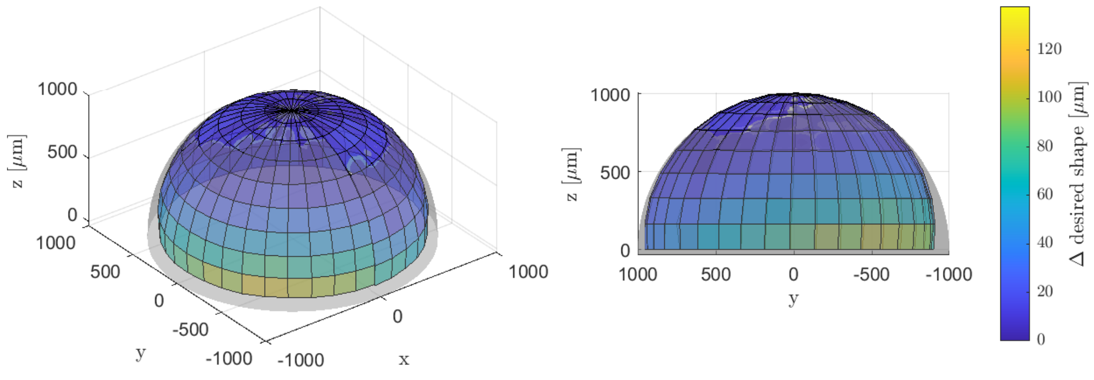

(a) XYZ (b) YZ

Figure A.35: 3D mesh plot of the measured goniometer data. Azimuth and elevation viewing angles are [-37.5 30] and [-90 0] for the left and right plot respectively. The height values are also use to colour the mesh.

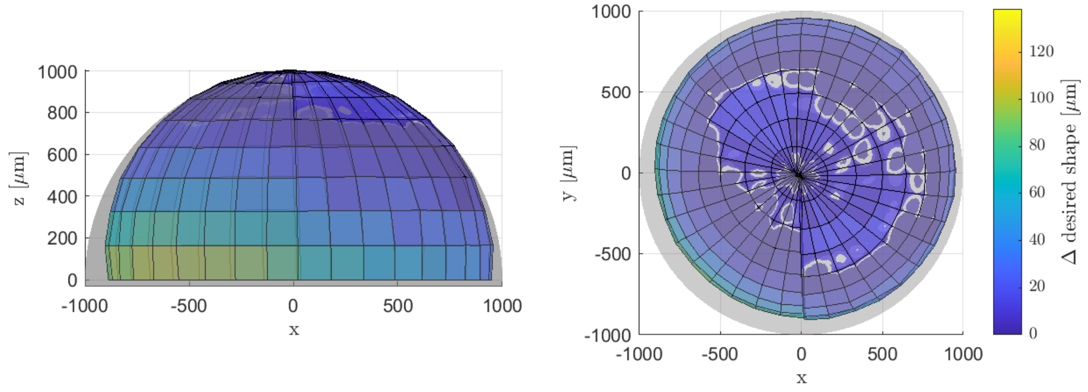

(a) XZ (b) XY

Figure A.36: 3D mesh plot of the measured goniometer data. Azimuth and elevation viewing angles are [0 0] and [0 90] for the left and right plot respectively. The height values are also use to colour the mesh.

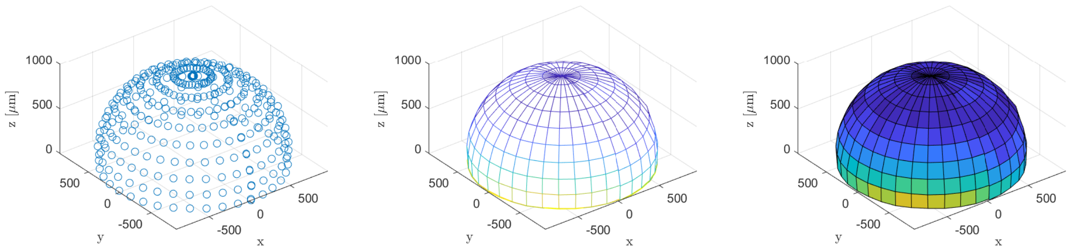

Figure A.37: Bonus figures, results plotted with *scatter3*, *mesh* and *surf*.

### A.4.3 Thirth: XY-offset Mapping

Data can be recreated using `SEER_JJ_scratchv4_data14jan.m` and `VisualizeBallData_improved_method_JJ.m`, which can be found at [1].

#### Thirth: Raw Data

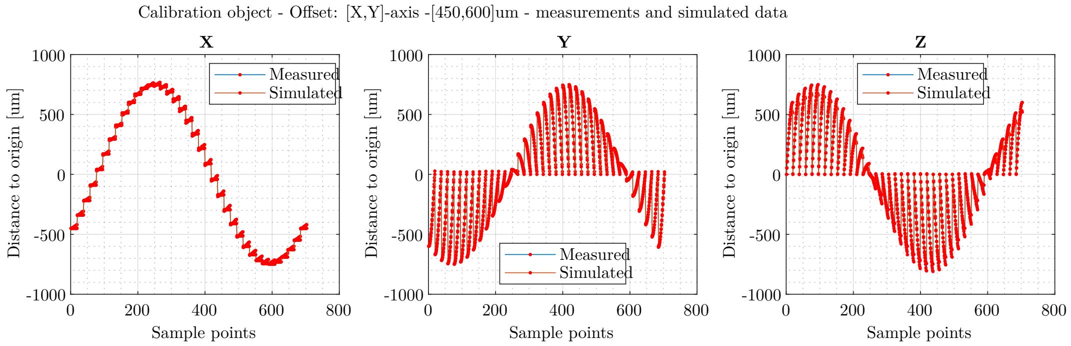

Figure A.38: Measured $x$-, $y$-, and $z$-data and the simulated $x$-, $y$-, and $z$-data for the object centre.

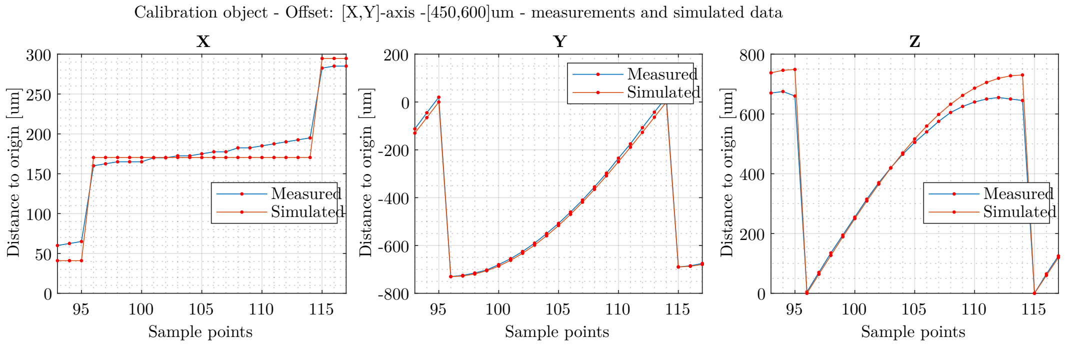

Figure A.39: Measured $x$-, $y$-, and $z$-data and the simulated $x$-, $y$-, and $z$-data for the object centre.

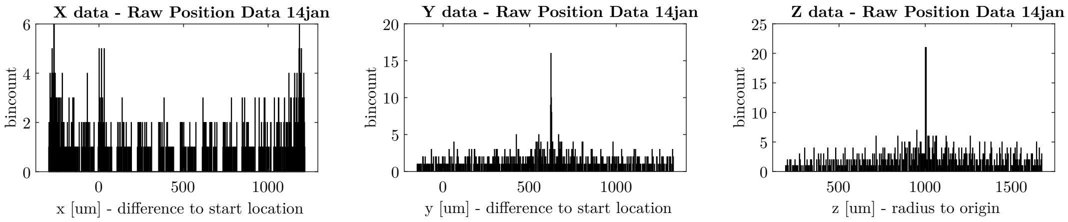

Figure A.40: Histograms of the measured $x$-, $y$-, and $z$-data. The bin width is 2.

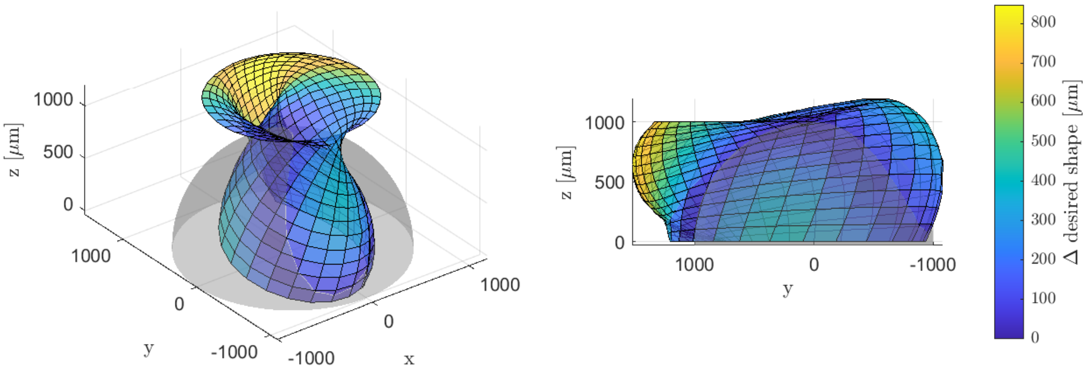

(a) XYZ

(b) YZ

Figure A.41: 3D mesh plot of the measured goniometer data. Azimuth and elevation viewing angles are [-37.5 30] and [-90 0] for the left and right plot respectively. The height values are also use to colour the mesh.

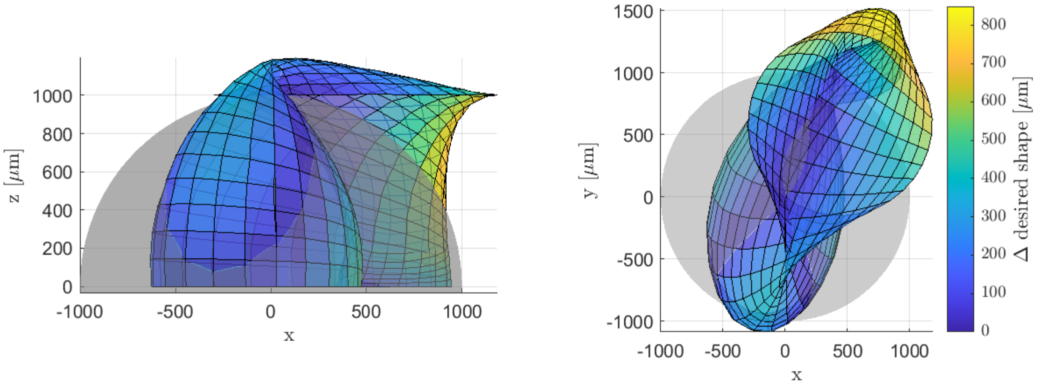

(a) XZ

(b) XY

Figure A.42: 3D mesh plot of the measured goniometer data. Azimuth and elevation viewing angles are [0 0] and [0 90] for the left and right plot respectively. The height values are also use to colour the mesh.

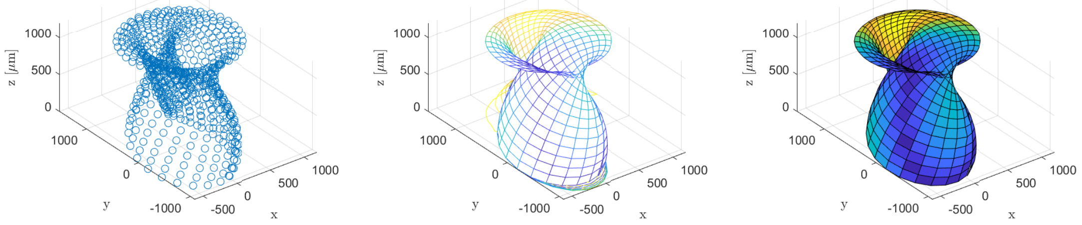

Figure A.43: Bonus figures, results plotted with *scatter3*, *mesh* and *surf*.

### Thirth: Adjusted Data

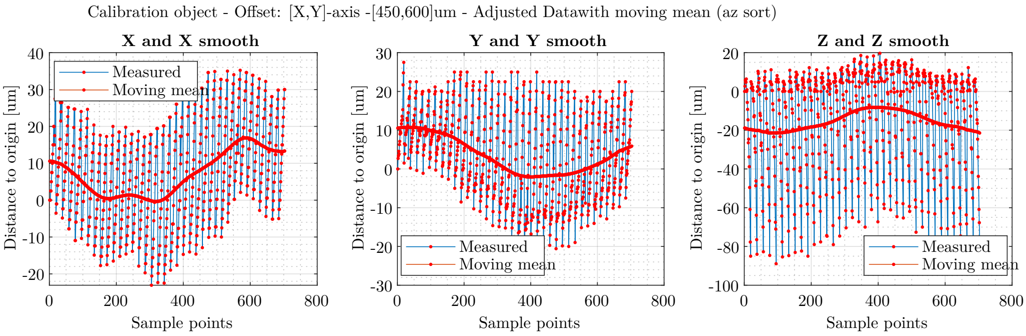

Figure A.44: Measured $x$-, $y$-, and $z$-data, including a moving mean. Note that the data is sorted for the (by default) azimuth values.

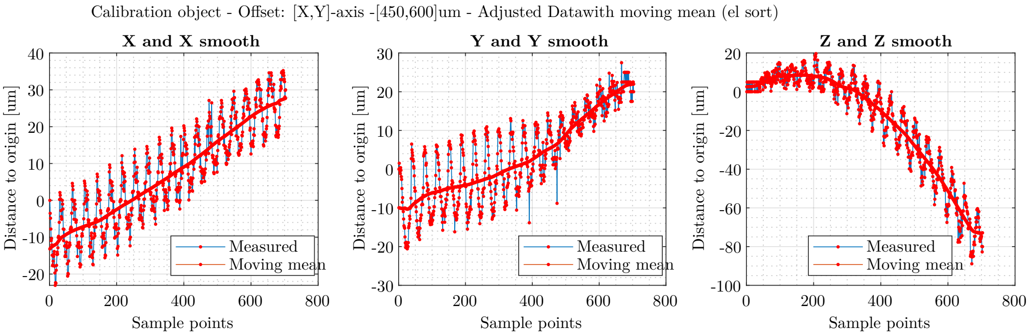

Figure A.45: Measured $x$-, $y$-, and $z$-data, including a moving mean. Note that the data is sorted for the elevation values.

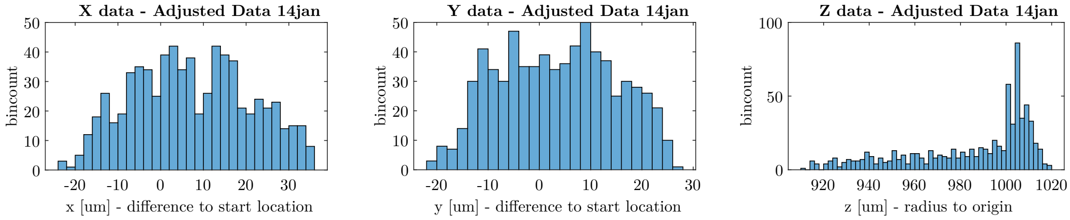

Figure A.46: Histograms of the measured $x$-, $y$-, and $z$-data. The bin width is 2.

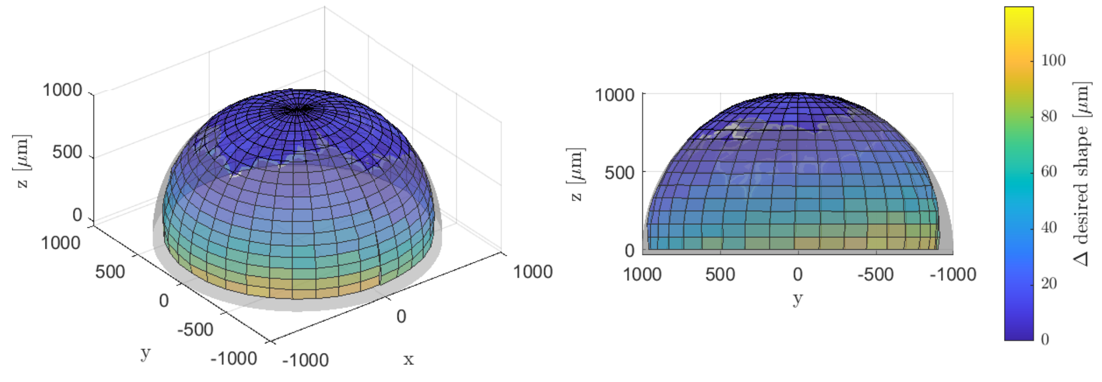

(a) XYZ

(b) YZ

Figure A.47: 3D mesh plot of the measured goniometer data. Azimuth and elevation viewing angles are [-37.5 30] and [-90 0] for the left and right plot respectively. The height values are also use to colour the mesh.

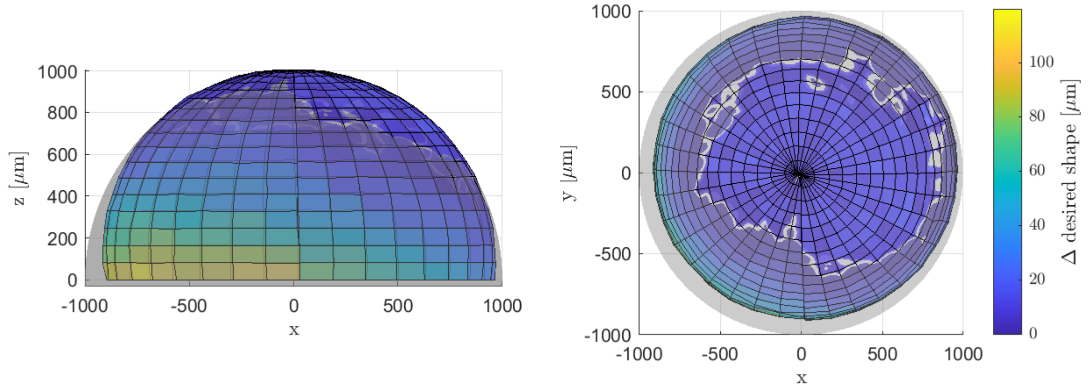

(a) XZ

(b) XY

Figure A.48: 3D mesh plot of the measured goniometer data. Azimuth and elevation viewing angles are [0 0] and [0 90] for the left and right plot respectively. The height values are also use to colour the mesh.

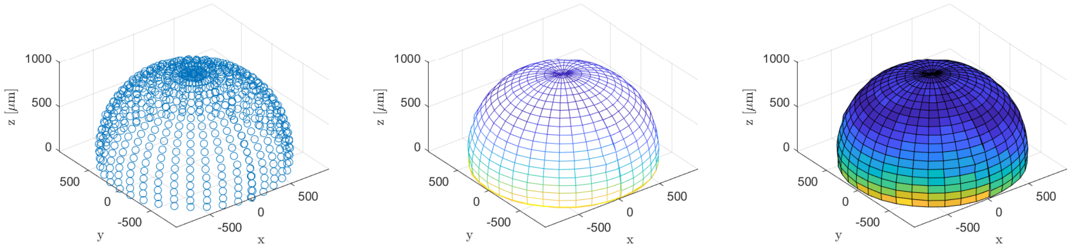

Figure A.49: Bonus figures, results plotted with *scatter3*, *mesh* and *surf*.

### A.4.4 Fourth: XYZ-offset Mapping

Data can be recreated using `SEER_JJ_scratchv4_data14jan.m` and `VisualizeBallData_improved_method_JJ.m`, which can be found at [1].

#### Fourth: Raw Data

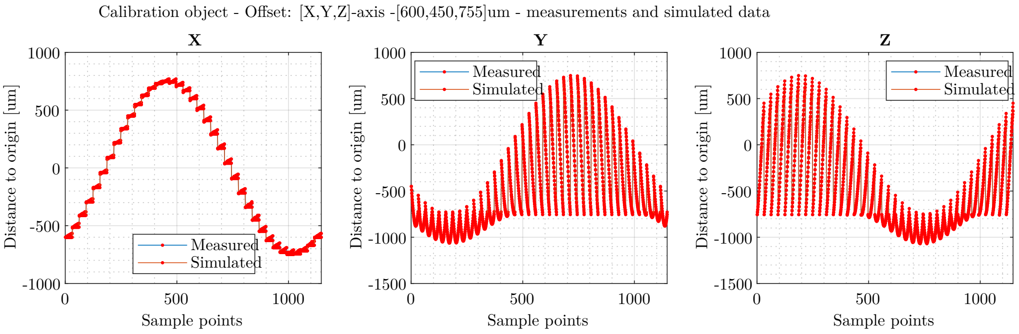

Figure A.50: Measured $x$-, $y$-, and $z$-data and the simulated $x$-, $y$-, and $z$-data for the object centre.

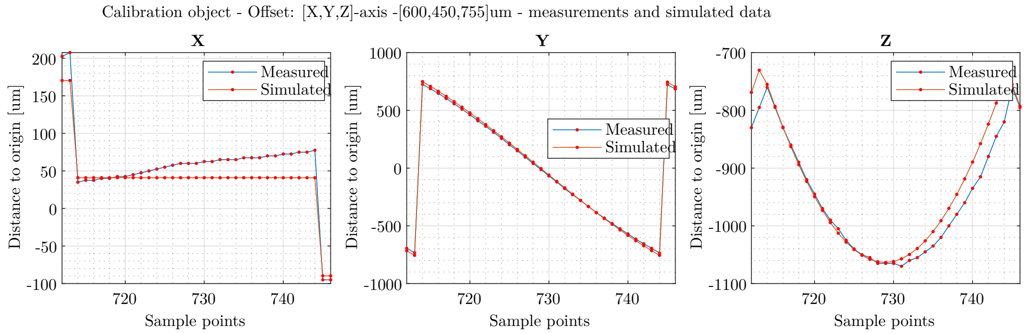

Figure A.51: Measured $x$-, $y$-, and $z$-data and the simulated $x$-, $y$-, and $z$-data for the object centre.

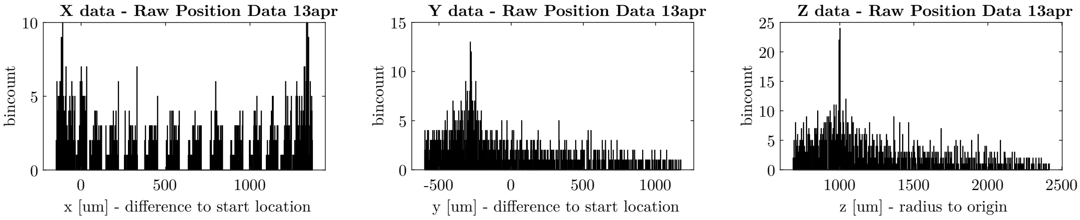

Figure A.52: Histograms of the measured $x$-, $y$-, and $z$-data. The bin width is 2.

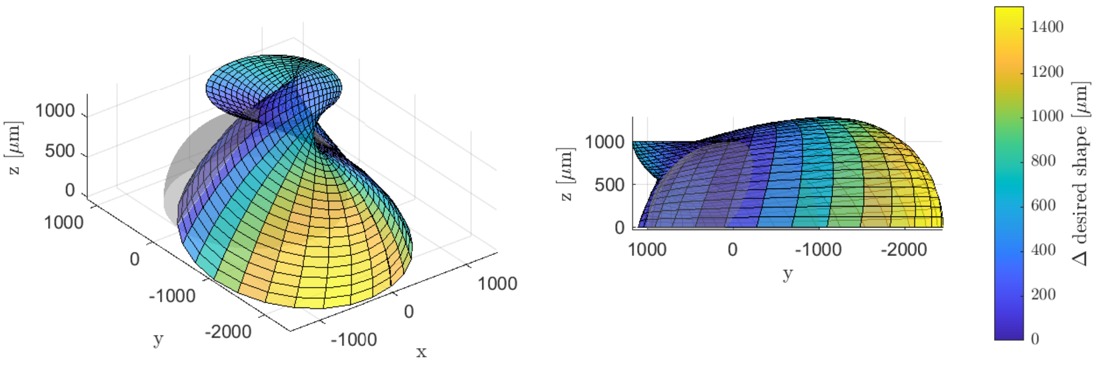

(a) XYZ

(b) YZ

Figure A.53: 3D mesh plot of the measured goniometer data. Azimuth and elevation viewing angles are [-37.5 30] and [-90 0] for the left and right plot respectively. The height values are also use to colour the mesh.

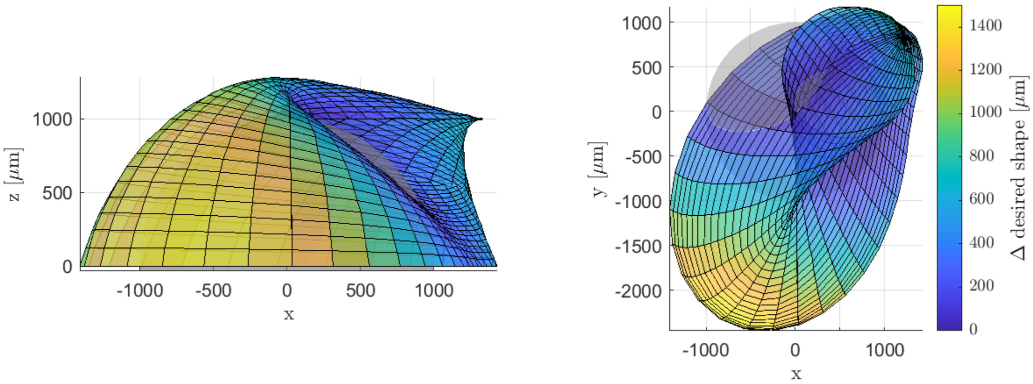

(a) XZ

(b) XY

Figure A.54: 3D mesh plot of the measured goniometer data. Azimuth and elevation viewing angles are [0 0] and [0 90] for the left and right plot respectively. The height values are also use to colour the mesh.

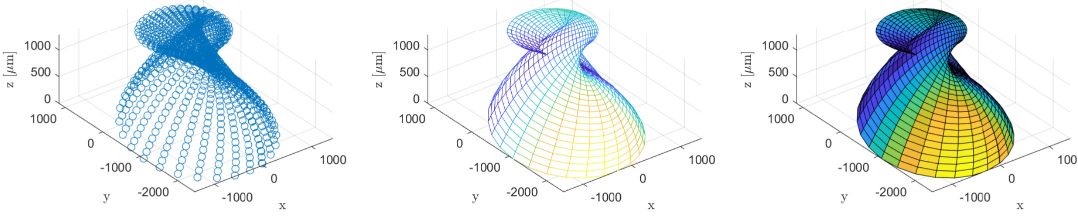

Figure A.55: Bonus figures, results plotted with *scatter3*, *mesh* and *surf*.

### Fourth: Adjusted Data

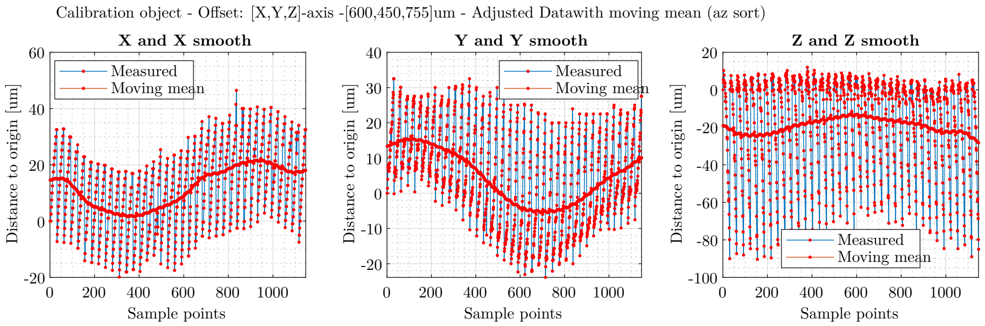

Figure A.56: Measured $x$-, $y$-, and $z$-data, including a moving mean. Note that the data is sorted for the (by default) azimuth values.

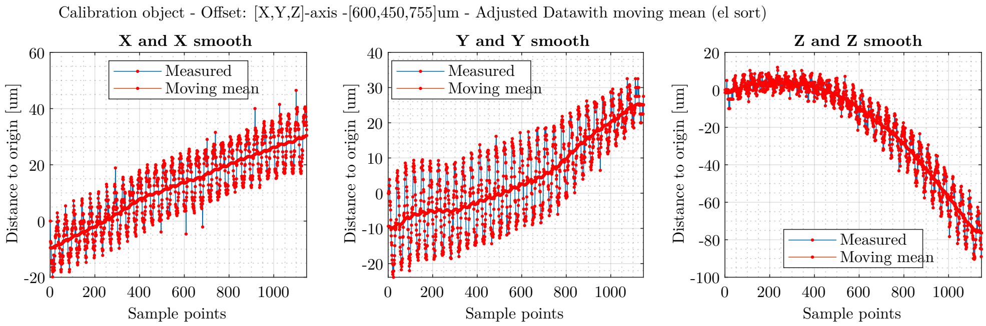

Figure A.57: Measured $x$-, $y$-, and $z$-data, including a moving mean. Note that the data is sorted for the elevation values.

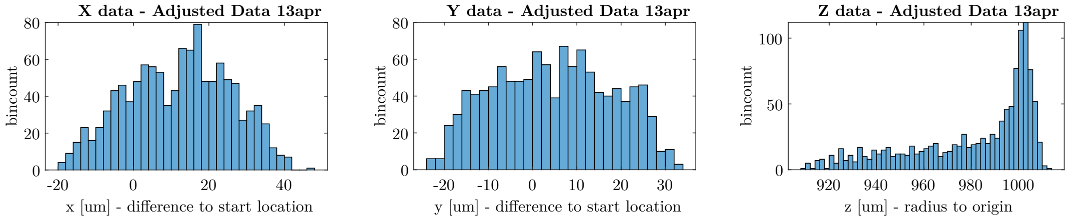

Figure A.58: Histograms of the measured $x$-, $y$-, and $z$-data. The bin width is 2.

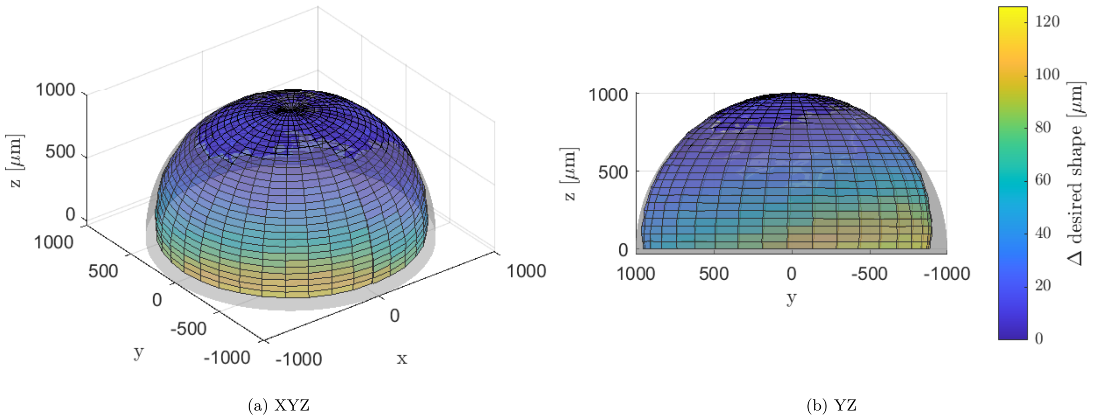

(a) XYZ

(b) YZ

Figure A.59: 3D mesh plot of the measured goniometer data. Azimuth and elevation viewing angles are [-37.5 30] and [-90 0] for the left and right plot respectively. The height values are also use to colour the mesh.

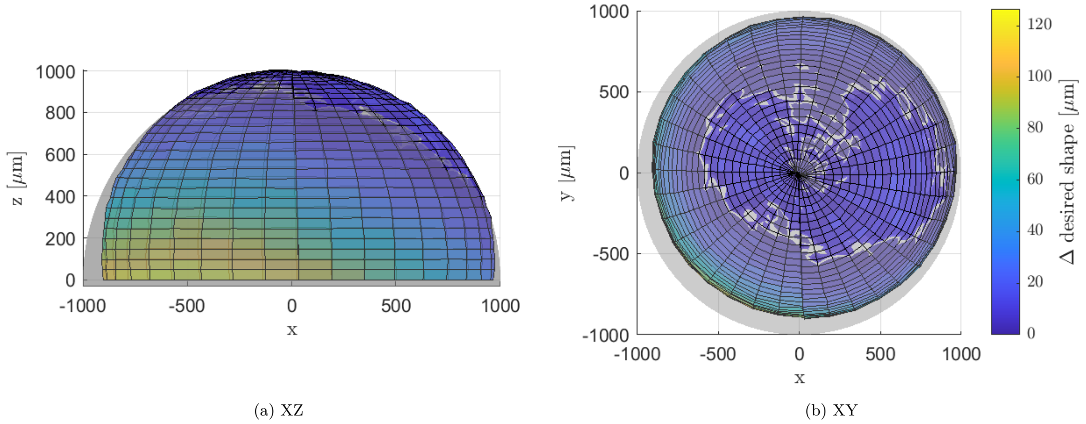

(a) XZ

(b) XY

Figure A.60: 3D mesh plot of the measured goniometer data. Azimuth and elevation viewing angles are [0 0] and [0 90] for the left and right plot respectively. The height values are also use to colour the mesh.

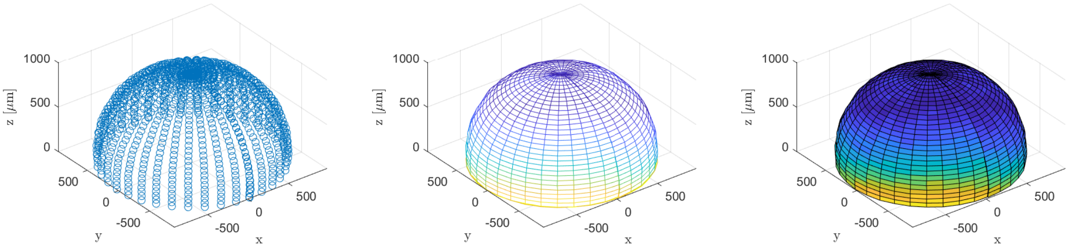

Figure A.61: Bonus figures, results plotted with *scatter3*, *mesh* and *surf*.

# Bibliography

[1] J. J. van Vliet, “Github repository,” 1 2022. [Online]. Available: https://github.com/SustainableBlueDuck/MRP-GRACE-JJ-2021-2022.git

[2] “Ball Terms & Definitions,” Jan 2022, [Online; accessed 18. Jan. 2022]. [Online]. Available: https://web.archive.org/web/20100225035209/http://www.hooverprecision.com:80/html/ball_terms_____definitions.html

[3] G. Taylor, P. Tichit, M. Schmidt, A. Bodey, C. Rau, and E. Baird, “Bumblebee visual allometry results in locally improved resolution and globally improved sensitivity,” *eLife*, vol. 8, 02 2019.

[4] K. D. Feller, C. R. Sharkey, A. McDuffee-Altekruse, H. D. Bracken-Grissom, N. P. Lord, M. L. Porter, and L. E. Schweikert, “Surf and turf vision: Patterns and predictors of visual acuity in compound eye evolution,” *Arthropod Structure & Development*, vol. 60, p. 101002, 2021.

[5] Z. M. Bagheri, A.-L. Jessop, S. Kato, J. C. Partridge, J. Shaw, Y. Ogawa, and J. M. Hemmi, “A new method for mapping spatial resolution in compound eyes suggests two visual streaks in fiddler crabs,” *Journal of Experimental Biology*, vol. 223, no. 1, 01 2020, jeb210195. [Online]. Available: https://doi.org/10.1242/jeb.210195

[6] P. Tichit, T. Zhou, H. M. Kjer, V. A. Dahl, A. B. Dahl, and E. Baird, “Insegtcone: Interactive segmentation of crystalline cones in compound eyes,” 12 2020.

[7] M. Muñoz Arias, J. K. Douglass, M. F. Wehling, and D. G. Stavenga, “Automated charting of the visual space of insect compound eyes,” *arXiv preprint arXiv:2106.05077*, 2021.

[8] Y. Cheng, J. Cao, Y. Zhang, and Q. Hao, “Review of state-of-the-art artificial compound eye imaging systems,” *Bioinspiration & Biomimetics*, vol. 14, no. 3, p. 031002, feb 2019. [Online]. Available: https://doi.org/10.1088/1748-3190/aaffb5

[9] J. E. Kuster and W. G. Evans, “Visual fields of the compound eyes of four species of cicindelidae (coleoptera),” *Canadian Journal of Zoology*, vol. 58, no. 3, pp. 326–336, 1980. [Online]. Available: https://doi.org/10.1139/z80-042

[10] J. K. Douglass and M. F. Wehling, “Rapid mapping of compound eye visual sampling parameters with FACETS, a highly automated wide-field goniometer,” *J. Comp. Physiol. A*, vol. 202, no. 12, pp. 839–851, Dec 2016.

[11] G. Bottone, “Automation of the mapping process of a compound eye with GRACE and Voronoi correlation,” Master’s thesis, University of Groningen, 2020. [Online]. Available: https://fse.studenttheses.ub.rug.nl/21708

[12] D. Krijestorac, “Image analysis of the fading pseudopupil phenomenon in butterfly compound eyes,” Master’s thesis, University of Groningen, 2020. [Online]. Available: https://fse.studenttheses.ub.rug.nl/21844

[13] O. Fonseca-Aguilar, “Positioning control and port-hamiltonian based model for compound eyes microscopy,” Master’s thesis, Instituto Tecnológico de Costa Rica, 2019. [Online]. Available: https://repositoriotec.tec.ac.cr/handle/2238/10758

[14] R. Niemeijer, “Scanning path for rapid mapping of a compound eye with GRACE,” Master’s thesis, University of Groningen, Aug 2018. [Online]. Available: https://fse.studenttheses.ub.rug.nl/18382

[15] A. Six Dijkstra, “GRACE Graphical user interface,” Master’s thesis, University of Groningen, Jul 2018. [Online]. Available: https://fse.studenttheses.ub.rug.nl/17969

[16] D. Reinders, T. Steinfort, Y. Sinnige, W. Berendschot, and J. d. Poel, “Automated Light Intensity and Camera Positioning for the Goniometric Robotic Apparatus for Compound Eyes,” 2018, pdf document.

[17] M. Guzmán-Fonseca, “Design and Implementation of an Autofocusing Algorithm for the Goniometric Robotic Apparatus for Compound Eyes,” Master’s thesis, Instituto Tecnológico de Costa Rica, 2017. [Online]. Available: https://repositoriotec.tec.ac.cr/handle/2238/10378

[18] K. Sahu, “Automated Image Feature Identification for Motorised Mapping of Insect Eyes,” Master’s thesis, Faculty of Science and Engineering, 2017. [Online]. Available: https://fse.studenttheses.ub.rug.nl/15738

[19] W. J. Retana-Calvo, “Design and implementation of a 6 degrees of freedom controller for the GRACE system,” Master’s thesis, Instituto Tecnológico de Costa Rica, 2016. [Online]. Available: https://repositoriotec.tec.ac.cr/handle/2238/7253

[20] M. v. d. Horst, “Design of an angular position measurement system and controller for a 3D Robotic Scanner,” Master’s thesis, Faculty of Science and Engineering, 2016. [Online]. Available: https://fse.studenttheses.ub.rug.nl/13932

[21] J. Andrés Vargas Delgado, “An image stitching algorithm for compound vision research,” 2016, pdf document.

[22] G.-J. Doornbos, “Design and implementation of an autofocusing algorithm for a 3D robotic scanner,” Master’s thesis, Faculty of Science and Engineering, 2015. [Online]. Available: https://fse.studenttheses.ub.rug.nl/12694

[23] T. R. Spanier, “The Design and Implementation of the Full Actuation for the Five DOF 3D Robotic Scanner,” Master’s thesis, Faculty of Science and Engineering, 2015. [Online]. Available: https://fse.studenttheses.ub.rug.nl/12939

[24] M. Muñoz Arias, J. K. Douglass, M. F. Wehling, and D. G. Stavenga, “Automated charting of the visual space of housefly compound eyes,” N.D., unpublished.

[25] D. G. Stavenga, “Reflections on colourful ommatidia of butterfly eyes,” *Journal of Experimental Biology*, vol. 205, no. 8, pp. 1077–1085, Apr. 2002.

[26] S. Inoué and K. R. Spring, *Video Microscopy: The Fundamentals.* Springer US, 1997.

[27] S. Ltd., "Standa Opto-Mechanical Products 2016/2017 (Full version of Standa printed catalog)," [Online; accessed 12. Dec. 2021]. [Online]. Available: https://www.standa.lt/PDF/Standa-Opto-Mechanical-Products-2016-2017.pdf

[28] B. Gustavii, *How to Write and Illustrate a Scientific Paper*, 2nd ed. Cambridge University Press, 2008.

[29] "Standa 8SMC#-USB controllers documentation," Dec 2021, [Online; accessed Jan. 2022]. [Online]. Available: https://doc.xisupport.com/en/index.html

[30] "8SMC4-USB User Manual," Dec 2021, [Online; accessed Jan. 2022]. [Online]. Available: https://doc.xisupport.com/en/8smc4-usb/8SMC4-USB.pdf

[31] "8SMC4-USB User Manual — 8SMC4-USB User Manual," Dec 2021, [Online; accessed Jan. 2022]. [Online]. Available: https://doc.xisupport.com/en/8smc4-usb/index.html#

[32] "libximc 2.13.1," Sep 2021, [Online; accessed Jan. 2022]. [Online]. Available: http://files.xisupport.com/8SMC4-USB_Programming_manual_Eng.pdf

[33] "libximc: libximc library," May 2021, [Online; accessed Jan. 2022]. [Online]. Available: https://libximc.xisupport.com/doc-en

[34] "Standa Software webpage for XIMC and XILab," Dec 2021, [Online; accessed Jan. 2022]. [Online]. Available: http://files.xisupport.com/Software.en.html